ISSN 8755-6839

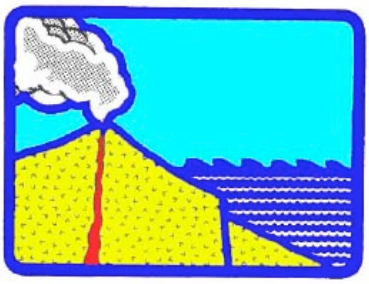

SCIENCE OF TSUNAMI HAZARDS

The International Journal of The Tsunami Society
Volume 28 Number 2 Published Electronically 2009

TSUNAMI SOCIETY, 1741 Ala Moana Blvd. #70, Honolulu, HI 96815, USA.

WWW.TSUNAMISOCIETY.ORG

OBJECTIVE: The Tsunami Society publishes this journal to increase and disseminate knowledge about tsunamis and their hazards.

DISCLAIMER: Although these articles have been technically reviewed by peers, the Tsunami Society is not responsible for the veracity of any statement, opinion or consequences.

Submit manuscripts of articles, notes or letters to the Editor. If an article is accepted for publication the author(s) must submit a scan ready manuscript, a Doc, TeX or a PDF file in the journal format. Issues of the journal are published electronically in PDF format. Recent journal issues are available at:
http://www.TsunamiSociety.org
http://www.sthjournal.org

Tsunami Society members will be advised by e-mail when a new issue is available. There are no page charges for one paper per calendar year for authors who are members of the Tsunami Society. Permission to use figures, tables and brief excerpts from this journal in scientific and educational works is hereby granted provided that the source is acknowledged.

Issues of the journal from 1982 thru 2005 are available in PDF format at http://epubs.lanl.gov/tsunami/ and on a CD-ROM from the Society to Tsunami Society members. ISSN 8755-6839 http://www.sthjournal.org

NOAA/WEST COAST AND ALASKA TSUNAMI WARNING CENTER ATLANTIC OCEAN RESPONSE CRITERIA

Paul Whitmore - NOAA/West Coast/Alaska Tsunami Warning Center - Palmer, Alaska
Uri ten Brink – United States Geological Survey – Woods Hole, Massachusetts
Michael Caropolo – NOAA/National Weather Service – Wilmington, North Carolina
Victor Huerfano-Moreno – Puerto Rico Seismic Network – Mayaguez, Puerto Rico
William Knight - NOAA/West Coast/Alaska Tsunami Warning Center - Palmer, Alaska
William Sammler – NOAA/National Weather Service – Wakefield, Virginia
Al Sandrik – NOAA/National Weather Service – Jacksonville, Florida

ABSTRACT

West Coast/Alaska Tsunami Warning Center (WCATWC) response criteria for earthquakes occurring in the Atlantic and Caribbean basins are presented. Initial warning center decisions are based on an earthquake's location, magnitude, depth, distance from coastal locations, and pre-computed threat estimates based on tsunami models computed from similar events. The new criteria will help limit the geographical extent of warnings and advisories to threatened regions, and complement the new operational tsunami product suite. Criteria are set for tsunamis generated by earthquakes, which are by far the main cause of tsunami generation (either directly through sea floor displacement or indirectly by triggering of sub-sea landslides).

The new criteria require development of a threat data base which sets warning or advisory zones based on location, magnitude, and pre-computed tsunami models. The models determine coastal tsunami amplitudes based on likely tsunami source parameters for a given event. Based on the computed amplitude, warning and advisory zones are pre-set.

INTRODUCTION

In 2005 the U.S. National Oceanic and Atmospheric Administration (NOAA) extended its tsunami warning system coverage to the U.S. Atlantic and Gulf of Mexico coasts as well as to eastern Canada. A rudimentary system was already in place for Puerto Rico and the Virgin Islands (PR/VI) thanks to a cooperative effort between the NOAA/Pacific Tsunami Warning Center and the Puerto Rico Seismic Network (PRSN) that started in 2003. In 2005, warning criteria for the North American Atlantic coast were based on the little available historical data, and by extrapolation from criteria used in the Pacific basin.

Prior to 2005, no tsunami warning system was in place for U.S. Atlantic coasts outside of PR/VI due to the assumption that the tsunami hazard was low for that region. Dunbar and Weaver (2008) confirmed this characterization by ranking the U.S. Atlantic and Gulf of Mexico tsunami threat level as low to very low. This compares with their ranking of PR/VI and the U.S. west coast as high, and Alaska and Hawaii as very high. One lesson learned from the 2004 Indian Ocean tsunami and resultant loss of life was that the impact of just a single major tsunami to areas with low tsunami threat justifies the establishment of a tsunami warning system. While some of the areas greatly impacted by the 2004 tsunami were known to be at risk, several of the countries had no previous history of any tsunami impact (such as Maldives and Kenya).

The purpose of this report is to refine criteria the WCATWC uses to issue tsunami messages in its Atlantic area-of-responsibility (AOR – Figure 1). This AOR consists of the coasts of eastern Canada, U.S. Atlantic states, U.S. Gulf of Mexico states, and Puerto Rico/Virgin Islands. Criteria are proposed for tsunamis generated both inside and outside the AOR. The criteria address when alerts are issued, to which areas, and what level of alert is sent. The term "alert" refers to tsunami warning, watch, and advisory which are defined later.

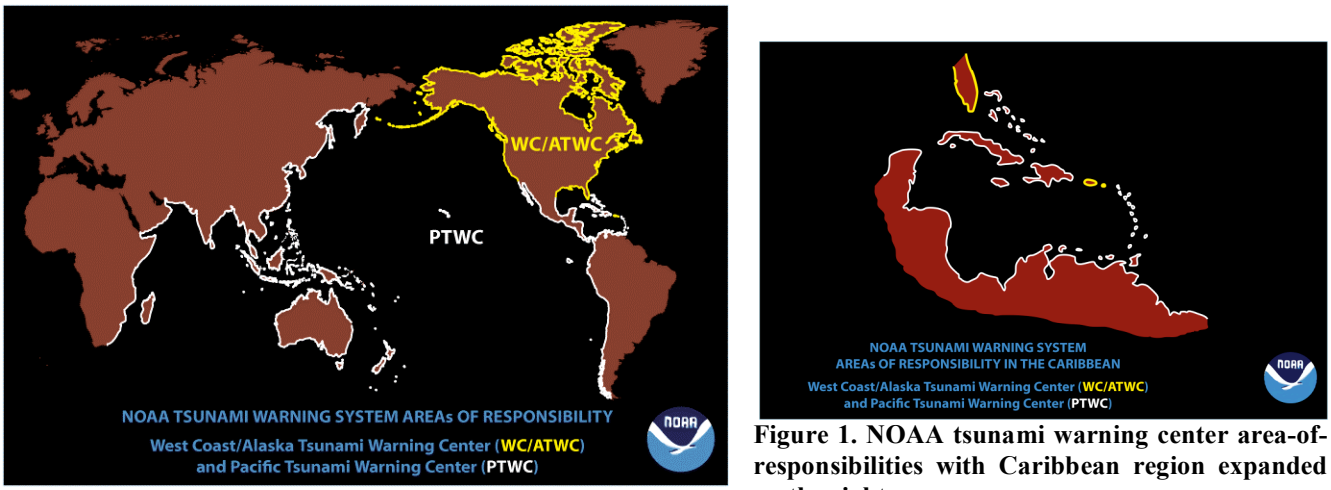

Figure 1. NOAA tsunami warning center area-of-responsibilities with Caribbean region expanded on the right.

The NOAA/National Geophysical Data Center's Tsunami Database (2007) shows that approximately 85% of tsunamis are generated by earthquake disturbance of the sea floor. Many of the other tsunamis are generated by landslides that are often triggered by strong earthquake shaking. Due

to this relationship between earthquake activity and tsunami generation, seismic data (provided by the United States Geological Survey (USGS), the Global Seismic Network, Earthquakes Canada, Puerto Rico Seismic Network, regional seismic networks, and others) are used by tsunami warning centers (TWCs) to characterize an earthquake's potential to generate a tsunami. Unfortunately, seismic signal strength is not directly proportional to the tsunami strength. Tsunami generation mechanisms can vary greatly for two equally-sized earthquakes. This reality forces warning centers to use conservative warning protocols when basing warnings solely on seismic data; particularly for those nearest the source as the wave will not be recorded prior to impact. A tsunami warning system's inability to see the phenomena for which it warns distinguishes from it from hazard warning systems for hurricanes, volcanic ash emissions, and solar storms.

TSUNAMI WARNING CENTER OPERATIONS

Two basic types of data are recorded at tsunami warning centers: seismic and sea level. Data from approximately 350 seismometers are recorded at the WCATWC (Figure 2). The center's seismic data processing system is optimized to characterize large earthquakes as quickly as possible. Normally, the first message concerning an event is based strictly on seismic data, because at that point the tsunami will not have been measured on a sea level gage.

After the initial bulletin is issued, seismic data are further analyzed to verify the magnitude, location, and depth, and to better characterize the event. Fault plane solutions, moment tensors, aftershock locations, and other fault parameters are determined at this point. Through the California Integrated Seismic Network's CISN Display software, earthquake characteristics computed at other seismic laboratories are shared with the WCATWC.

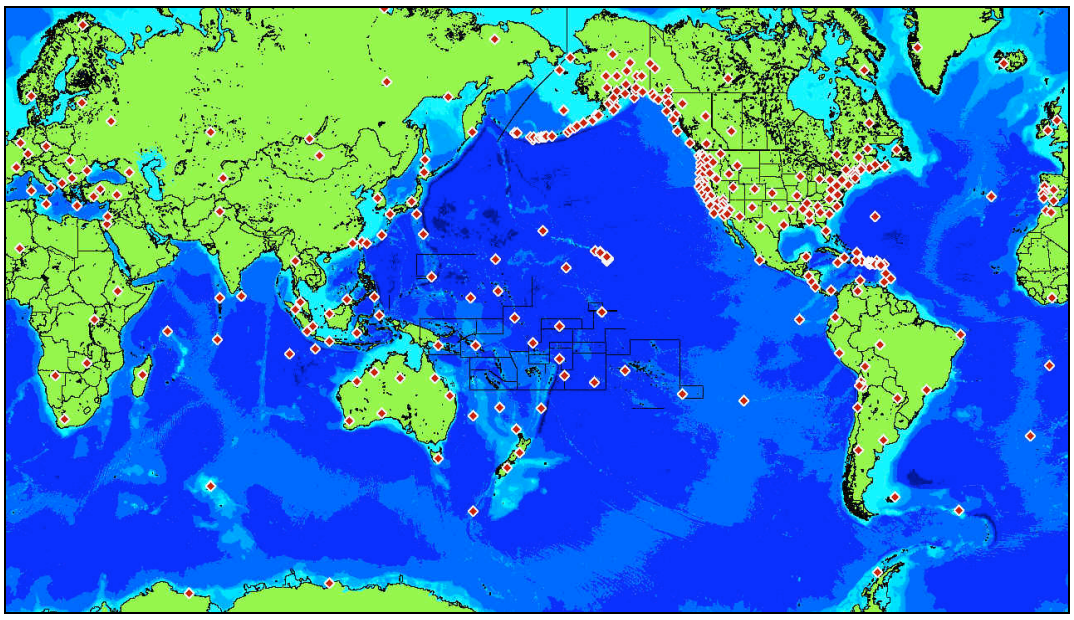

Figure 2. Diamonds represent seismometer locations recorded at the WCATWC from sources such as the USGS, NOAA, Global Seismic Network, Puerto Rico Seismic Network, regional seismic networks, Earthquakes Canada, and others.

Concurrent with secondary seismic data analysis, the center monitors data from over 400 sea level stations worldwide in near real-time (Figure 3). The center also has access to sea level information from eastern Canada over the internet. Two types of sea level data are available: coastal tide gage data and deep-ocean pressure sensor data (Deep-ocean Assessment and Reporting of Tsunamis (DART) Gonzalez, *et al*., 2005). Since 2005, the amount and quality of both tide gage data and DART data has greatly improved. Seven DARTs are operated by NOAA in the Atlantic, Caribbean, and Gulf of Mexico basins. NOAA's National Ocean Service also operates an extensive tide gage network along the U.S. coast and the PRSN operates seven tide gauges in Puerto Rico and the Dominican Republic. Internationally, the sea level data are sparse, but improving in quantity. These data are critical to verify the existence of tsunamis and to calibrate models used to forecast amplitudes throughout the basin. Depending on the source location, it can take anywhere from 30 minutes to 3 hours to obtain sufficient sea level data to provide estimates of wave heights outside the source zone, or to verify that no wave has occurred and cancel the alert. Coastal sea level data coverage within the AOR is relatively dense. Even with dense network coverage, tsunami verification can take over an hour for Atlantic AOR earthquakes due to the large width of relatively shallow continental shelf and corresponding low tsunami velocities along the eastern coast of North America.

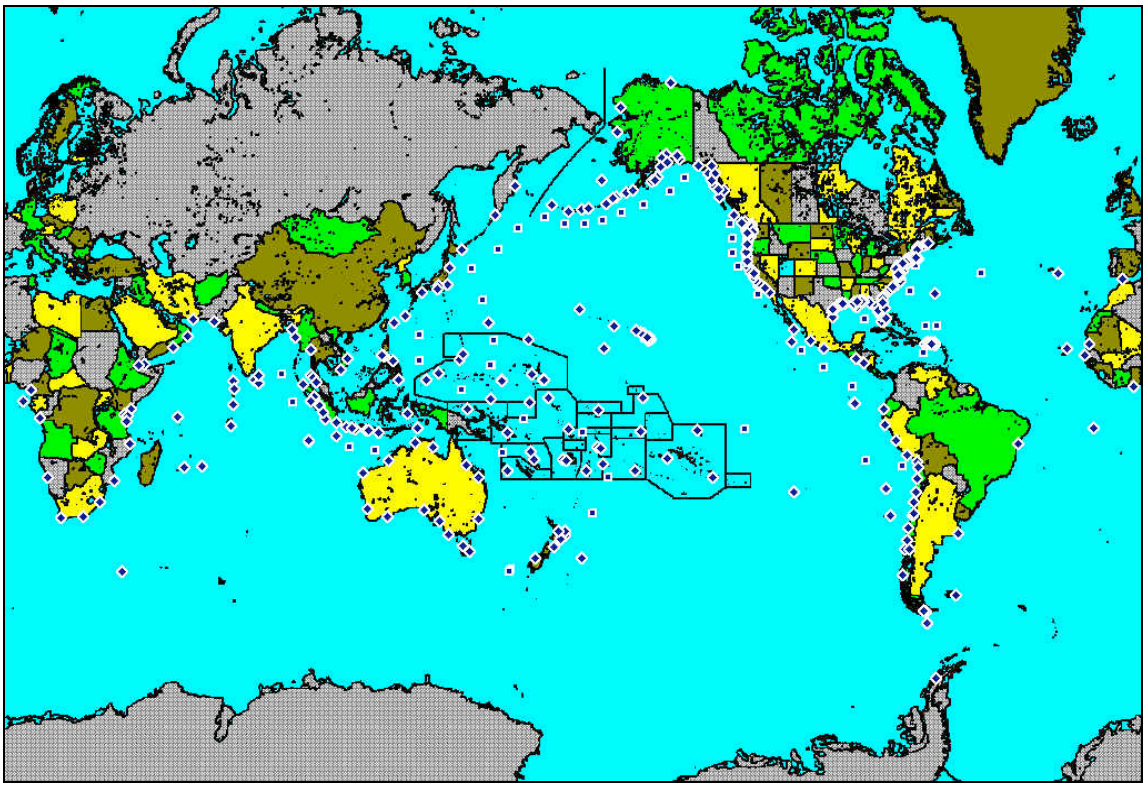

Figure 3. Diamonds represent coastal tide gages and squares represent DARTs recorded at the WCATWC. Gages are operated by NOAA, the Canadian Hydrographic Service, Puerto Rico Seismic Network, the University of Hawaii Sea Level Center, and many other national networks.

To issue alerts within the WCATWC's goal of five minutes or less for events within the AOR (Figure 4), analysts must quickly review events. Procedures for the initial message must be well planned in advance and set for all potential earthquakes. Following the initial response, analyst judgment of the situation becomes a greater part of the procedures. There are literally an infinite number of different scenarios which can play out during an event, and it is impossible to set criteria for each situation.

One of the biggest challenges to TWCs considering the rapid response requirement is computing accurate earthquake magnitudes. Figure 5 shows that WCATWC magnitude accuracy is generally within +/-0.2 units when compared to final USGS results. For earthquakes with magnitude 8 and above, the center's initial magnitude estimate is often low because the earthquake rupture may have not finished rupture by the time the initial processing is completed. Response criteria are set conservatively enough that the initial response will provide the proper alert to those nearest the epicenter even with an under-estimated magnitude for earthquakes of this size.

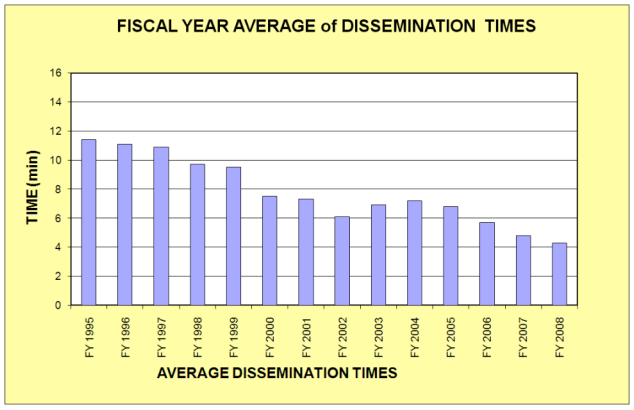

Figure 4. WCATWC response time summary. Response time is defined as the time of bulletin issuance minus the earthquake's origin time. Decrease in response time has been made possible by the use of denser broadband seismic networks, improved seismic analysis software, and 24x7 staffing of the center.

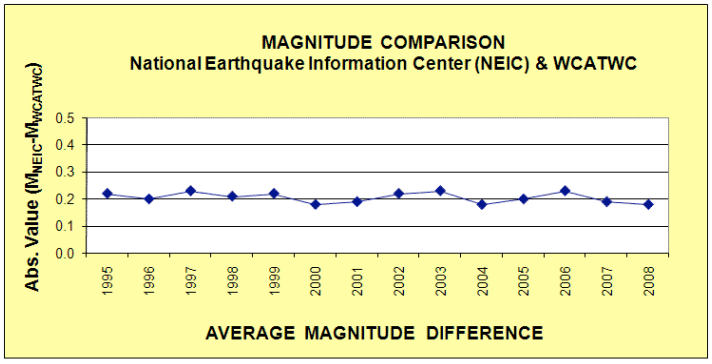

Figure 5. WCATWC magnitude accuracy summary. The values shown by diamonds are the yearly averages of the absolute value of the difference between the initial WCATWC magnitude and the final USGS magnitude for earthquakes located in the WCATWC AOR.

After an alert is issued, messages are updated every 30 minutes during the early parts of an event with the frequency decreasing in the latter times of the event. In the early stages of an event, there may be no sea level data to support analysis in these supplemental messages (often the case when the event is outside the AOR). In these cases, secondary seismic analysis to better characterize the source can help guide the response of the warning center.

TSUNAMI WARNING CENTER MESSAGE SUITE

The WCATWC tsunami message suite was revamped in February 2008. The suite has progressed from effectively a three-level suite to a four-level suite. The products issued by the center are warning, watch, advisory, and information statement. Each has a distinct meaning relating to local emergency response. In summary:

Warning	->	Inundating wave possible	->	Full evacuation suggested
Watch	->	Danger level not yet known	->	Stay alert for more info
Advisory	->	Strong currents likely	->	Stay away from the shore
Information	->	Minor waves at most	->	No action suggested

Based on seismic data analysis or forecasted tsunami amplitude (dependent on whether the center has obtained sea level data), WCATWC will issue the appropriate alert. Warnings and Advisories suggest that action should be taken. Watches are issued to provide an early alert for areas that are distant from the wave front, but may be in danger. Once the danger level is determined, the watch is converted to a warning or advisory based on expected impact, or canceled. The full definition of each message is given below:

Tsunami Warning - a tsunami warning is issued when a potential tsunami with significant widespread inundation is imminent or expected. Warnings alert the public that widespread, dangerous coastal flooding accompanied by powerful currents is possible and may continue for several hours after arrival of the initial wave. Warnings also alert emergency management officials to take action for the entire tsunami hazard zone. Appropriate actions to be taken by local officials may include the evacuation of low-lying coastal areas, and the repositioning of ships to deep waters when there is time to safely do so. Warnings may be updated, adjusted geographically, downgraded, or canceled. To provide the earliest possible alert, initial warnings are normally based only on seismic information.

Tsunami Watch - a tsunami watch is issued to alert emergency management officials and the public of an event which may later impact the watch area. The watch area may be upgraded to a warning or advisory - or canceled - based on updated information and analysis. Therefore, emergency management officials and the public should prepare to take action. Watches are normally issued based on seismic information without confirmation that a destructive tsunami is underway.

Tsunami Advisory - a tsunami advisory is issued due to the threat of a potential tsunami which may produce strong currents or waves dangerous to those in or near the water. Coastal regions historically prone to damage

due to strong currents induced by tsunamis are at the greatest risk. The threat may continue for several hours after the arrival of the initial wave, but significant widespread inundation is not expected for areas under an advisory. Appropriate actions to be taken by local officials may include closing beaches, evacuating harbors and marinas, and the repositioning of ships to deep waters when there is time to safely do so. Advisories are normally updated to continue the advisory, expand/contract affected areas, upgrade to a warning, or cancel the advisory.

Tsunami Information Statement - a tsunami information statement is issued to inform emergency management officials and the public that an earthquake has occurred, or that a tsunami warning, watch or advisory has been issued for another section of the ocean. In most cases, information statements are issued to indicate there is no threat of a destructive tsunami and to prevent unnecessary evacuations as the earthquake may have been felt in coastal areas. An information statement may, in appropriate situations, caution about the possibility of destructive local tsunamis. Information statements may be re-issued with additional information, though normally these messages are not updated. However, a watch, advisory or warning may be issued for the area, if necessary, after analysis and/or updated information becomes available.

Whitmore, et al. (2008) provided data from historic tsunami events which showed that coastal damage due to strong tsunami currents can occur with tsunami amplitudes measured at the shoreline as small as 0.5 m (amplitude is the level of the wave above normal sea level). Severe damage and inundation generally doesn't occur until amplitudes or vertical runups along the coast reach the 1.5-2.0 m range. These observations, combined with tsunami forecast accuracy which is expected to be in the range of 50% (Whitmore, 2003), prompt the WCATWC to issue advisories when the forecast is from 0.3 m to 1.0 m and warnings when the forecast is above 1.0 m.

WARNING CRITERIA

Tsunami response criteria can be based on historic event data when sufficient data exist for a region. The WCATWC Atlantic AOR has few historic tsunami events as shown in the National Geophysical Data Center (NGDC, 2007) historic tsunami data base and summarized here. The most active section of the AOR is the Puerto Rico/Virgin Islands region. The U.S. Virgin Islands and other nearby islands were struck by an earthquake-generated tsunami up to 10 m high in 1867 which killed 30 people. Over 140 people were killed in western Puerto Rico by a tsunami with an amplitude up to 6 m in 1918. Just to the west of Puerto Rico a magnitude 8.0 earthquake in 1946 triggered a tsunami which resulted in approximately 1800 deaths in the Dominican Republic. Another area in the Atlantic Ocean capable of producing large earthquakes and tsunamis is the region between Portugal and the Azores Islands. In 1755 an earthquake located in this region estimated at over magnitude 8.0, generated a tsunami up to 30 m in Portugal. The tsunami was recorded widely around the Atlantic, producing damage at several locations including Canada and the Caribbean. The largest historic tsunami along the U.S. and Canadian east coast was produced by a magnitude 7.2 earthquake in 1929 which triggered a large sub-sea landslide. This tsunami had maximum amplitude of 7 m along the Newfoundland coast and resulted in 22 deaths. Two other reports of smaller tsunamis along the U.S. Atlantic coast are provided by the NGDC (2007). First, a tsunami was reported in northern Florida after the 1886 Charleston, South Carolina earthquake (estimated magnitude 7.7), and a second minor

tsunami was observed in the New York region in 1964. This tsunami produced no damage and its cause is poorly understood.

In the absence of historic data for a specific region, historic data from other regions can be extrapolated. The National Geophysical Data Center (NGDC, 2007) database can be used for this purpose. Tsunami amplitudes in the database have been compared to sea level records when available and updated as necessary. Figure 6 displays tsunamis which have been recorded along the WCATWC Atlantic AOR.

The Atlantic and Gulf of Mexico Tsunami Hazard Assessment Study Group (AMTHAG, 2008) summarized the current state of knowledge of potential tsunami sources which could impact the U.S. Atlantic and Gulf of Mexico coasts. While there still remains a significant amount of research to be performed, the information contained in the report provides a basis for criteria proposed in this study. The report addressed many potential sources: events distant to the AOR in offshore Portugal and elsewhere in the eastern and mid-Atlantic, continental slope failures along the U.S. Atlantic and Gulf of Mexico coasts, landslide sources in the Puerto Rico region, and earthquake sources in the Puerto Rico region, the wider Caribbean basin, and along the U.S. and Canadian coast. Modeling performed in conjunction with some of the studied sources provides impact estimates. An earlier study by Knight (2006a) also provided important information on level of tsunami threat between basins. Knight (2006a) finds that tsunamis generated in the Atlantic/Caribbean are not expected to affect the Gulf of Mexico and vice-versa.

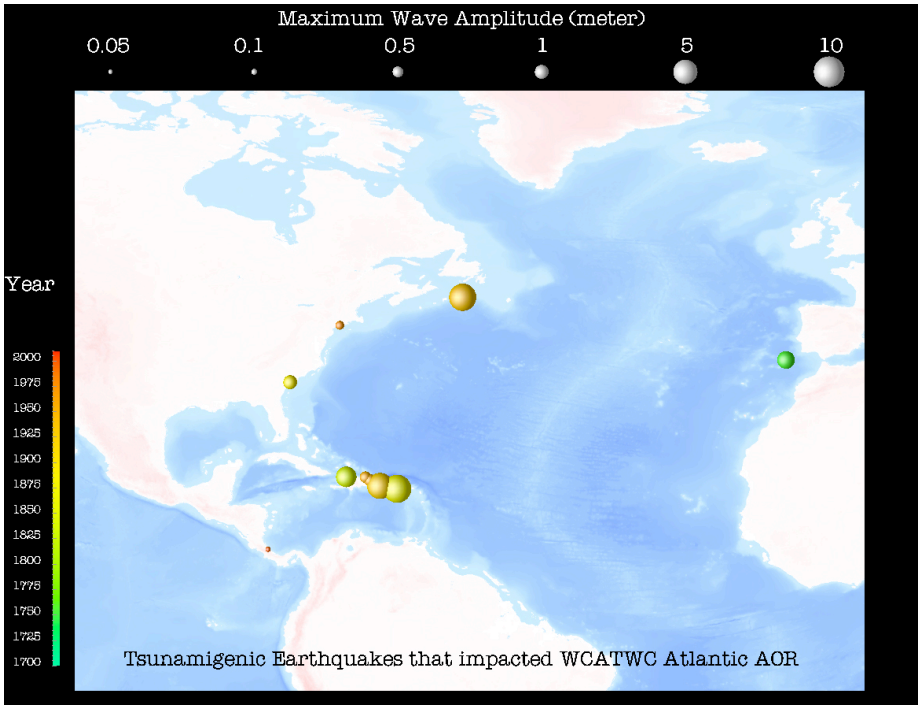

Figure 6. Events which have produced tsunamis recorded in the WCATWC Atlantic AOR (NGDC, 2007). Spheres are located at the event's source location with a size related to the maximum recorded amplitude or runup within the AOR. The sphere color relates to the event's year of occurrence.

There are some pitfalls in using forward tsunami modeling based on earthquake sources alone to set criteria for local events. Most sub-sea earthquakes less than or near magnitude 7.5 do not trigger significant tsunamis as shown later in this report. However, occasionally a major tsunami will be triggered by an earthquake of this magnitude range (e.g., 1998 Papua New Guinea, 1994 Java, and 2006 Java (NGDC, 2007)). For these events, models computed using the expected sea floor displacement will normally show a non-dangerous wave about an order of magnitude less in size than the actual wave produced. The larger waves have been attributed to many phenomena, such as associated landslides, slow slip, and slip on splay faults through the accretionary wedge (e.g., associated landslides – Tappin, *et al*. 2001; slow slip – Kanamori and Kikuchi, 1993; slip through accretionary wedge – Fukao, 1977).

Due to the lack of historical data in the Atlantic AOR, tsunami source and modeling studies refined with observations and statistics obtained from the NGDC worldwide historical tsunami data base are used to set criteria. Basic statistics relating earthquake parameters to tsunami generation observed in the NGDC database and discussed in Whitmore, *et al*. 2008 are also examined.

Several earthquake source characteristics influence whether a tsunami is generated by an earthquake and how large an area it may affect. The most obvious is earthquake size, or magnitude. Earthquake size can also be estimated by other features such as fault length, width, and slip. These other parameters are not known to the center analysts within the time frame necessary to issue the first message.

Other earthquake source factors which can influence the likelihood of tsunami generation are earthquake location (onshore distance, relationship to tectonic features, and depth of water at epicenter), hypocentral depth, and the earthquake fault mechanism. All of these characteristics influence how large an area can be affected by a tsunami if one is generated.

The influence of earthquake source parameters on tsunami generation is examined using the NGDC tsunami database. Table 1 compares hypocentral depth versus tsunami generation for all tsunamis worldwide since 1900 with amplitude 0.5 m or greater, and gives the percentage of occurrence at different hypocentral depth ranges.

Table 1. Tsunami generation versus depth (Whitmore, *et al.*, 2008). Tsunamis included are all high-validity events worldwide since 1900 with amplitude greater than 0.5 m. The last column shows the estimated total number of events over magnitude 7 for each depth range in this time period based on an extrapolation of the USGS Preliminary Determination of Epicenters catalog (2007).

Hypocentral Depth (km)	Number Tsunamis (entire database since 1900)	% of total tsunamis	% earthquakes in this depth range which produced a tsunami	Total # of earthquakes since 1900; M >= 7
< 50	343	90%	26%	1300
50-100	35	9%	25%	140
> 100	2	<1%	3%	70

Table 1 shows that the likelihood of tsunami generation by earthquakes greater than 100 km depth is very low. However, earthquakes in the range 50 km to 100 km produce a sizeable portion of significant tsunamis. Results from this table support the international tsunami standard of not issuing

tsunami warnings for earthquakes over 100 km in depth except in cases where the size, depth, and location of the earthquake indicate possible rupture to shallow depths; such as a magnitude 9 earthquake located near a subduction zone.

In the WCATWC Atlantic AOR there are not enough events to form a meaningful relationship between earthquake magnitude and tsunami generation. Table 2 compares earthquake magnitude with tsunami generation for earthquakes along the U.S. west, Alaska and British Columbia coasts.

Magnitude	Total number of earthquakes (U.S. west coast, BC, and Alaska) in potential tsunami generation areas (1900-2004)	Number of events which produced a tsunami >= 0.5m amp.	Maximum amplitude (m)	Maximum "reach" – max. epicentral distance with recorded amp. >= 0.5 m (km)	Percentage of occurrence
5.0-5.9	3549	1	3	16	0.028%
6.0-6.4	422	0			0%
6.5-7.0	266	2	2.2	28	0.75%
7.1-7.5	55	3	3	146	5.5%
7.6-7.8	10	2	1+	870	20%
7.9+	13	7	525	Tele-tsunamis	59%

Table 2. Tsunami generation versus magnitude within the WCATWC Pacific AOR (Whitmore, *et al.*, 2008). Earthquakes of all depths are included in this table. Note: Three earthquakes M > 8.5 have occurred in the region since 1900 and all three triggered basin-wide tsunamis.

Data in Table 2 show a general trend where the higher the earthquake magnitude, the more likely a tsunami will be generated. Furthermore, the higher the magnitude, the larger the area over which the wave may be dangerous. Historic data in this table support keeping warning zones small for earthquakes magnitude 7.5 and below, and increasing the geographic extent with increasing magnitude.

Tsunami generation is also influenced by an earthquake's source mechanism. That is, the more the sea floor moves vertically, the more likely it is to trigger a tsunami. Intuitively, it might seem that events with horizontal fault motion should not produce tsunamis as little sea floor is vertically moved. However, Knight (2006b) and Geist and Parsons (2005) showed that earthquakes with horizontal fault motion can produce significant tsunamis. Potential generation mechanisms include triggering of sub-aerial or sub-marine landslides, horizontal motion of an inclined sea floor, and slip vector obliqueness. Table 3 summarizes strike-slip events which produced large tsunamis from 1977 to 2004. Fault parameters are taken from the Global Centroid Moment Tensor Project Database (2007). Of the nearly 4000 earthquakes listed in the database, 109 produced a tsunami and 41 of those produced tsunamis greater than 1 m amplitude. Of those 41 events, 5 (12%) were triggered by strike slip earthquakes (with slip vectors within 20 degrees of horizontal). Each of these events only produced a tsunami dangerous near the source, and in each case the source was within 25 km of the impacted coast.

Table 3. Strike slip earthquakes which produced significant tsunamis in the period from 1977 to 2004 (Knight, 2006b; Whitmore *et al.*, 2008).

Event Date	Region	Magnitude	Maximum amplitude (m)	"Reach" – max. epicentral distance with recorded amp. >= 0.5 m (km)	Notes
9/12/1979	Irian Jaya	7.5	2.0	75	
1/21/1994	Indonesia	6.9	2.0	30	
10/8/1994	Indonesia	6.8	3.0	10	1 death
11/14/1994	Philippines	7.1	7.2	35	24 deaths
10/10/2002	Irian Jaya	7.5	4.0	75	Flooding

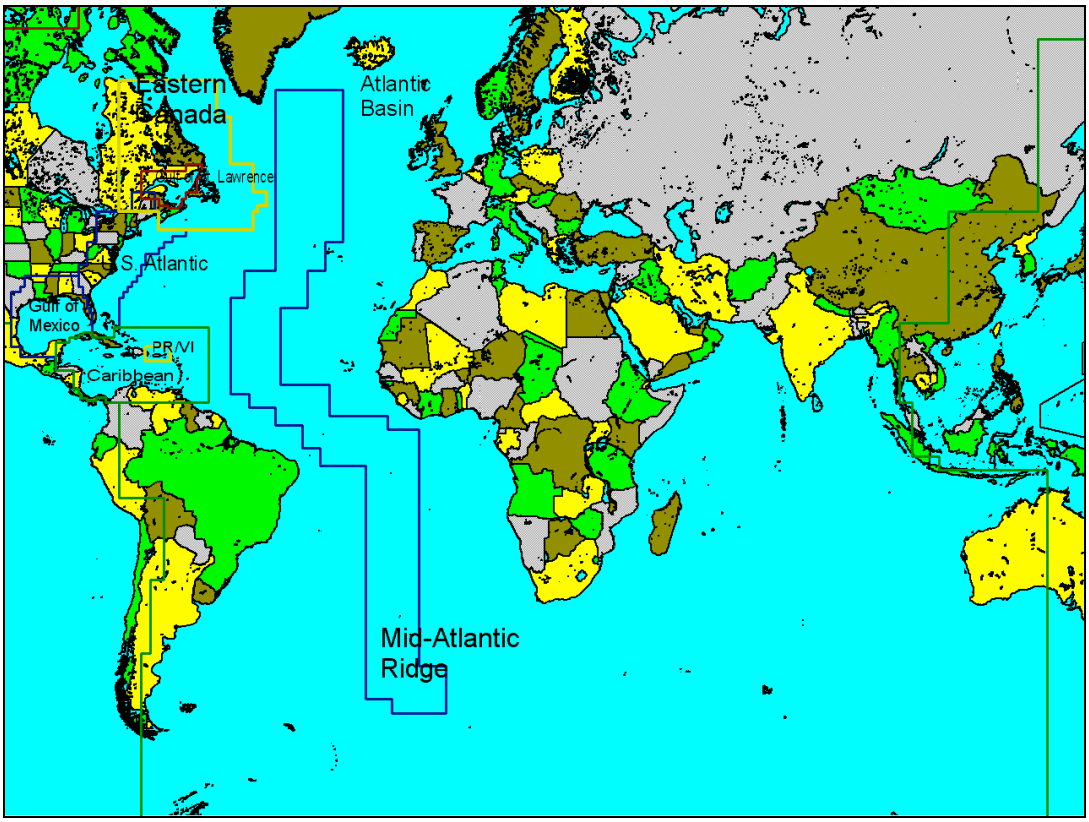

Figure 7. WCATWC Atlantic AOR geographic regions.

Earthquake/tsunami relationships based on historical data summarized above are combined with potential tsunami source information summarized in AMTHAG (2008) to set response criteria in the Atlantic by region. WCATWC Atlantic AOR regionalization is shown in Figure 7. Four criteria flowcharts are shown in Figures 8 through 11.

- Figure 8 displays criteria for earthquakes which occur in the WCATWC eastern Canada, U.S. Atlantic coast, and Gulf of Mexico AORs.
    - One potential source of a significant, widespread tsunami in this region is due to a continental slope landslide as occurred along the Grand Banks in 1929. This landslide was triggered by the largest earthquake along the U.S./Canadian Atlantic in at least the last 100 years. Historic data and tectonics suggest that large tsunami-generating earthquakes are uncommon in this region, though criteria must be set for them anyway.
    - Studies by Lee (2008) show that large continental slope failures occur periodically along the U.S. Atlantic continental slope. ten Brink, *et al*. (2008) show that these failures can trigger significant tsunamis and have attempted to relate the likelihood of a large slope failure to earthquake magnitude, distance from the slope, and slope steepness. Through tsunami modeling, Geist, *et al*. (2008) and Hornbach, *et al*. (2007) show that large continental slope failures are expected to trigger tsunamis of several meters amplitude along the U.S. Atlantic coast. The 1929 Grand Banks landslide-generated tsunami provides confirmation of this potential (Fine, *et al.,* 2004).
    - ten Brink, *et al.* (2008) show that quakes as small as 5.5 and located very near the continental slope could trigger slope failures large enough to generate tsunamis damaging to development along the Atlantic coast. There is little historical earthquake data along the Atlantic coast to verify this, though data from other regions (e.g., Table 2) show that offshore earthquakes less than magnitude 6.5 have a very small probability of generating a tsunami either directly through sea-floor uplift or indirectly through an associated sub-sea landslide. Based on the historic data and the relations shown in ten Brink, *et al*. (2008), the magnitude threshold for calling warnings along the east coast is set at 6.5. Smaller events near the slope will prompt warning center analysts to trigger DARTs near the slope and monitor coastal tide gages to verify tsunami generation prior to issuing an alert.
    - The Gulf of Mexico and Gulf of St. Lawrence have specialized procedures. Tsunamis generated within those basins are not expected to be dangerous outside the basins. Earthquakes greater than or equal to magnitude 6.5 will trigger a warning for coastal areas within the Gulf. No warning, watch, or advisory will be called for areas outside the Gulf, unless observations indicate otherwise. No warning, watch, or advisory will be called for either the Gulf of Mexico or the Gulf of St. Lawrence coast when a warning, watch, or advisory has been issued for the wider Atlantic or Caribbean basins unless observations indicate otherwise.
    - The Gulf of Mexico warning threshold is set at magnitude 6.5. The threat database will specify that earthquakes located in the deep-water Gulf and farther than 75 km from the continental slope will not trigger warnings unless their magnitude is over 7.0.

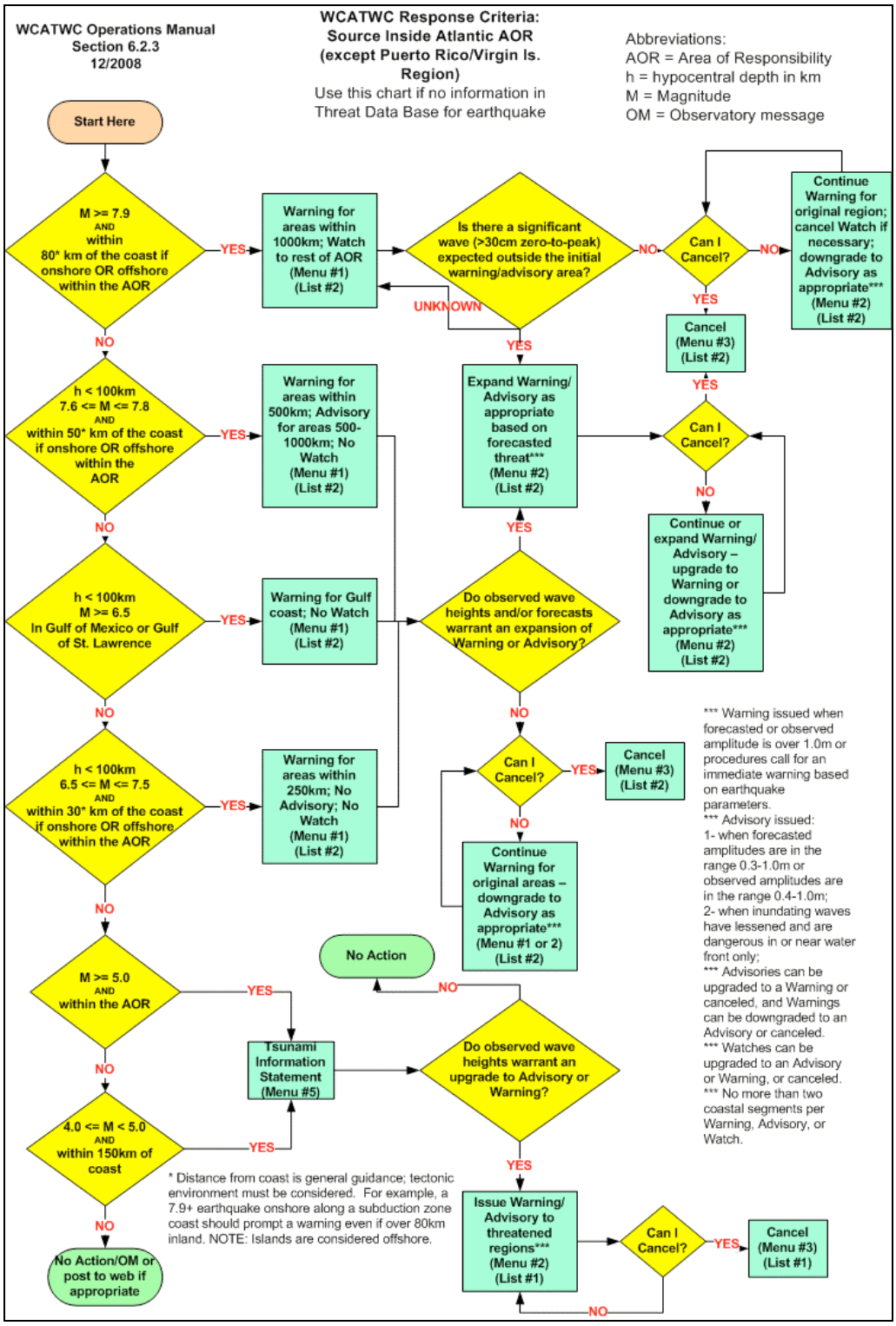

Figure 8. Criteria used for earthquakes located within the Gulf of Mexico, eastern U.S., and eastern Canada AOR.

- Figure 9 displays criteria for earthquakes which occur in the Atlantic outside WCATWC AOR regions and outside the Caribbean region.

    - The only historic basin-wide Atlantic tsunami that has occurred is the 1755 Lisbon tsunami (Barkan, *et al*., 2008). No impact was noted on the U.S. Atlantic or Gulf coasts, however the tsunami was observed in the Caribbean and in eastern Canada (Lockridge, *et al*., 2002).
    - Tsunamis generated in the Puerto Rico trench have the potential to impact U.S. and Canadian east coasts with tsunami amplitudes estimated from 1 m (Knight, 2006a) 4 m (AMTHAG, 2008) dependent on earthquake source parameters. Historic tsunamis generated near this trench have been too small to significantly impact the U.S./Canadian coast.
    - Ward and Day (2001) report that a catastrophic flank collapse on the Cumbre Viejo volcano on the island of La Palma located off the northwest Africa coast could trigger a tsunami 10-25 m high along the North American coast. More recent modeling by Gisler, *et al*. (2006) suggests much smaller amplitudes on the order of less than one meter.
    - The mid-Atlantic Ridge is the site of many large earthquakes (Global Centroid Moment Tensor Project Database, 2007). , though none of these are known to have triggered a tsunami observed in the WCATWC AOR.
    - Given the lack of widespread, significant potential tsunami sources throughout the area outside the WCATWC AOR/Caribbean and the ability to observe a tsunami on sea level gages well before impact along AOR coasts from distant sources, criteria in Figure 9 require observation of a significant wave prior to issuance of an alert for the WCATWC AOR. Alerts are not issued based on earthquake parameters alone as they are within the AOR when travel times are short.
    -

- Figure 10 displays criteria for earthquakes which occur in the Puerto Rico/Virgin Islands (17^{o}N to 20^{o}N and 63.5^{o}W to 69^{o}W) region.
    - Two significant tsunamis have been generated in the PR/VI region in the last 150 years: the 1867 Virgin Islands tsunami (Zahibo, *et al.,* 2003) and the 1918 Puerto Rico tsunami (e.g., Mercado and McCann, 1998).
    - Zahibo, *et al*. (2003) show that the 1867 tsunami can be described by co-seismic sea floor displacement from an earthquake source north of St. Croix Island based on a magnitude 7.5 earthquake. Observed tsunami runups ranged from 1 to 10 m. Models given in Zahibo, *et al*. (2003) simulated the observations well except for those reported from the island of Guadeloupe.
    - The 1918 Puerto Rico tsunami has been proposed to be both landslide generated (Hornbach, *et al.,* 2007; Lopez-Venegas, *et al*., 2008), and generated by co-seismic sea floor uplift due to the magnitude 7.5 earthquake (Mercado and McCann, 1998). Landslide generation was confirmed by broken oceanic communication cables.

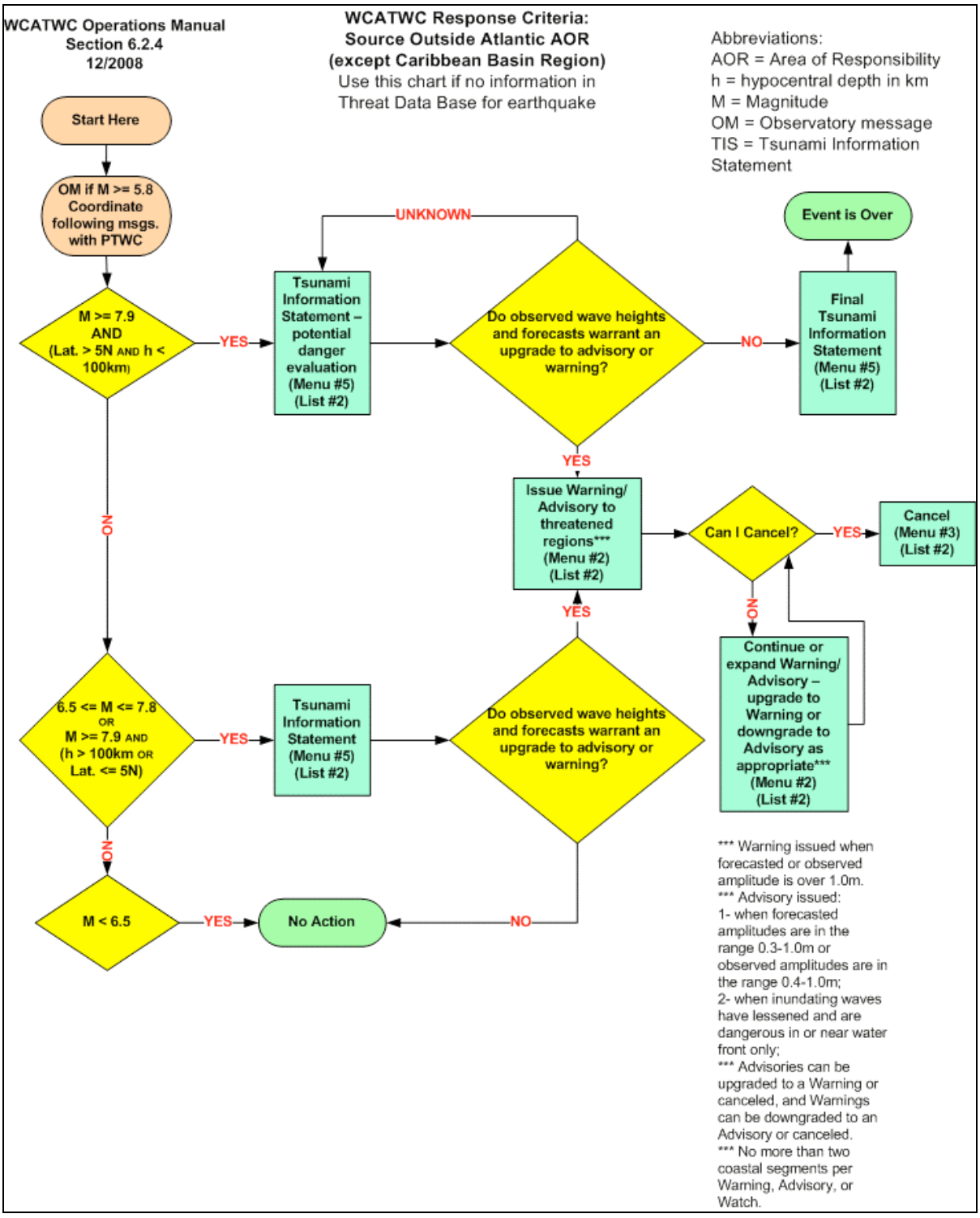

Figure 9. Criteria for Atlantic earthquakes located outside the Caribbean and WCATWC AOR.

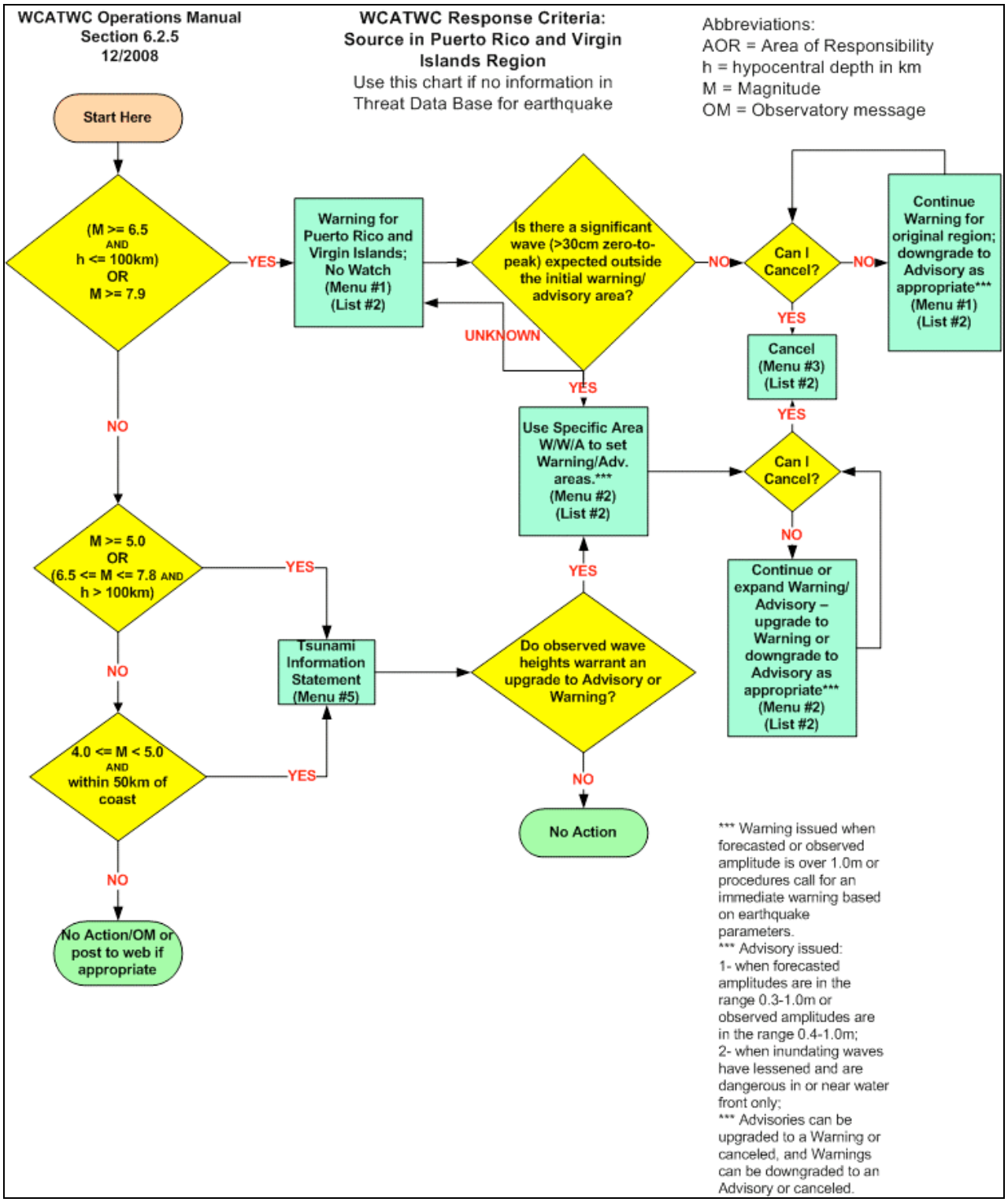

Figure 10. Criteria for earthquakes located near Puerto Rico and the Virgin Islands.

- The PR/VI region contains several potential tsunami sources. These include sources west and east of Puerto Rico as occurred in 1918 and 1867, subduction zone events to the north, and Muertos Trough events to the south (Carbo, *et al*., 2005; ten Brink, *et al*., 2004 for more details on PR/VI region tectonics).
- Based on the potential for landslide generation and the history of events within the PR/VI AOR, earthquakes magnitude 6.5 and greater will trigger the issuance of a tsunami warning for Puerto Rico and the Virgin Islands.
- Development of the threat data base and use of finer break points will allow better constraints on PR/VI warning extent. For example, magnitude 7.0 earthquakes on the western coast of Puerto Rico are not expected to significantly impact eastern Puerto Rico and the Virgin Islands. For cases like this, the threat database used in conjunction with finer-grained warning zones will allow limiting the warning to threatened regions.

• Figure 11 displays criteria for earthquakes which occur in the Caribbean region outside PR/VI.

- The only historic tsunami observations over 0.5 m amplitude in PR/VI from tsunamis generated outside the PR/VI region were due to earthquakes in 1842 (magnitude 7.7) and 1946 (magnitude 8.1) north of the island of Hispanola (NGDC, 2007).
- Potential Caribbean tsunami sources that may have a significant impact in PR/VI include the tectonically active areas of the Lesser Antilles, northern Venezuela, north of Hispanola, and the region north of Costa Rica and Panama.
- Volcanic tsunami sources in the Lesser Antilles described by Pararas-Carayannis (2004) have historically only been dangerous locally.
- Due to the proximity to PR/VI, Caribbean earthquakes (located outside the PR/VI AOR) east of 75^{o}W and magnitude 7.9 or greater will trigger the issuance of a tsunami warning for PR/VI. An advisory will be issued to PR/VI for earthquakes in this region from magnitude 7.6 to 7.8.
- Earthquakes located west of 75^{o}W and with magnitude 7.9 or greater will trigger the issuance of an advisory for PR/VI. Earthquakes less than magnitude 7.9 in this region will not trigger an alert for PR/VI unless observations indicate otherwise. The longitude 75^{o}W is chosen because it is the general longitude west of which tsunami directivity due to source orientation is such that a major tsunami impact is not expected along the PR/VI coasts.

The flowcharts refer to a threat database. This database will contain warning/watch/advisory zones for events categorized by location and magnitude. The zones will be determined from tsunami models based on likely source parameters for maximum expected events within that location and magnitude range. The database will provide a mechanism for finer zonation of threatened regions than is possible by only using distance from the source as criteria. For example, tsunamis generated by U.S. Atlantic margin continental slope failures based on characteristics given in ten Brink, *et al*. (2008) can be modeled and the threatened AOR coastal regions saved in the database along with the expected impact. When an earthquake occurs which could trigger a continental slop failure, the database is first checked for information. If no information has been computed for that region or magnitude range, the

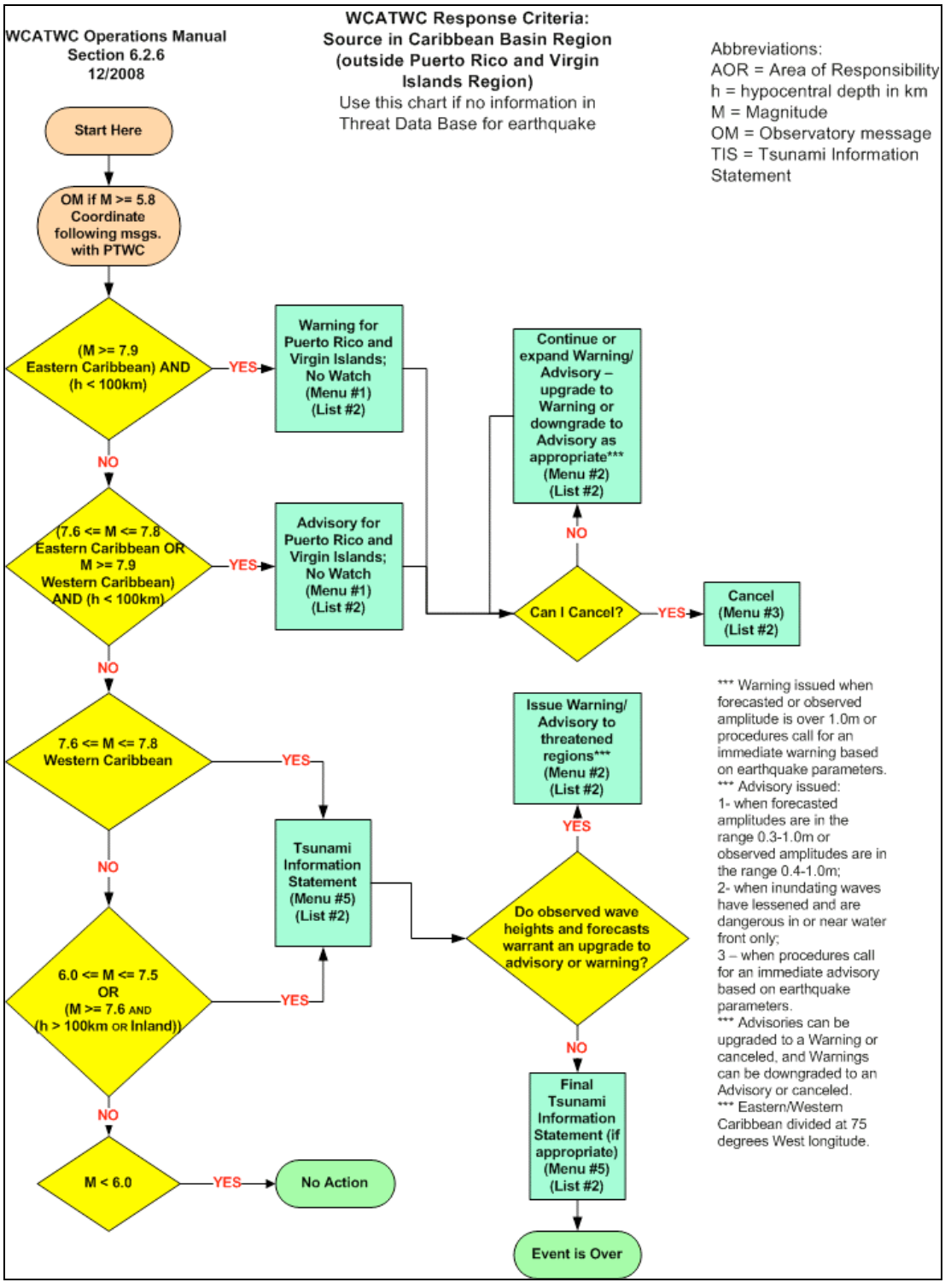

Figure 11. Criteria for Caribbean earthquakes located outside the Puerto Rico/Virgin Islands AOR.

standard response criteria will be used as given in the flow chart. If threatened zones have been pre-computed for this event, those regions will be immediately put in the appropriate alert level. The alert zones will not be adjusted until sea level data are observed on gages. Zones will then be further refined based on this information and any other forecast model or historical information available.

The seismic-based criteria given on the left sides of Figures 8 through 11 are for initial message issuance. Supplemental messages are mainly based on sea level observations and corresponding forecast models, but can be further guided by fault mechanism analysis, USGS Shake Maps, and slow earthquake discrimination by energy versus moment comparisons if sea level data and/or forecast models are not available.

FUTURE WORK

Warning criteria refinement is an ongoing process. Development of a threat database will continue as potential sources are better defined and models are computed based on those sources. Presently, these pre-computed sources are limited to tsunami generated by co-seismic, static sea floor motion, but could be expanded to include landslide sources. Continued collaboration between warning centers, tsunami research labs, and emergency management is necessary to keep criteria up-to-date with the latest research and emergency management response capabilities. New observational data sets such as better remote sensing of tsunamis, processing techniques, and basic hazard research must be incorporated into the criteria as they become available.

ACKNOWLEDGEMENTS

The authors thank George Parkes, Audrey Rubel, Jeff Osiensky, Jason Chaytor and Jeff Williams for very helpful reviews, and Paul Huang and Cindi Preller of the WCATWC for their assistance with graphics used in this report.

REFERENCES

Atlantic and Gulf of Mexico Tsunami Hazard Assessment Group (AMTHAG), 2008. Evaluation of Tsunami Sources with the Potential to Impact the U.S. Atlantic and Gulf Coasts – An Updated Report to the Nuclear Regualtory Commission: U.S. Geological Survey Administrative Report, 302 pp.

Barkan, R. U.S. ten Brink, and J Lin, *in press* 2008. Far Field Tsunami Simulations of the 1755 Lisbon Earthquake: Implications for Tsunami Hazard to the U.S. East Coast and the Caribbean, *Marine Geology*, doi:10.1016/j.margeo.2008.05.011.

Carbó, A., D. Cordoba, A.M. Martin, J.L. Granja, J.M. Davila, A. Pazos, M. Catalan, M. Gomez, U. ten Brink, C. von Hillenbrandt, J. Payero, 2005. Survey Explores Active Tectonics in Northeastern Caribbean, *Eos Trans. AGU*, **86**, doi:10.1029/2005EO510002.

Dunbar, P.K. and C.S. Weaver, 2008. U.S. States and Territories National Tsunami Hazard Assessment: Historical Record and Source for Waves, NOAA and USGS report prepared for the National Tsunami Hazard Mitigation Program, 59 pp.

Fine, I.V., A.B. Rabinovich, B.D. Bornhold, R.E. Thomson, and E.A. Kulikov, 2004. The Grand Banks Landslide-Generated Tsunami of November 18, 1929; Preliminary Analysis and Numerical Modeling, *Marine Geology*, **215**, 45-57.

Fukao, Y., 1979. Tsunami earthquakes and subduction processes near deep-sea trenches, *J. Geophys. Res*., **84**, 2303-2314.

Geist, E. and T. Parsons., 2005. Triggering of tsunamigenic aftershocks from large strike-slip earthquakes: Analysis of the November 2000 New Ireland earthquake sequence. *Geochemistry, Geophysics, Geosystems 6(10): doi: 10.1029/2005GC000935. issn: 1525-2027.*

Geist, E.L. P.J. Lynett, and J.D. Chaytor, *in press* 2008. Hydrodynamic Modeling of Tsunamis from the Currituck Landslide, *Marine Geology*, doi:10.1016/j.margeo.2008.05.011.

Gisler, G., R. Weaver, and M.L. Gittings, 2006. SAGE Calculations of the Tsunami Threat from La Palma, *Sci. Tsu. Hazards,* **24**, 288-301.

Global Centroid Moment Tensor Project Database. 2007. http://www.globalcmt.org/CMTsearch.html.

Hornbach, M.J., L.L. Lavier, and C.D. Ruppel, 2007. Triggering Mechanism and Tsunamogenic Potential of the Cape Fear Slide Complex, U.S. Atlantic Margin, *G-cubed*, **8**, Q12008, doi:10.1029/2007GC001722, 16pp.

Gonzalez, F.I., E.N. Bernard, C. Meinig, M.C. Eble, H.O. Mofjeld, and S. Stalin, 2005. The NTHMP tsunameter network, *Natural Hazards*, **35**, 25-39.

Kanamori, H. and M. Kikuchi, 1993. The 1992 Nicaragua earthquake: a slow tsunami earthquake associated with subducted sediments, *Nature*, **361**, 714-716.

Knight, W., 2006a. Model predictions of Gulf and southern Atlantic coast tsunami impacts from a distribution of sources, *Sci. Tsu. Hazards,* **24**, 304-312.

Knight, W., 2006b. Strike Slip Tsunami Sources. Abstract, The Tsunami Society Third Tsunami Symposium, Honolulu, Hawaii.

Lee, H.J., *in press* 2008. Timing of Occurrence of Large Submarine Landslides on the Atlantic Ocean Margin, *Marine Geology*, doi:10.1016/j.margeo.2008.05.011.

Lockridge, P.A., L.S. Whiteside, and J.F. Lander, 2002. Tsunamis and Tsunami-Like Waves of the Eastern United States, *Sci. Tsu. Hazards,* **20**, 120-157.

Lopez-Venegas, A.M., U.S. ten Brink, and E.L. Geist, *in press* 2008. Submarine landslide as the source for the October 11, 1918 Mona Passage tsunami: Observations and modeling, *Marine Geology*, doi:10.1016/j.margeo.2008.05.011.

Mercado, A. and W. McCann, 1998. Numerical simulation of the 1918 Puerto Rico tsunami. *Natural Hazards*, **18**, 57-76.

National Geophysical Data Center Tsunami Database. 2007. Revised November 6, 2007. http://www.ngdc.noaa.gov/seg/hazard/tsu_db.shtml.

Pararas-Carayannis, G., 2004. Volcanic Tsunami Generating Source Mechanisms in the Eastern Caribbean Region, *Sci. Tsu. Hazards,* **22**, 74-114.

Tappin, D. R., P. Watts, G. M. McMurty, Y. Lafoy, and T. Matsumoto, 2001. The Sissano, Papua New Guinea tsunami of July 1998 – offshore evidence on the source mechanism, *Marine Geology*, **175**, 1-23.

ten Brink, U.S., W. Danforth, C. Polloni, B. Andrews, P. Llanes Estrada, S. Smith, E. Parker, and T. Uozumi, 2004. New seafloor map of the Puerto Rico trench helps assess earthquake and tsunami hazards in the northwest Caribbean, *Eos Trans. AGU*, **85**, p. 349, 354.

ten Brink, U.S., H.J. Lee, E.L. Geist, and D. Twichell, *in press* 2008. Assessment of Tsunami Hazard to the U.S. East Coast using Relationships Between Submarine Landslides and Earthquakes, *Marine Geology*, doi:10.1016/j.margeo.2008.05.011.

United States Geological Survey Earthquake Hazards Program Global Earthquake Data Base, 2007. Revised November 5, 2007. http://wwwneic.cr.usgs.gov/neis/epic/epic.html.

Ward S.N. and S. Day, 2001. Cumbre Viejo Volcano – Potential Collapse and Tsunami at La Palma, Canary Islands, *Geophysical Research Letters*, **28**, 3397-4000.

Whitmore, P.M., 2003. Tsunami amplitude prediction during events: a test based on previous tsunamis, *Sci. Tsu. Hazards,* **21**, 135-143.

Whitmore, P.M., H. Benz, M. Bolton, G. Crawford, L. Dengler, G. Fryer, J. Goltz, R. Hanson, K. Kryzanowski, S. Malone, D. Oppenheimer, E. Petty, G. Rogers, and J. Wilson, 2008. NOAA/West Coast and Alaska Tsunami Warning Center Pacific Ocean Response Criteria, *Sci. Tsu. Hazards,* **27**, 1-21.

Zahibo, N., E. Pelinovsky, A.C. Yalciner, A. Kurkin, A. Koselkov, and A. Zaitsev, 2003. The 1867 Virgin Island Tsunami, *Natural Hazards and Earth System Sciences*, **3**, 367-376.

NATURAL HAZARD ASSESSMENT OF SW MYANMAR - A CONTRIBUTION OF REMOTE SENSING AND GIS METHODS TO THE DETECTION OF AREAS VULNERABLE TO EARTHQUAKES AND TSUNAMI / CYCLONE FLOODING

Barbara Theilen-Willige

Berlin University of Technology (TU Berlin), Institute of Applied Geosciences

Email: Barbara.Theilen-Willige@t-online.de

George Pararas-Carayannis

Tsunami Society, Honolulu, Hawaii, USA

Email: drgeorgepc@yahoo.com

ABSTRACT

Myanmar, formerly Burma, is vulnerable to several natural hazards, such as earthquakes, cyclones, floods, tsunamis and landslides. The present study focuses on geomorphologic and geologic investigations of the south-western region of the country, based on satellite data (Shuttle Radar Topography Mission-SRTM, MODIS and LANDSAT). The main objective is to detect areas vulnerable to inundation by tsunami waves and cyclone surges. Since the region is also vulnerable to earthquake hazards, it is also important to identify seismotectonic patterns, the location of major active faults, and local site conditions that may enhance ground motions and earthquake intensities. As illustrated by this study, linear, topographic features related to subsurface tectonic features become clearly visible on SRTM-derived morphometric maps and on LANDSAT imagery. The GIS integrated evaluation of LANDSAT and SRTM data helps identify areas most susceptible to flooding and inundation by tsunamis and storm surges. Additionally, land elevation maps help identify sites greater than 10 m in elevation height, that would be suitable for the building of protective tsunami/cyclone shelters.

Science of Tsunami Hazards, Vol. 28, No. 2, page 108 (2009)

1. INTRODUCTION

The south-western region of Myanmar is vulnerable to numerous natural hazards, such as earthquakes, cyclones, floods, tsunamis and landslides (Fig. 1). The present study was undertaken for the purpose of using remote sensing satellite imagery and methodology to determine Myanmar's vulnerability to disasters and for ways to mitigate losses of lives and improve on disaster preparedness. The assessments described in subsequent sections are based on satellite data of the Shuttle Radar Topography Mission-SRTM, MODIS and LANDSAT and focus on geomorphologic and geologic investigations of the southwest region of Myanmar. The main objective is to detect areas vulnerable to inundation by tsunamis and cyclone surges, but also to identify seismotectonic patterns, the location of major active faults and local site conditions that may enhance earthquake ground motions and seismic intensities. As illustrated by this study, linear, topographic features related to subsurface tectonic features become clearly visible on SRTM-derived morphometric maps and on LANDSAT imageries. The GIS (**G**eo-**I**nformation**S**ystem) integrated evaluation of LANDSAT and SRTM data helps to identify areas most susceptible to flooding and inundation by tsunamis and storm surges. Land elevation maps help identify sites with elevations greater than 10 m that would be suitable for building protective evacuation shelters. However, before proceeding with the analysis of the satellite data, a brief review of the region's disaster exposure is appropriate.

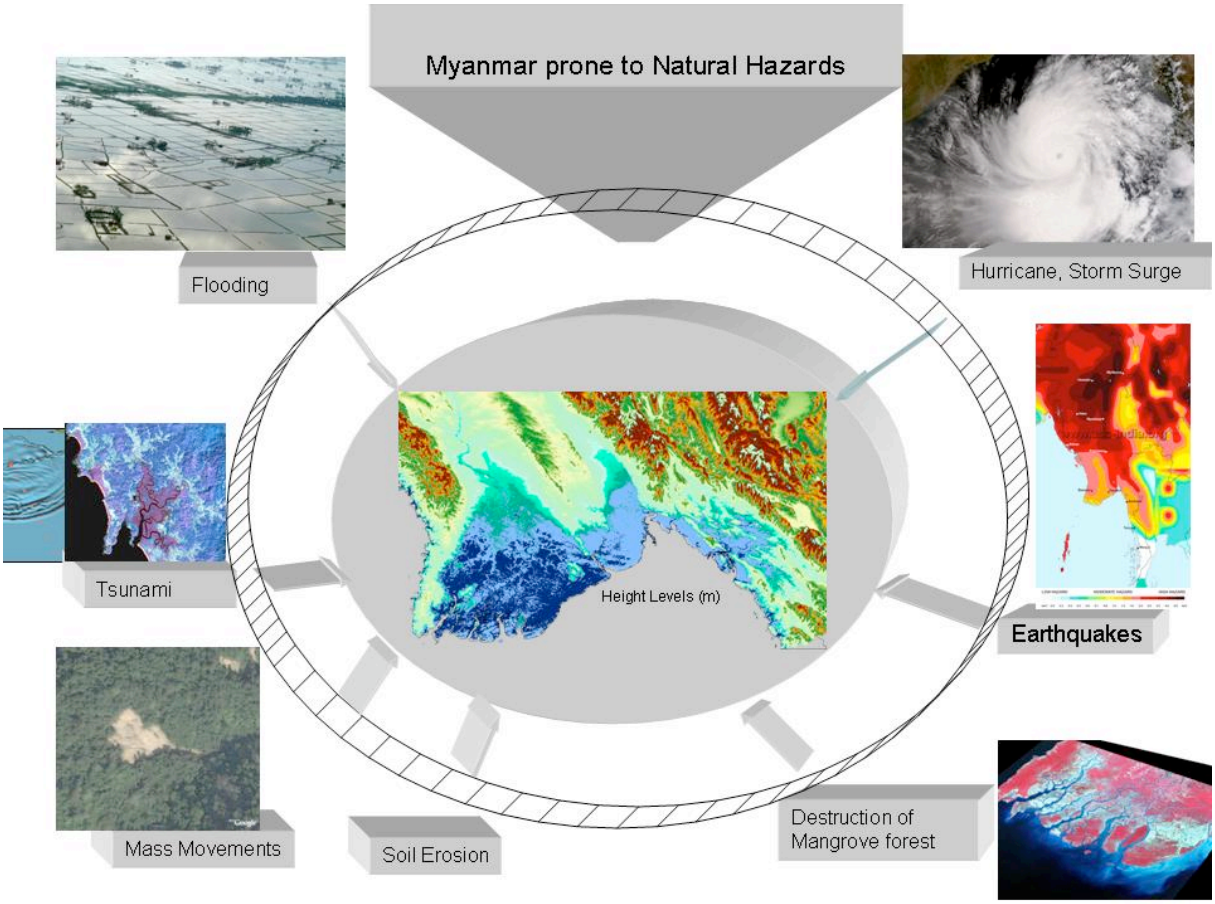

Fig. 1. The vulnerability of southwest Myanmar to natural hazards.

2. MAYNMAR'S VULNERABILITY TO NATURAL DISASTERS

Mynmar's high vulnerability to natural disasters results from its unique geographic and geologic location and geomoprhology. Myanmar borders the Bay of Bengal to the southwest and the Gulf of Martaban and the Andaman Sea along its southern periphery. The country's extensive coastline of about 1,930 (1,199 mi) and its extensive lowland areas make it particularly vulnerable to all types of marine and terrestrial disasters. Its geotectonic evolution and proximity to regions of subduction and major antithetical faulting, make it vulnerable to earthquakes, some of which could be potentially tsunamigenic.

Cyclones and Cyclone Surges - Myanmar is particularly vulnerable to cyclones originating in the Bay of Bengal during pre- and post-monsoon seasons from April to May and from October to November. These cyclones result in heavy rains, floods and storms surges, especially in the coastal region of Rakhine State. Cyclone-related disasters occur in this region every 3 to 4 years.

Additionally to the destruction by high winds, storm surges generated by the cyclones in the region usually flood the low lying and densely populated Ayeyarwady (Irrawaddy) river delta region as well as other coastal regions along the Gulf of Martaban. On May 1-3, 2008, Cyclone Nargis generated in the Bay of Bengal was the deadliest to ever hit the country. It made landfall across the delta of the Irrawaddy River, then continued northeast along the coastline and devastated Myanmar (Fig. 2). Figure 3 shows flooded areas in the Irrawaddy region.

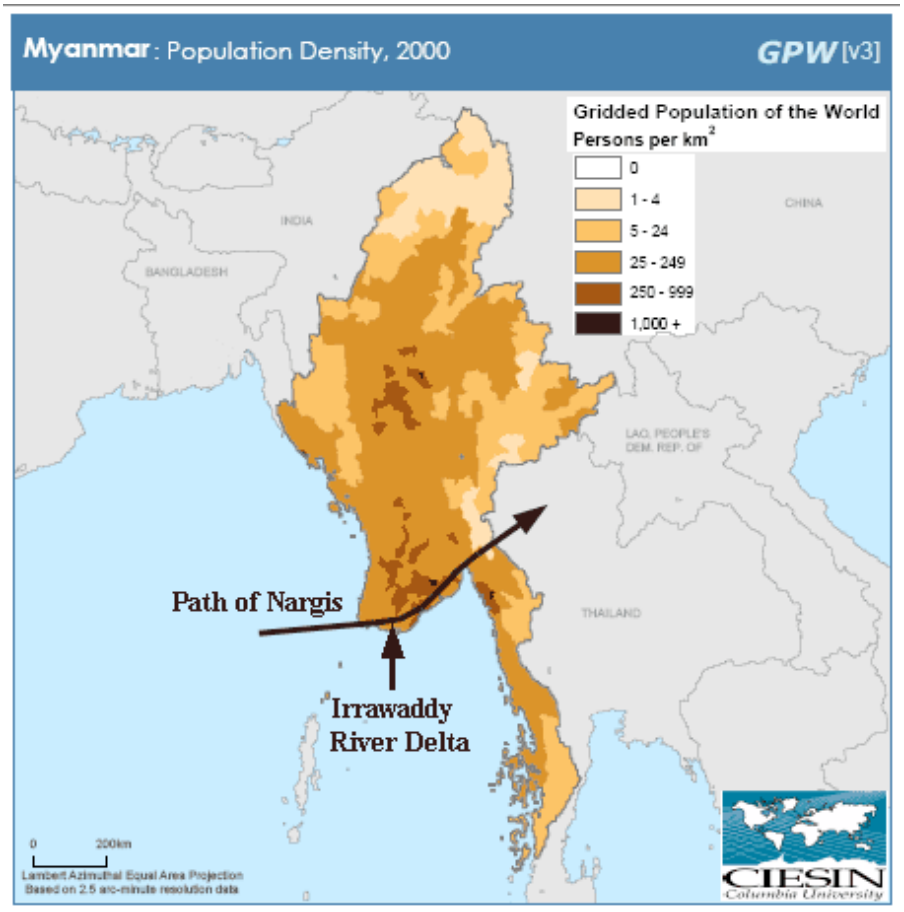

Fig. 2. Cyclone Nargis Path over the Irrawaddy River Delta Region (web graphic)

Fig. 3. Flooding by Cyclone Nargis surge at the Irrawaddy Delta. Non-flooded land of higher elevation seen as islands from NASA satellite.

Maximum reported flooding by Nargis' surge was at least 4 meters (13 feet). The cities of Yangon, Irrawaddy, Pegu and the states of Karen and Mon Worse were the most severely affected regions (Pararas-Carayannis, 2008). The cyclone was responsible for unprecedented loss of life and destruction. It is estimated that more than 100,000 people lost their lives As illustrated by the May 5 MODIS image, the entire coastal plain was flooded. The image from the Moderate Resolution Imaging Spectroradiometer (MODIS) on NASA's Terra satellite uses a combination of visible and infrared light to make floodwaters visible (Fig.4). Based on data of the RADAR satellites TerraSAR-X (DLR/Infoterra) and ALOS/PALSAR (JAXA), the Center for Satellite Based Crisis Information (ZKI) at DLR produced maps of the affected areas (DLR, ZKI, 2008).

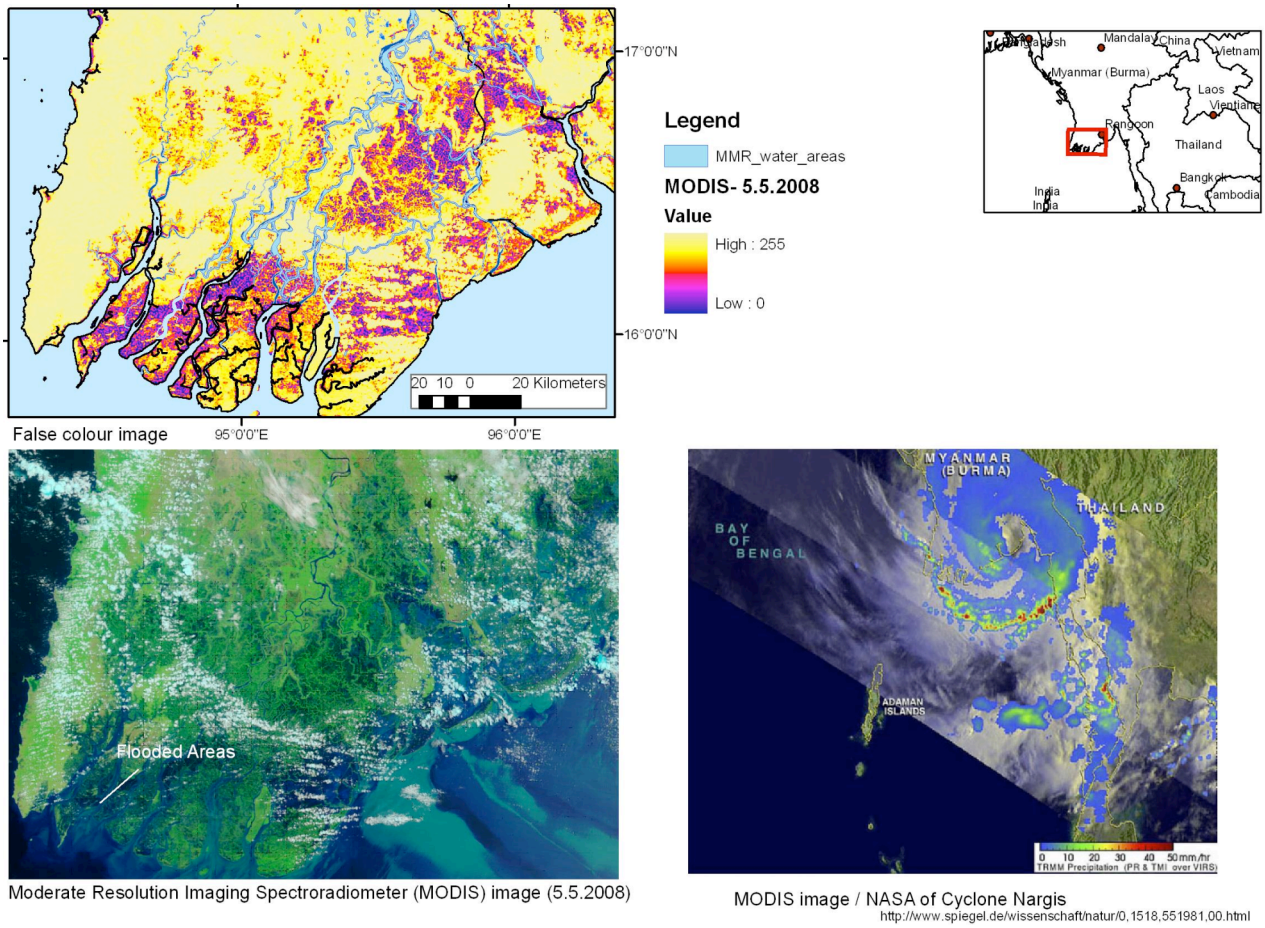

Fig. 4. MODIS image from the flooded areas (NASA)
Water is blue or nearly black, vegetation is bright green, bare ground is tan, and clouds are white or light blue. The wetlands near the shore are a deep blue green. The colour-coded image above shows the flooded areas in blue-reddish and grey tones.

Floods - Four major rivers flowing southward traverse southwest Maynmar. Sometimes, during the heavy monsoon season, rainfall in the north causes the rivers to exceed maximum levels and result in destructive flooding of adjacent towns and villages. The lowland, delta regions are also vulnerable to similar disastrous floods during the monsoon season, particularly when the high tide and the high river water flow occur at the same time. Although earthen dykes have been built to protect the lowlands, there have been times when the dykes have failed and great floods have resulted in great losses of life and property. Fig. 4 and 5 show NASA and Google Earth images of Southwest Myanmar that are also vulnerable areas to both annual and extreme floods (Asian Disaster Reduction Center, Country Report Myanmar, 2003), particularly the central plain area bounded by the two major rivers - the Irrawaddy to the west and the smaller Sittang to the east.

Tsunamis - Large earthquakes have generated tsunamis that have struck the coast of Myanmar. The country is vulnerable to tsunamis originating from earthquakes along the Andaman or the Northern Sumatra segments of the great Sunda Arc (Pararas-Carayannis, 2007a&b). Although not as severe as in other regions and apparently underreported, the December 26, 2004 tsunami impacted Maymar and was responsible for extensive loss of life (Pararas-Carayannis, 2005). The December 26, 2004 tsunami devastated the long southern coastline of the country (Democratic

Voice of Burma, 2005 McKeon et al., 2008). Worst impacted was the Irrawaddy Delta region, which is largely populated by subsistence farmers and fishermen. Fig. 5 shows Google Earth images of devastated areas several months after the tsunami struck.

Fig. 5. Destroyed buildings in the delta area of the Irrawaddy River as documented by Google Earth images.

Local tsunami generation is also very possible. Most of the local seismicity originates along the Sagaing transform which apparently undergoes a right lateral slip – a movement that is not particularly conducive to the traditional mechanism of tsunami generation but which could result in folding and deformational future seismic events with the potential to generate local tsunamis directly or by collateral mechanisms of folding, en-echelon bookshelf failures, particularly within the thick sedimentary stratigraphic layers of the Northern Andaman Sea or of the Gulf of Martaban (Pararas-Carayannis, 2009).

Furthermore, backarc seismicity results along the Shan scarp which is presumed to be a normal fault zone dissecting the Shan plateau of the SE Asian plate against the Burmese lowlands (Mukhopadhyay, 1992). However, there is also a high potential for a major tsunamigenic earthquake in the future as the western region may be representing a seismic gap where stress may have been building up as a result of recent seismic activity along Sumatra and the Andaman Sea

and the northward, oblique movement of the Indian tectonic plate (Pararas-Carayannis, 2005a&b; 2007).

The geomorphology of the Gulf of Martaban enhances the occurrence of flooding disasters. The geological conditions and shallow sea off the coast of Myanmar stretching 15 to 20 miles obviously influence the intensity of flooding (Fig. 6).

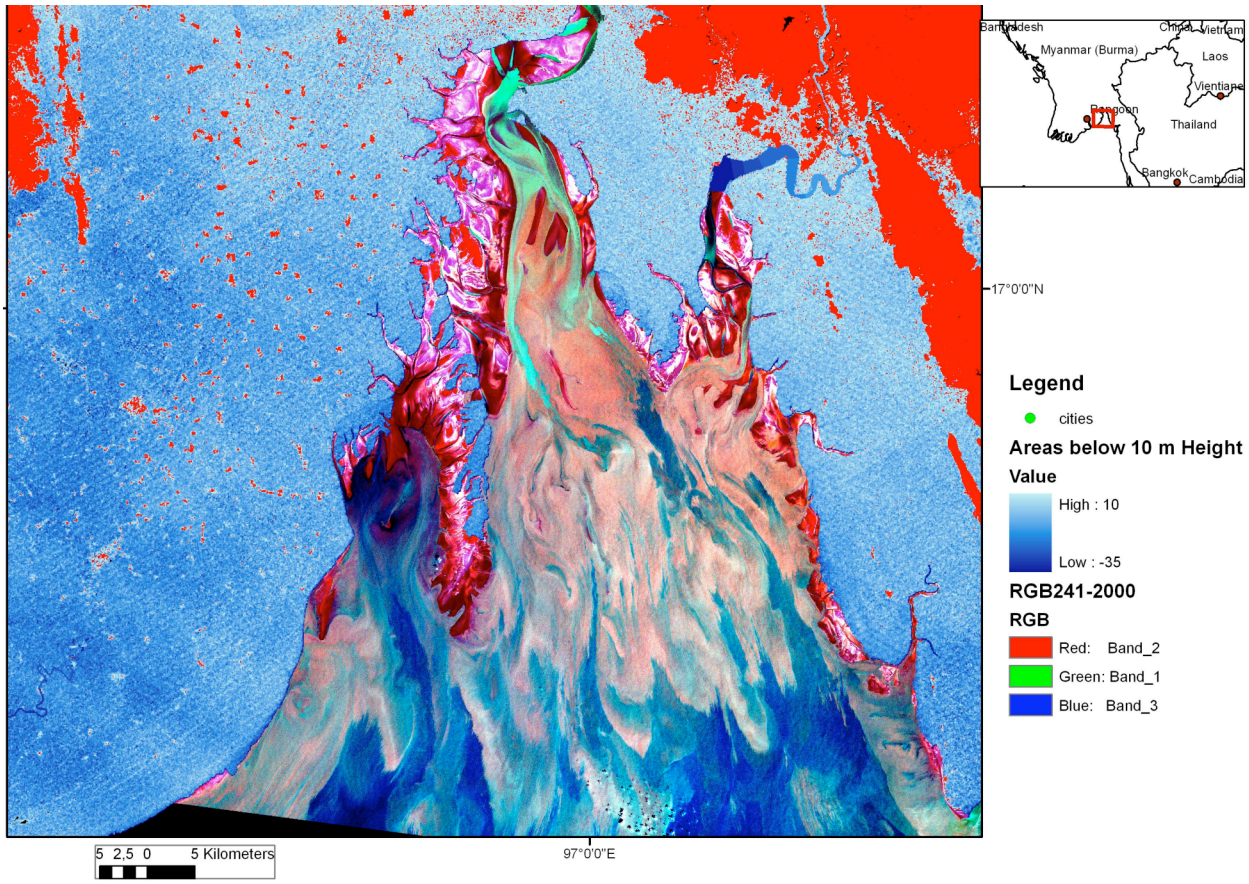

Fig. 6. Visualizing sea surface water currents and streaming in the Gulf of Martaban - based on a LANDSAT ETM false-colour composite (3.5.2000)

Earthquakes - Also, Myanmar is seismologically unstable and vulnerable to earthquakes because of its proximity to boundaries of major interacting tectonic plates. Specifically, the eastern Himalayan belt marks the collision boundary of the Indian tectonic plate underthrusting the Eurasian plate. The approximately North-South trending Indo-Burmese Arc extends southward to join the Andaman segment of the great Sunda Arc (Fig. 7). Continuous collision and movement of the northward-moving Indian plate, at an average rate of 5.5 cm/yr, results in active subduction underneath the smaller Burma plate (part of the Eurasian plate) – the latter moving northward from a spreading center in the Andaman Sea at an average rate of 2.5 – 3.0 cm/yr (Kyaw Kyaw Lin, 2008; Tun, 2008; Pararas-Carayannis, 2007). The movement of the Indian plate movement with respect to Eurasia is highly oblique along the margin of the subduction zone. Northward-trending, antithetical right-lateral shear motion occurs along the Great Sumatra fault and extends into the rift system of the Andaman

Sea (Asian Disaster Reduction Center, Country Report Myanmar, 2003; Pararas-Carayannis, 2005a and b). Very large over thrusts along the Western Fold Belt have resulted from past movements along the Sagaing and related faults.

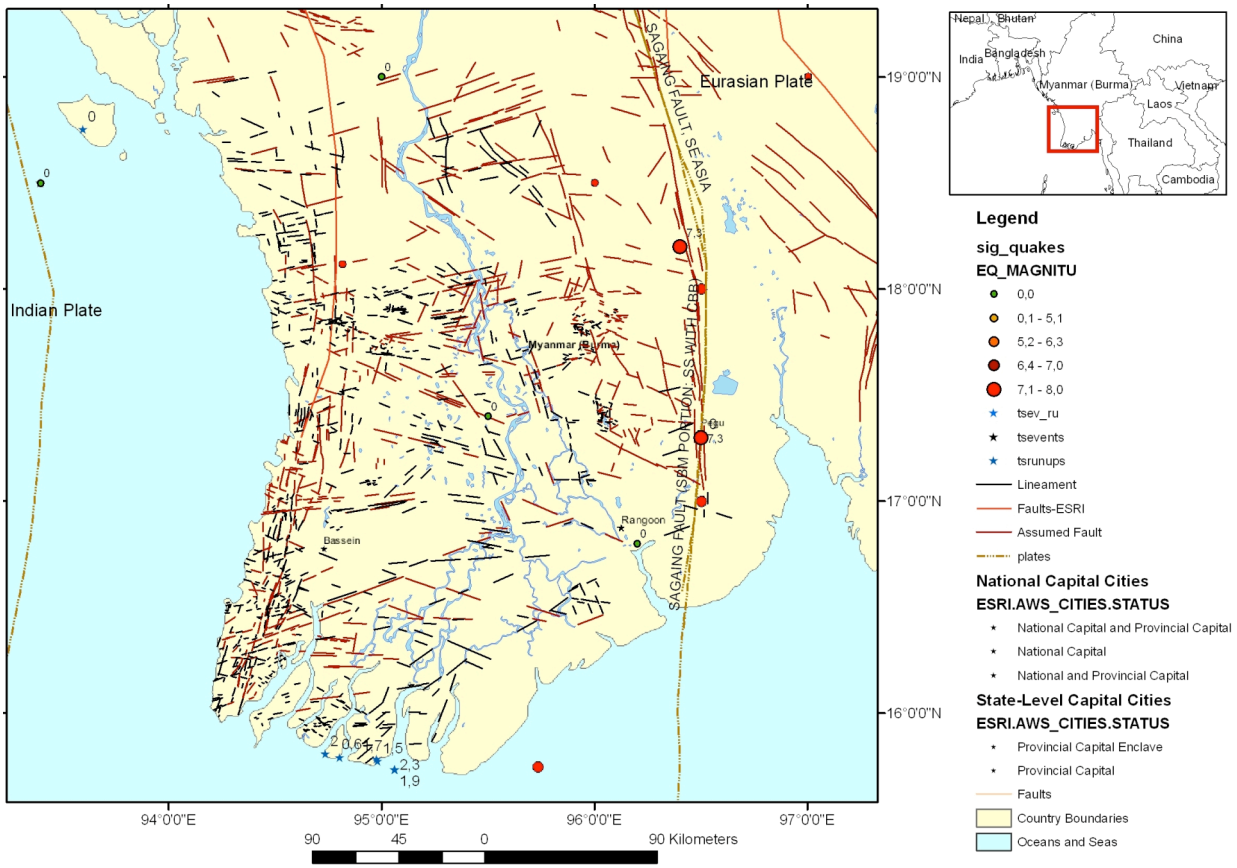

Fig. 7. Geotectonic position of Myanmar
(based on NOAA data, ESRI-data and LANDSAT and SRTM evaluations)

Across Maynmar's lowlands, the Sagaing transform fault defines another plate boundary between the Burma and the Southeast Asean tectonic plates. The seismicity of Maynmar's coastal area is relatively low, perhaps because of a fossil plate boundary. However, occasionally, sudden, intermittent movements along these major active faults have resulted in earthquakes that have affected the region. The historic records show that at least 15 major earthquakes with magnitudes $M \geq 7.0$ have occurred in Myanmar in the last hundred years. Destructive earthquakes occurred in 1930 at Bago, in 1970 at Yangon and in 1975 at Pagan.

3. METHODS AND OBJECTIVES

To further delineate Southwest Maynmar's disaster vulnerability, the present study evaluated remote sensing data from LANDSAT ETM, MODIS and SRTM. **G**eo-**I**nformation**S**ystem (GIS) integrated, comparative analysis of remote sensing data with available geoscientific data was carried out as well as evaluation of reference data. Available geological and geophysical data were collected and integrated as layers into the **G**eo-**I**nformation**S**ystem using ArcView GIS 9.2

and ENVI 4.3 software. Various digital image processing tools delivered by ENVI / CREASO software were tested, to determine the best suited LANDSAT Enhanced Thematic Mapper (ETM) band combinations or contrast stretching parameters. The imageries were merged with the panchromatic Band 8 of LANDSAT ETM to get a spatial resolution of 15 m. For the extraction of tectonic features, standard approaches of digital image processing were used, such as classification for land use and vegetation information. The thermal Band 6 was used to derive and process surface temperature information.

Subsequently, the digital, topographic sets of data were merged and overlain with LANDSAT ETM data. SRTM data provided by the **S**huttle **R**adar **T**opography **M**ission (90 m resolution, interpolated to 50 m) was used to get an overview of the geomorphology of the region and for structural analysis. SRTM data derived image products were used - such as shaded relief and slope degree maps (Theilen-Willige, 2008). The main objectives were to identify more accurately areas vulnerable to floods and suitable locations to build protective shelters.

For the delineation of the tectonic patterns in Southwest Myanmar, the study also considered the support provided by spatial databases. The neotectonic movements were traced by drainage and sedimentological patterns or displacements of strata mapped as linear features (lineaments). Causal or preparatory factors influencing earthquake ground intensity that can be derived by remote sensing and GIS methods were represented as layers in the GIS, in order to detect local site conditions and possible enhancement effects.

4. EVALUATION OF SRTM AND LANDSAT DATA FOR THE DETECTION OF AREAS SUSCEPTIBLE TO FLOODING BY TSUNAMI AND STORM SURGE

In evaluating digital topographic data provided by the Shuttle Radar Topography Mission (SRTM, 2000) one can visualize that the flooding susceptibility is very high in southwest Myanmar since most of the delta region is situated at an elevation almost below 10 m above sea level. Figure 8 provides an overview of the geomorphologic setting. The height level map enhances the V-shaped basin-morphology with large areas below the 10 m elevation from sea level.

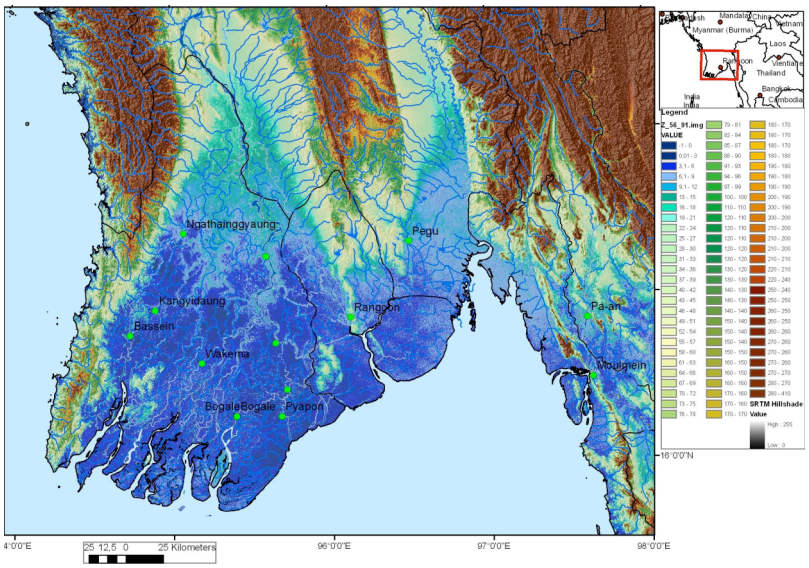

Fig. 8. Height level map (heights in m) of SW-Myanmar

(Note:The ArcGIS 9.2 integrated **flow accumulation** function was applied to calculate surface runoff and lateral flow toward streams using a two-compartment distributed delay function. It routes the flow of water, finding a flow direction for every cell of the elevation grid, following the steepest paths. Flows from cell to cell on the same flow path result in a flow accumulation map in which the value for each cell represents the accumulated flow along a particular path).

Based on the SRTM DEM data, the flow accumulation and the drainage patterns can be calculated as shown in Figure 9. The flow accumulation map provides information of the areas susceptible to flooding.

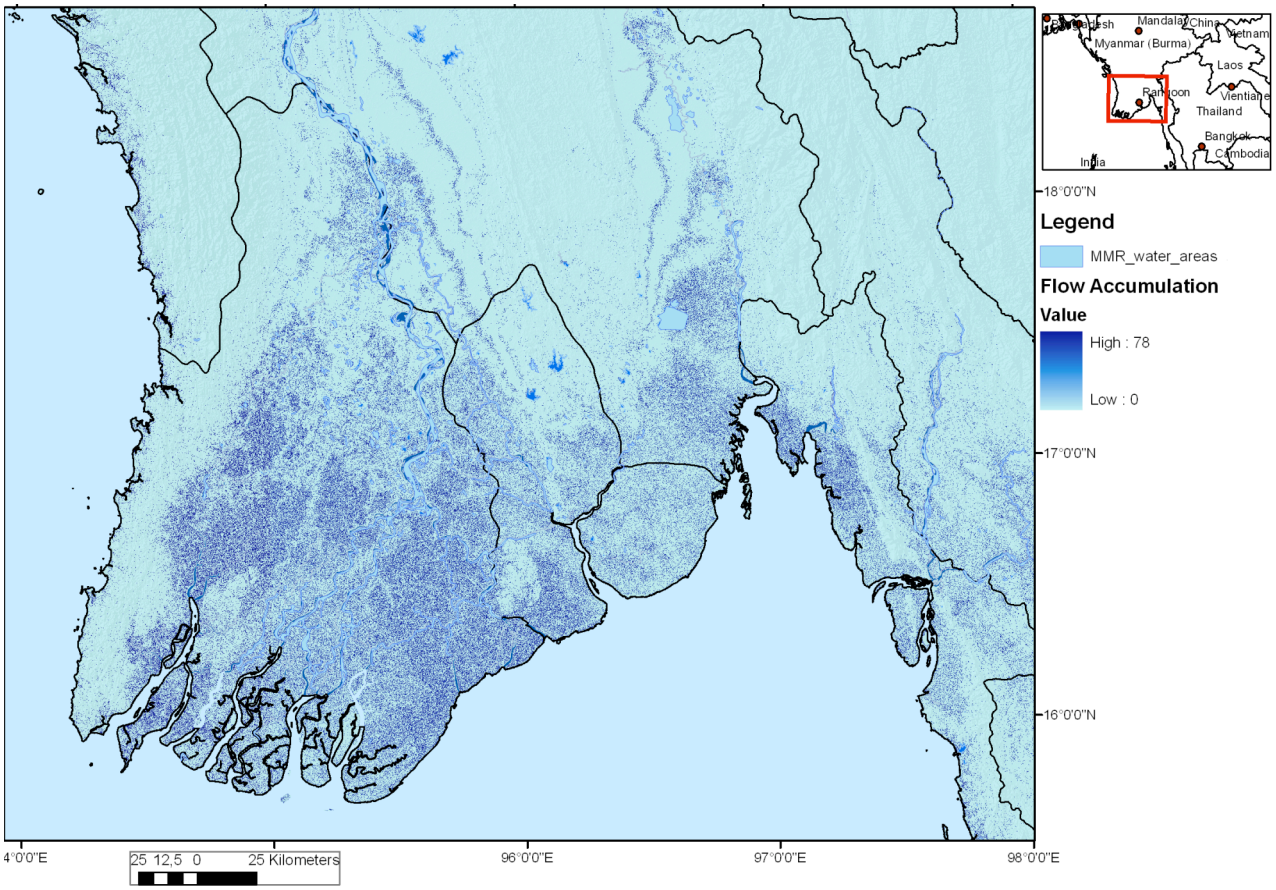

Fig. 9. Flow accumulation map indicating in dark-blue colours the areas most susceptible to flooding.

When comparing satellite data of the western coasts of Myanmar before and after the December 26, 2004 Tsunami, it becomes obvious that the areas below 10 m elevation were particularly vulnerable to flooding (Fig. 10), however, generally not the areas above the 10 m elevation. These areas seen in greenish colours on the LANDSAT scene, which were acquired in 2002, appear in light tones on the image received in April of 2006, because erosion, abrasion and sedimentation caused by the 2004 tsunami. As these images suggest, bays, river mouths, broader riverbeds and estuary plains have probably been more vulnerable to tsunami inundation. Bays and river mouths where tsunamis can enter and inundate are illustrated in Figure 11.

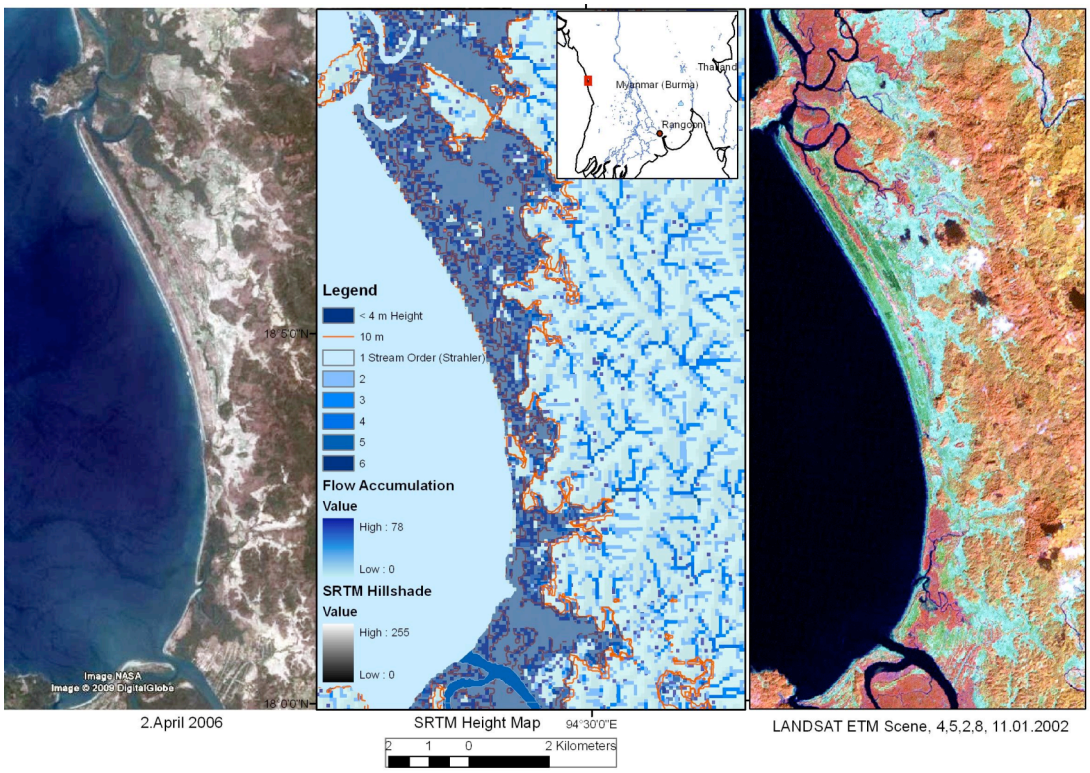

Fig. 10. Comparative analysis of a Google Earth Scene (after the Dec. 26, 2004 Tsunami), SRTM and LANDSAT ETM data (before the Dec. 26, 2004 Tsunami)

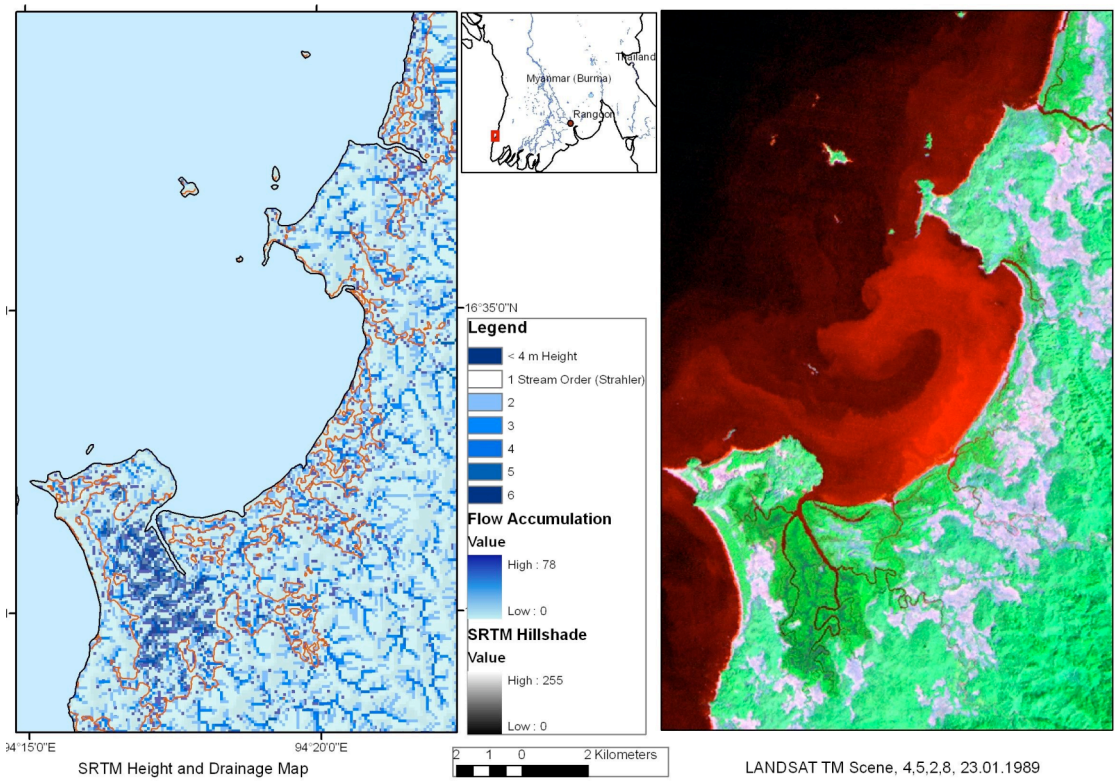

Fig. 11. Streaming pattern at the west coast of Myanmar as seen on LANDSAT imageries

The flooding by Cyclone Nargis had shown that areas above the 10 m elevation had not been flooded (see maps of DLR, ZKI, 2008). Also, evaluation of the satellite data (Fig. 12) indicates that coastal areas above the 10 m elevation were not inundated by the December 26, 2004 tsunami. Therefore, in planning emergency measures such as shelters or evacuation routes, the 10 meter elevation should be considered as being a relatively safe elevation. Figure 13 shows this 10m contour elevation and the areas lower than 4 m above sea level. Based on SRTM height data (interpolated to 50 m ground resolution), LANDSAT ETM data (15 m resolution) and on available high resolution Google Earth data, areas above 10 m were further investigated.

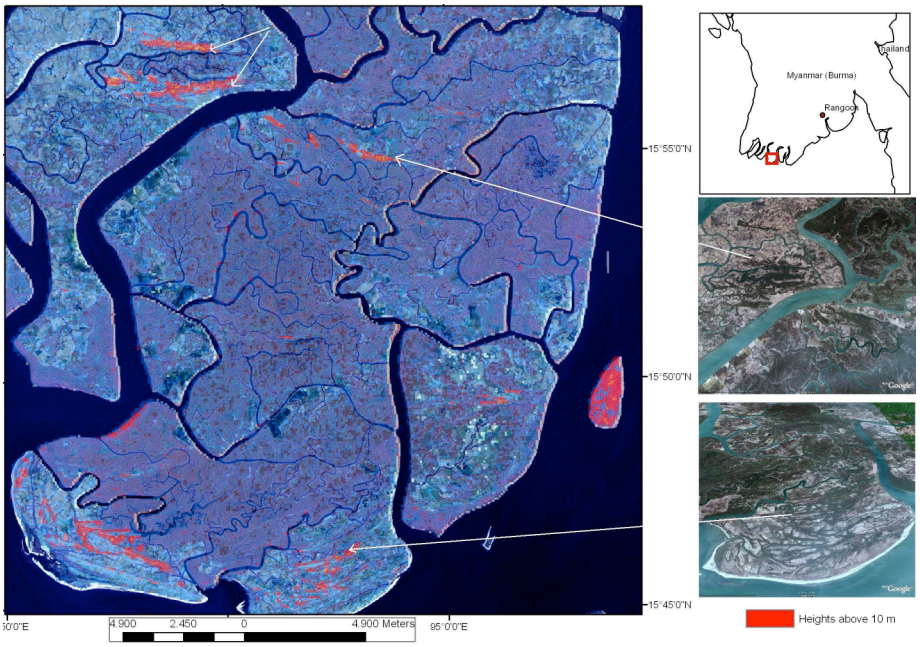

Fig. 12. Areas above 10 m height level

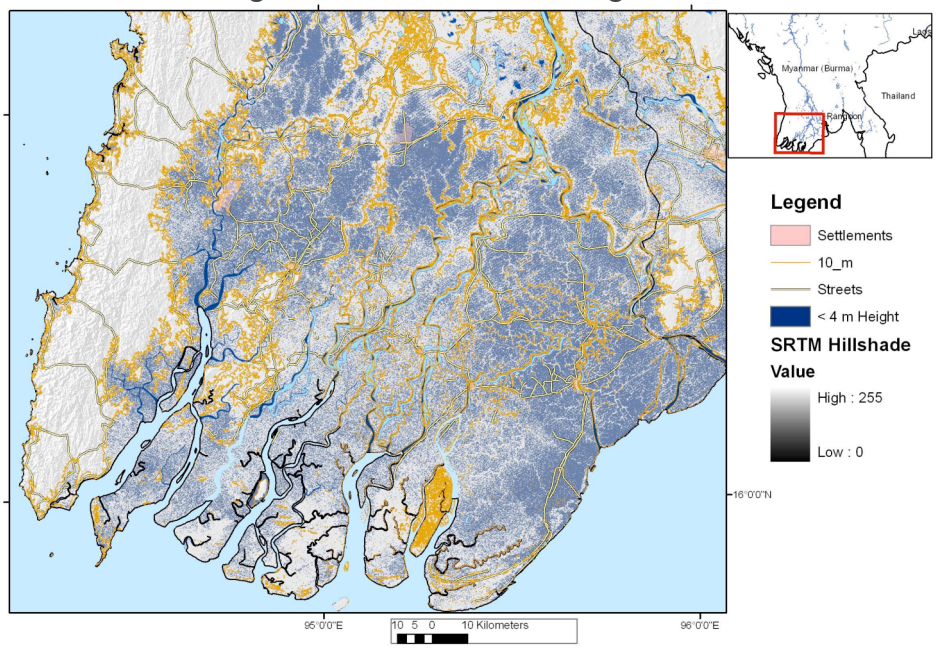

Fig. 13. Elevations below 4 m and 10 meters.

Surveys of the impact of severe and catastrophic floods, such as those caused by Cyclone Nargis, found that small scale flood protection measures such as raising the elevations of houses and shelters should be part of emergency planning (Thomalla et al., 2008). Also necessary is coordination of resources, technical assistance and proper hazard assessment. Measures to be taken should include: flood shelters, evacuation roads above flood levels, planning that takes into account all flood risks and actions that reduce the economic vulnerability of households to flood losses. Criteria for the selection of flood shelter locations should include:

- Elevation heights above 10 m;
- siting on a morphological watershed;
- a distance greater than 1 km from larger rivers;
- separation of shelters not to exceed 3 to 4 km (if possible).

Analysis of satellite imageries makes it obvious that in flat delta areas with dense river patterns the selection of locations to build shelters is difficult. However, analysis of the drainage patterns can help select small "islands" with elevations greater than 10 meters that could be used for such shelters. Thus, the best-suited locations for shelters were mapped in Figures 14 and15 and distances to each other were calculated (Fig. 16). However, with often-limited financial resources, a possible low or no cost emergency solution would be to construct such shelters with earth-bags (Fig. 17).

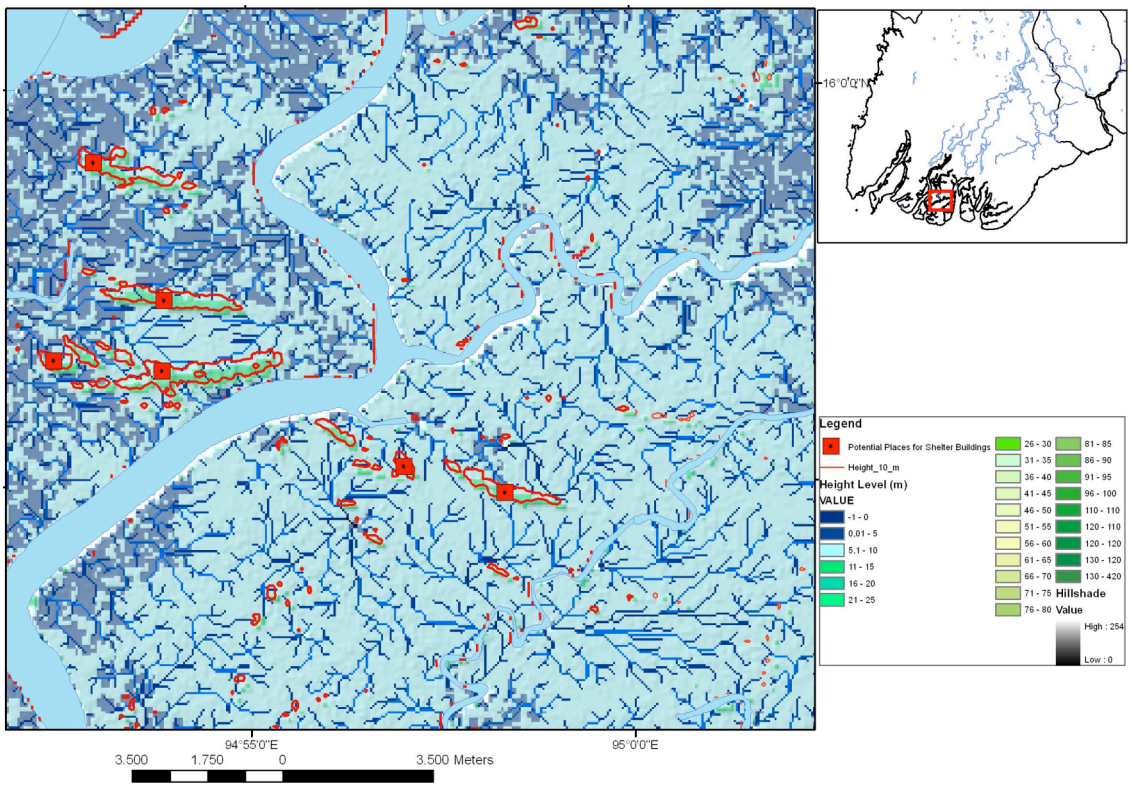

Fig. 14. Possible flood shelter locations with elevations above 10 m in height.
The drainage pattern was calculated based on SRTM data (interpolated to 50 m Grid resolution)

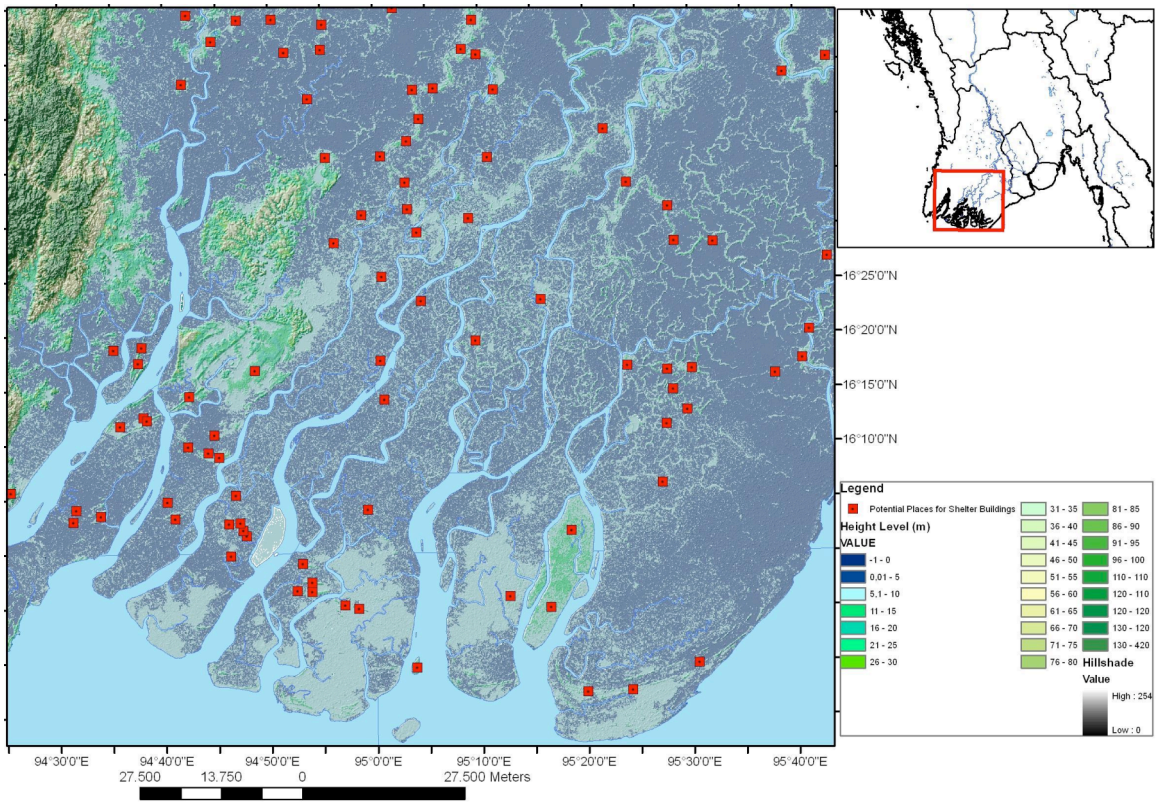

Fig. 15. Distribution of possible tsunami and cyclone surge shelter locations in the Irrawaddy delta area.

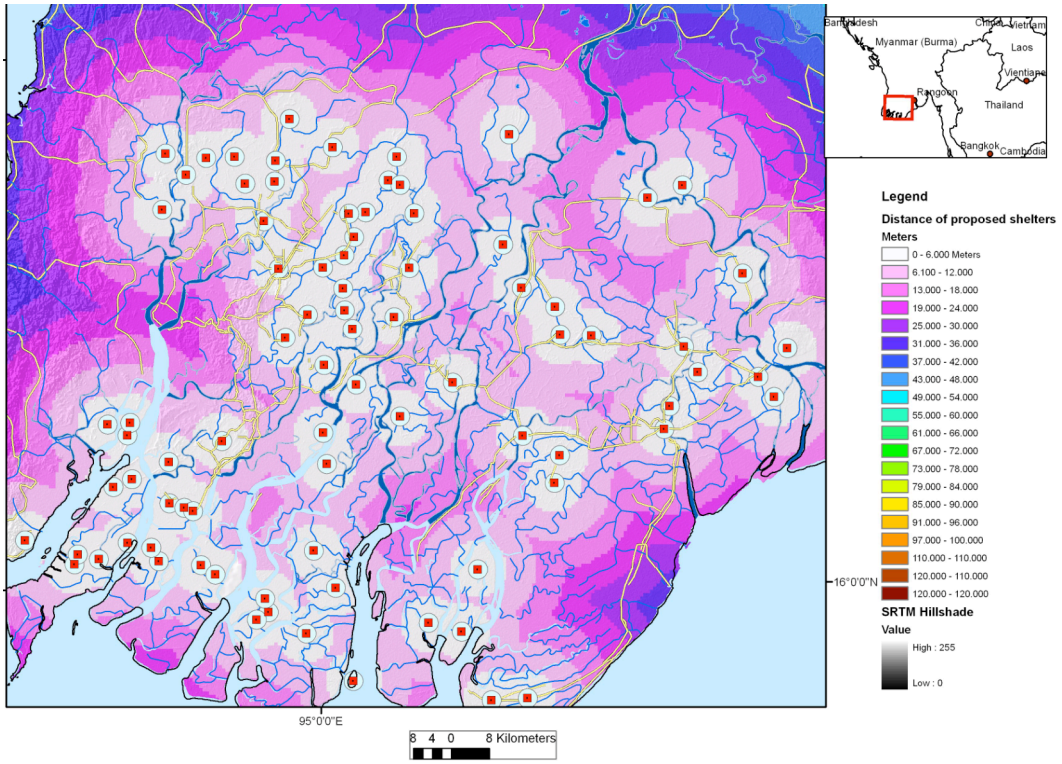

Fig. 16. Distance of potential shelter locations to each other.

Fig. 17. Proposed low cost shelter buildings (from Khalili and Hart, http://www.earthbagbuilding.com/articles/earthbagbuilding.htm)

Sandbags have long been used to form strong, protective barriers or for flood control. For this reason sandbags could be useful to create housing or shelters. The walls of such structures are massive, strong and resist severe weather and fire. Such structures can be erected simply and quickly with readily available components. Burlap bags have been traditionally used for this purpose, and they work fine until they rot. For more permanent structures, such bags should be covered with some kind of protective plaster (according to Khalili, see link in caption of Fig. 15). Still fire is one of the main causes of disasters in Myanmar as most homes, normally in close proximity to each other, are build with bamboo and thatch roofing – which are the cheap and readily available traditional building materials. (http://www.adrc.or.jp/countryreport/MMR/2002/CR_MMR2002.htm).

5. EVALUATION OF LANDSAT DATA FOR THE DETECTION OF ENVIRONMENTAL CHANGES

Since environmental conditions play a significant role in assessing flooding vulnerability, remote sensing data was used to analyze the distribution of vegetation and land use changes. The

destruction of huge areas of coastal mangroves around the Irrawaddy River delta in Myanmar in the last few decades has amplified the flooding risk and has worsened potential devastation in this region. As people have been pushing closer towards coastal areas, the combination of new settlements and the ongoing deforestation for the creation of fishponds and farmland, has increased significantly the vulnerability to flooding by severe tsunamis or cyclones (UNOSAT, 2008). Lumbering operations have also reduced forest density. A comparative analysis of the LANDSAT imageries from the Irrawaddy-Delta clearly shows the decrease of the mangrove forest (red colours) between 1978 and 2000 (Fig. 18). Coastlines that have lost mangroves have also lost their protection from future tsunamis.

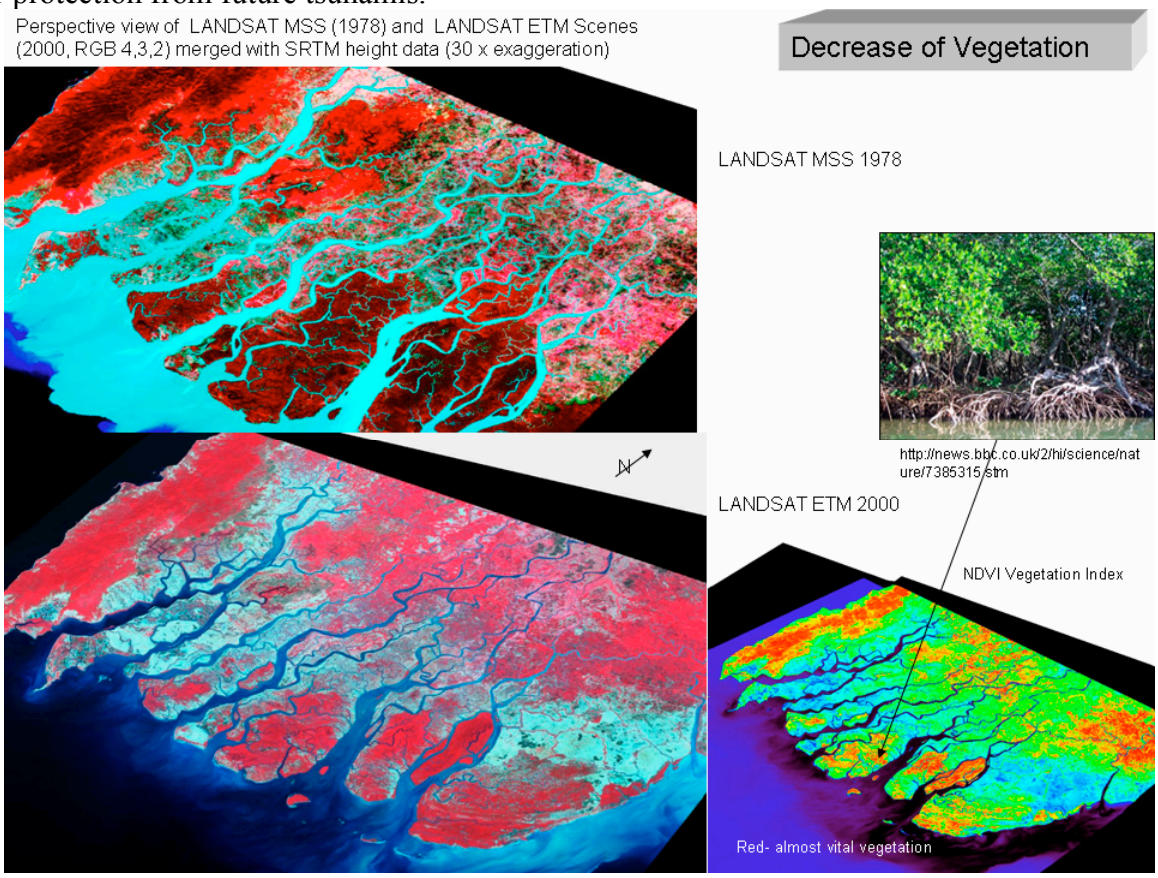

Fig. 18. LANDSAT imageries from 1978 and 2000 showing the decrease of forests

6. EVALUATION OF SRTM AND LANDSAT DATA FOR THE DETECTION OF AREAS SUSCEPTIBLE TO HIGHER EARTHQUAKE INTENSITIES AND TO EARTHQUAKE INDUCED SECONDARY EFFECTS

One important factor that must be accounted for in local earthquake hazard studies is a site's surface and subsurface conditions and expected response in the form of ground motions. Earthquake damage may vary locally, since it depends on the types of structures that are built and the subsurface ground conditions, proximity to faults and fractures, lithology, and the ground water table (Gupta, 2003). Remote sensing data can be used to map factors that are related to the occurrence of higher earthquake intensities and earthquake-induced secondary effects, such as liquefaction or landslides.

Past earthquakes indicate that damage and loss of life are mostly concentrated in areas that are underlain by deposits of soft soils and high ground water tables - as exemplified by the Mexico City earthquake of 1985 (Steinwachs, 1988; Pararas-Carayannis, 1985). Soft soils tend to amplify shear waves and ground shaking. Wetlands have a higher damage potential during earthquakes due to longer and higher vibrations. The fundamental phenomenon responsible for the amplification of ground motions over soft sediments is the trapping of seismic waves due to differences between sediments and the underlying bedrock. With horizontal stratigraphy, the trapping affects body waves, which travel up and down through the surface layers. When the structure is either two or three-dimensional, lateral heterogeneities are present (such as thickness variations in sediment-filled valleys), this trapping also affects the surface seismic waves. The interferences between the trapped waves lead to resonance patterns, the shape and the frequency of which are related with the geometrical and mechanical characteristics of the structure (Ehret & Hannich, 2004).

For example, although the epicenter of the 1985 earthquake was more than 300 Km away from Mexico City, the downtown area experienced surface seismic waves with accelerations of up to 17% g. with peaks concentrated at 2 sec. period. The maximum estimate of the Modified Mercalli intensity was IX. The extreme liquefaction and damage to new buildings which occurred in downtown Mexico City was attributed to the monochromatic type of seismic wave with a predominant period which caused 11 harmonic resonant oscillations of buildings and caused many to collapse (Pararas-Carayannis, 1985). The ground accelerations were enhanced within a layer of 30 ft. of unconsolidated sediments (of silt and volcanic clay) underneath downtown Mexico City, which had been the site of the historic Lake Texcocoa in the 15th Century. These example illustrate that indeed earthquake damage can be amplified by focused seismic waves along fault zones or layers of sediments. Seismic waves travelling in the subsurface might be refracted at sharp discontinuities such as faults and may have a cumulative effect that influences their intensity and therefore cause greater damage. Similarly, fault segments, their bends and intersections are more likely to concentrate stress and amplify intensity. Intersecting fault zones could cause constructive interference of multiple seismic wave reflections at the boundaries with surrounding rocks**.** The highest risk occurs at junctions of differently oriented, intersecting ruptures. Dense fault zones consisting of distinct segments can be considered to be more dangerous in terms of seismic risk than those where active ruptures are scattered over a larger area. Such aareas can be expected to experience greater earthquake intensities because of focused seismic wave amplification along intersecting fault zones and additional soil amplification. Lineament analysis can help detect near-surface faults and fracture zones and thus provide clues as to where cumulative effects can be expected. Fig. 19 shows the areas with the highest density of linear features assumed to be related to fault zones in South-western Myanmar.

Finally, the Irrawaddy delta was formed by deposition of sediments carried by major rivers and tributaries. The distribution of the sedimentary cover in this region can be correlated with areas having a slope gradient of less than 5°. By extracting elevations below the 4 m level, the location of areas with high ground-water tables can be determined. Slopes with higher slope gradient (> 20°) are generally more vulnerable to mass movements. Slope gradient maps help detect areas where such mass movements are likely to occur. Areas with intersecting, larger lineaments are probably exposed to relatively higher earthquake intensities by the stronger earthquakes.

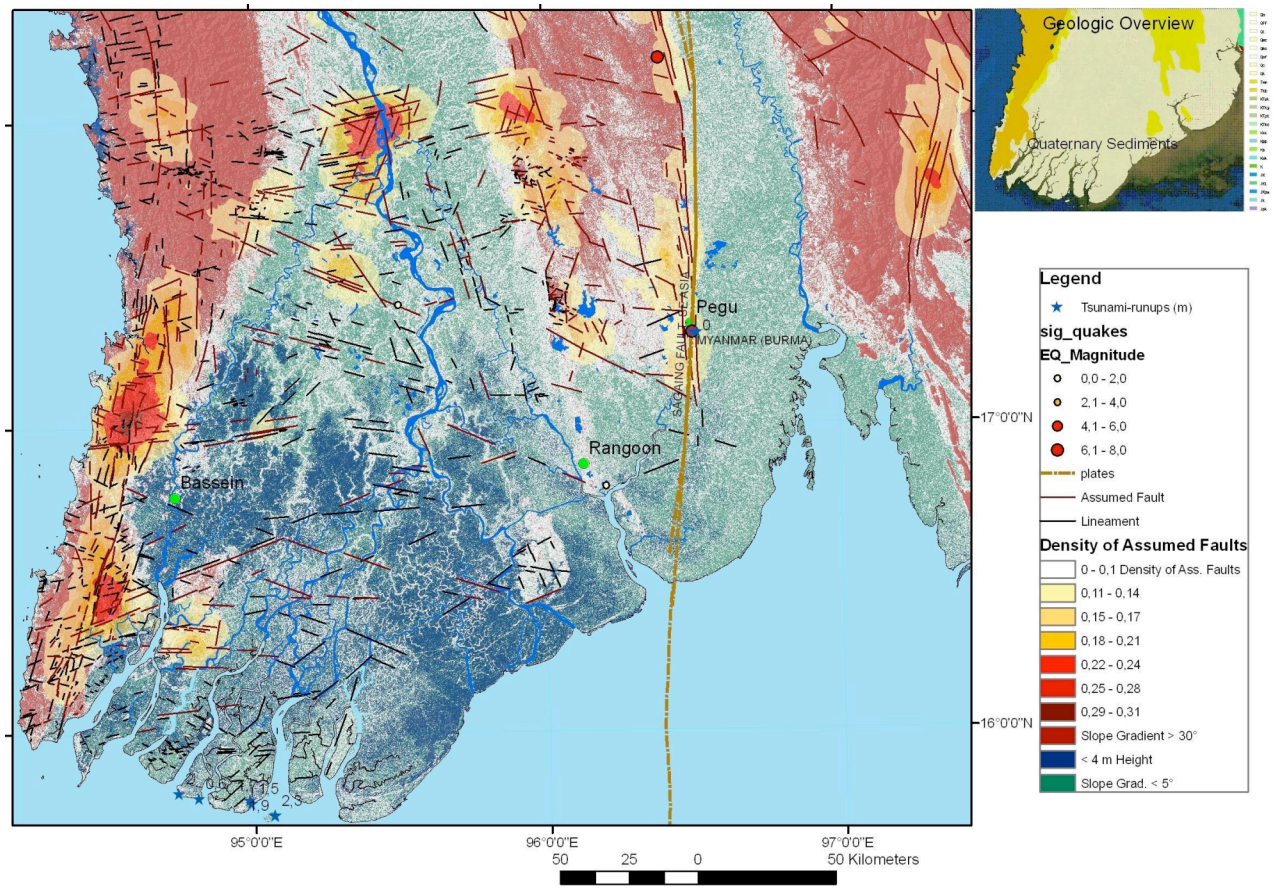

Fig. 19. Areas probably susceptible to higher earthquake intensities due to unconsolidated, sediments, near surface fault density and higher groundwater tables
Linear geomorphologic features are mapped as lineaments, often related to subsurface structures.
Geologic Overview according to One Geology Portal (http://portal.onegeology.org/)

7. CONCLUSIONS

The use of satellite SRTM, LANDSAT and GOOGLE EARTH data, integrated into GIS methodology, helped map the areas most susceptible to flooding in the southwest region of Burma/Myanmar. The analysis helped identify coastal areas that are vulnerable to potential tsunami and storm surge inundation. Such collection of data represents a promising new tool for examining and identifying suitable locations for cyclone flooding and tsunami shelters. The use of the described GIS methodology can help visualize some of the factors that influence local earthquake intensities or are capable of generating secondary hazards. The methodology can also help determine probable fault zones, areas of higher earthquake damage risk, areas with higher groundwater tables and higher slope gradients where mass movements could occur.

8. REFERENCES

Asian Disaster Reduction Center (2003). Country Report 2003.
http://www.adrc.or.jp/countryreport/MMR/2002/CR_MMR2002.htm

Democratic Voice of Burma -DVB (2005). TSUNAMI: Did Burma Escape the Consequences?
http://www.burma.no/noop/file.php?id=2288
http://www.burmacampaign.org.uk/PDFs/Tsunami_Damage_(DVB).pdf

Ehret, D.& Hannich,D.(2004). Seismic Microzonation based on Geotechnical Parameters – Estimation of Site Effects in Bucharest (Romania). EOS Trans. AGU, 85 (47), Fall Meet. Suppl., Abstract S43A-0972; San Francisco.
http://www2.agk.unikarlsruhe.de/projekte/projekte_ing/mikrozonierung/Literatur_PDFs/Mikrozonierung_Bukarest/Ehret_et_al_2004_AGU.pdf

German Aerospace Center (DLR): Tropical Cyclone Nargis: ZKI maps flooding in Myanmar,
http://www.zki.caf.dlr.de/applications/2008/myanmar/150_en.html

Gupta, R.P. (2003). Remote Sensing Geology. Springer Verlag, Berlin, Heidelberg, New York

Hart, K.and Geiger,O.: An Earthbag Emergency Shelter .-
http://www.earthbagbuilding.com/emergency/emergencyshelter.htm

Kyaw Kyaw Lin (2008). Seismic and Tsunami Activities in Myanmar.
July 2007-March 2008 JICA Training Course, Nagoya University
http://www.seis.nagoya-u.ac.jp/kimata/jica/kyawkyaw.pdf

Khalili ,N.: Emergency Sandbag Shelter, Eco-Village (Training Guide), California Institute of Earth Art and Architecture (Cal-Earth), in Hesperia, CA,USA
http://www.calearth.org/
http://www.earthbagbuilding.com/projects/baraka.htm
http://www.earthbagbuilding.com/articles/earthbagbuilding.htm

McKeon, J., Fengler,W. & A. Zaki Fahmi (2008). Comparing cyclone Nargis in Myanmar with the tsunami in Indonesia – August 27th, 2008, IDRC, Davos
http://www.proventionconsortium.org/themes/default/pdfs/M&E/IDRC08_M&E_Fengler-McKeon.pdf

UNOSAT (2008). Hyperlinked Overview of Building Damages in 18 Selected Villages, Southern Ayeyarwady Delta, Myanmar. http://unosat.web.cern.ch/unosat/

Pararas-Carayannis, G. 2009. Assessment of Potential Tsunami Generation in China's Bohai Sea from Direct geotectonic and Collateral Source Mechanisms. Science of Tsunami Hazards, Vol. 28, No. 1, pages 35-66 (2009)

Pararas-Carayannis, G. 2008. Cyclone "Nargis" of May 2-3 in Myanmar (Burma). http://www.drgeorgepc.com/Cyclone2008Burma.html

Pararas-Carayannis, G. 2007a. Assessment of India's Vulnerability from Potentially Destructive Earthquakes and Tsunamis – Land Use and engineering Guidelines in Alleviating Future Disaster Impacts and Losses. Proceedings of IC-NHDM-2007, pp 1-23, 12-14 December 2007, Hyderabad, India.

Pararas-Carayannis, G. 2007b. The Earthquakes and Tsunami of September 12, 2007 in Indonesia. http://www.drgeorgepc.com/Tsunami2007Indonesia.html

Pararas-Carayannis, G. 2005a. The Great Earthquake and Tsunami of 26 December 2004 in Southeast Asia and the Indian Ocean
http://www.drgeorgepc.com/Tsunami2004Indonesia.html

Pararas-Carayannis, G. 2005b. Great Earthquake and Tsunami of 28 March 2005 in Sumatra, Indonesia
http://drgeorgepc.com/Tsunami2005ndonesia.html

Pararas-Carayannis, G. 1985. The Great Earthquake of 19 September 1985 and the Major Earthquake of 21 September 1985 in Mexico – Tsunami Source Mechanism. Report to Intergovernmental Oceanographic Commission – UNESCO; Tsunami Newsletter, Vol. XVIII, No. 2, 1985; ITIC Progress Reportfor 1985-1987. XI Session of the International Coordination Group for the Tsunami Warning System in the Pacific, Beizing, China, Aug 1987
http://www.drgeorgepc.com/Tsunami1985Mexico.html

PONREPP (2008). Shelter and Settlements. PONREPP sector chapter (final – 29 Nov 2008)
http://myanmar.humanitarianinfo.org/Shelter/Strategy/Shelter_Plan_final%20291108.pdf

Steinwachs M.(1988). Das Erdbeben am 19.September 1985 in Mexiko – Ingeneieurseismologische Aspekte eines multiplen Subduktionsbebens. In: Steinwachs M. (ed). Ausbreitungen von Erschütterungen im Boden und Bauwerk. 3.Jt. DGEB, Trans Tech.Publications,1988, Clausthal

Theilen-Willige,B. (2008). Tsunami Hazard Assessment in the Northern Aegean Sea.- SCIENCE OF TSUNAMI HAZARDS. The International Journal of The Tsunami Society,Vol. 27, Number 1, 1-16, Published Electronically 2008, http://tsunamisociety.org/271Willige.pdf

Theilen-Willige, B., Mulyasari Sule, F.& Wenzel H.(2008). Environmental Factors derived from Satellite Data of Java, Indonesia. in: Christian Boller, Fu-Kuo Chang & Jozo Fujino (Editors), 2008: Encyclopedia of Structural Health Monitoring.- John Wiley and Sons,Ltd., Chichester,UK, 2343-2354

Theilen-Willige, B. (2006). Remote Sensing and GIS Contribution to Tsunami Risk Sites Detection in Southern Italy. Photogrammetrie – Fernerkundung – Geoinformation-PFG, 2, 103-114.

Thomalla, F., Chadwick,M., Shaw,S. and Miller,F. (2008).Cyclone Nargis What are the Lessons from the 2004 Tsunami for Myanmar's Recovery? - Risk, Livelihoods and Vulnerability Programme. May 2008, http://www.sei.se/pubs/Nargis_20080527d.pdf

TUN, P. P.: Hypocenter relocation and moment tensor analysis of earthquakes in Myanmar – toward the investigation of the Burma subduction-Sagaing fault system. Analysis of earthquakes 2008-11-13
http://iisee.kenken.go.jp/syndb/?action=down&p=200810207552663f.pdf&t=application/pdf&n=MEE07164_Pa_Pa_Tun_2008.pdf

Shapefiles:

National Oceanic and Atmospheric Administration
http://map.ngdc.noaa.gov/website/seg/hazards/viewer.htm

Satellite Data:
SRTM DEM: ftp://e0srp01u.ecs.nasa.gov/srtm/version1/Eurasia/LANDSAT
ETM Daten:
http://glcfapp.umiacs.umd.edu:8080/esdi/index.jsp

Geologic Maps:

Digital Geologic Map of Southeast Asia, 1:2,000,000 –Second Edition– 5 Edition Published in 2004.
http://portal.onegeology.org/
http://geodata1.geogrid.org/mapserv/CCOP_Combined_Bedrock_and_Superficial_Geology_and_Age/wms?

A New Method to Analyze the Tsunami Incitement Process and Site-selection for Tsunami Observations in China's Eastern Sea

Yuanqing Zhu[1],
Shuangqing Liu,
Yanlin Wen,
Yan Xue

[1]*Professor, Earthquake Administration of Shanghai Municipality;*
National Geophysical Observatory at Sheshan, Shanghai, 200062, China
Email: yqzhu@sbsn.net, liushuangq05@mails.gucas.ac.cn

ABSTRACT

In this paper, we present a CONTROL volume model for tsunami incitement process by combining the Navier-Stokes equation, the jet theory and relative velocity model. We conclude that the initial condition for tsunami propagation simulation is equivalent to the static near-field seismic displacement of earthquake that induces the tsunami. The error analyzed from this method is only about 1 percent for a common seafloor earthquake, and it is consistent with the result of Ansys/Ls-dyna numerical analysis. EDGRN/EDCMP and COMCOT program provide some new acquirement for the tsunami studies. In the second part of the paper, we develop a site-selection method for anchor-grounded tsunami observation in Chinese eastern sea.

KEYWORDS: N-S equation, Jet theory, Relative velocity, Optimal analysis

INTRODUCTION

At present, there is little solid and constructive study on the tsunami near-field characteristics or initial condition of propagating simulation. The classic paper by Gutenberg (1939) showed that most previous studies on tsunami were rested on the qualitative approaches. The essential study about the tsunami near-field characteristics maybe owned to Kajiura (1970). He separated the energy pattern from the non-homogeneous wave equation. Most of subsequent tsunami propagation researches all made a statement to cite its conclusion, albeit there was a defect in that article, which the energy of dynamic retrieved from the incitement source was completely independent of the water depth. Based on the linear shallow water wave equations, Todorovska et al. (2001,2002,2003) derived analytical integral solution for tsunami incited by a landslide. Ward (2003) deduced, with traditional seismological procedures, some 1st-order approximate integral formula of results including patterns of incitement of the landslide, celestial impact, and seismic tensor combined with focal geometry parameters. Ohmachi et al. (2001) utilized BEM and FDM methods to simulate a tsunami incitement process by a fault rupture. Partial interrelated experiments and corresponding numerical calculations were carried out by Grilli et al. (2001,2004,2005) and Liu et al. (2005). Except above, most researches put focus on the propagation and simulation algorithm, and paid little attention to the "initial value problem." We present a new way to analyze the tsunami near-field characteristics. Also, in the part 2, we discuss the method for selecting a best site for anchor-grounded tsunami observational station.

PART (I) INITIAL VALUE PROBLEM

Mathematical Model

In general fluid mechanism theory, the Navier-Stokes momentum equation is

$$\frac{\partial \boldsymbol{V}}{\partial t} + \boldsymbol{V}\cdot\nabla\boldsymbol{V} = \boldsymbol{f} + \frac{1}{\rho}\nabla\cdot(T_{ij}\boldsymbol{e}_i\boldsymbol{e}_j) \tag{1}$$

Where, $\boldsymbol{V}$ is velocity vector, $\boldsymbol{f}$ is body force, $\boldsymbol{\rho}$ is density, T_{ij} is a tenor, and $\boldsymbol{e}_i$, $\boldsymbol{e}_j$ is unit directional vector. This is a differential equation. Along with the continuous equation: $\frac{\partial \rho}{\partial t} + \nabla\cdot(\rho\boldsymbol{V}) = 0$, it constitutes the traditional foundation of fluid mechanism theory. Especially, they are suitable for the shallow wave studies. However, these equations only allow researchers to derive the complex integral solutions to the wave initial deformation, it is still difficult to obtain the relationship between the tsunami and its incitement source, even for the case in which the hypothesis source is very simple. But if we consider the integral equation form of momentum is

$$\int_D \frac{\partial(\rho\boldsymbol{V})}{\partial t}d\mathrm{V} + \oiint_{\Sigma}\rho\boldsymbol{V}(\boldsymbol{V}\cdot\boldsymbol{n})dA = \int_D \rho\boldsymbol{f}d\mathrm{V} + \oiint_{\Sigma}\boldsymbol{T}_n dA \tag{2}$$

Where $\boldsymbol{n}$ is a normal vector. We can develop a CONTROL volume model to analyze it.

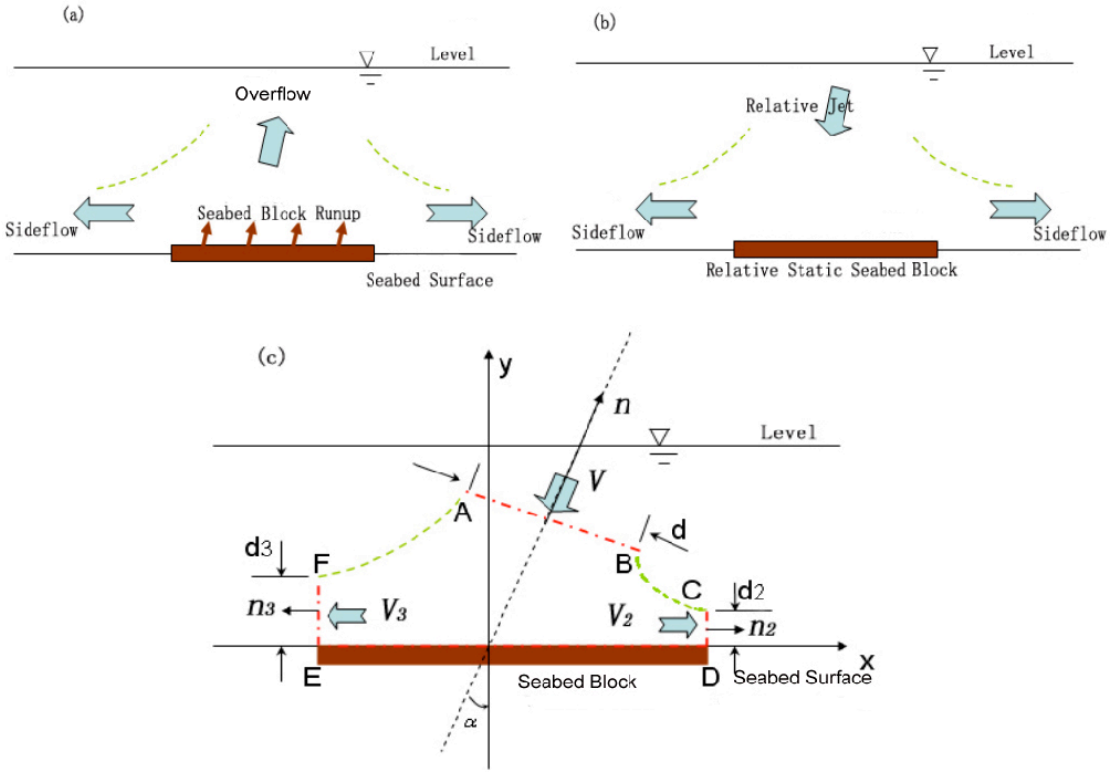

Fig .1 The sketch of two-dimensional sea disturbance by seabed run-up
(a) Incitement of seabed run up, (b) The model of jet on the approach of relative velocity analysis,
(c) The Cartesian-ordinates description of steady jet model and CONTROL volume.

When a seafloor earthquake takes place, the nearby seabed would lift up and pull down, the water column above the seabed would be disturbed and tsunami could possibly be generated. We simplify the tsunami incitement process as the Fig.1 and only consider the seabed lift-up case. We assume that the sea bed lifts up with a constant velocity until the earthquake rise time ends. The sea water is uplifted with slower velocity $\boldsymbol{V}_1$ than that of sea bed $\boldsymbol{V}_0$. We then define the relative velocity $\boldsymbol{V}=\boldsymbol{V}_1-\boldsymbol{V}_0$, and the overflow can take as a relative jet flow with velocity $\boldsymbol{V}$ (see the fig. 1(b)). It can be farther modified as the CONTROL volume model in the fig. 1(c), in which $\boldsymbol{V}_2$ and $\boldsymbol{V}_3$ represent the velocities of two right-about side flows respectively.

The region closed by AB-BC-CD-DE-EF-FA (figure 1c) is the CONTROL volume. The reference frame is x-axis trends along the sea bed, y-axis goes up, and z-axis is a unit length. The jet flow, with a width **d**, impacts the sea bed with an angle of incidence $\boldsymbol{\acute{a}}$. In the specified CONTROL volume, we assume the body force $\boldsymbol{f}$ is zero and the flow is uncompressible, the equation (2) can be rewritten as

$$\oiint_{\Sigma}\rho\boldsymbol{V}(\boldsymbol{V}\cdot\boldsymbol{n})dA=-\oiint_{\Sigma}p\boldsymbol{n}dA \tag{3}$$

and

$$\oiint_{\Sigma}\rho\boldsymbol{V}(\boldsymbol{V}\cdot\boldsymbol{n})dA=\iint_{AB}\rho\boldsymbol{V}(\boldsymbol{V}\cdot\boldsymbol{n})dA+\iint_{BC+FA}\rho\boldsymbol{V}(\boldsymbol{V}\cdot\boldsymbol{n})dA+\iint_{CD}\rho\boldsymbol{V}_2(\boldsymbol{V}_2\cdot\boldsymbol{n})dA+\iint_{EF}\rho\boldsymbol{V}_3(\boldsymbol{V}_3\cdot\boldsymbol{n})dA \tag{4}$$

In equation (4), $\boldsymbol{V}\cdot\boldsymbol{n}=0$ on the BC+FA boundary, because they are the jet flow side and the normal velocity equals zero. Therefore, we have

$$\begin{aligned}\oiint_{\Sigma}\rho\boldsymbol{V}(\boldsymbol{V}\cdot\boldsymbol{n})dA&=-\rho\boldsymbol{V}Vd+\rho V_2^2d_2\boldsymbol{i}-\rho V_3^2d_3\boldsymbol{i}\\&=-\rho V^2d(\boldsymbol{i}\sin\alpha+\boldsymbol{j}\cos\alpha)+\rho V_2^2d_2\boldsymbol{i}-\rho V_3^2d_3\boldsymbol{i}\end{aligned} \tag{5}$$

Where V_2, V_3 are unbeknown parameters. Making use of the steady Bernoulli formula

$$p_a+\frac{\rho V^2}{2}=p_a+\frac{\rho V_2^2}{2}=p_a+\frac{\rho V_3^2}{2} \tag{6}$$

Where, p_a is the environmental pressure. We deduce the result of $V=V_2=V_3$. Furthermore, $Vd=V_2d_2+V_3d_3=V(d_2+d_3)$ by analysis of continuous equation, and $d=d_2+d_3$ subsequently.

Now we calculate the sum of pressure with

$$-\oiint_{\Sigma}p\boldsymbol{n}dA=-\iint_{AB+BC+CD+EF+FA}p_a\boldsymbol{n}dA-\iint_{DE}p\boldsymbol{n}dA \tag{7}$$

$-\iint_{DE}p\boldsymbol{n}dA$ represents the force that the seabed acts on the water. Given the pressure of the down-toward side of sea bed is p_{struc}, the sum of force on the sea bed (ED length) is

$$\boldsymbol{F}=\iint_{DE}(p-p_{struc})\boldsymbol{n}dA \tag{8}$$

Substitute p into equation (7), we have

$$\begin{aligned} \boldsymbol{F} &= \iint_{DE}(p - p_{struc})\boldsymbol{n}dA = \oiint p\boldsymbol{n}dA - \iint_{AB+BC+CD+EF+FA} p_a\boldsymbol{n}dA - \iint_{DE} p_{struc}\boldsymbol{n}dA + \iint_{DE} p_a\boldsymbol{n}dA - \iint_{DE} p_a\boldsymbol{n}dA \\ &= \oiint p\boldsymbol{n}dA - \oiint p_a\boldsymbol{n}dA - \iint_{DE} p_{struc}\boldsymbol{n}dA + \iint_{DE} p_a\boldsymbol{n}dA \end{aligned} \tag{9}$$

The second item on the right is equal to zero as it integrates on a closed facet. And equation (9) can be simplified as

$$\boldsymbol{F} = \oiint p\boldsymbol{n}dA - \iint_{DE} p_{struc}\boldsymbol{n}dA + \iint_{DE} p_a\boldsymbol{n}dA \tag{10}$$

Substitute equations (10), (5) into (3):

$$-\rho V^2 d(\boldsymbol{i}\sin\alpha + \boldsymbol{j}\cos\alpha) + \rho V^2 d_2\boldsymbol{i} - \rho V^2 d_3\boldsymbol{i} = -\boldsymbol{F} - \iint_{DE} p_{struc}\boldsymbol{n}dA + \iint_{DE} p_a\boldsymbol{n}dA$$

then

$$\begin{aligned} \boldsymbol{F} &= \rho V^2 d(\boldsymbol{i}\sin\alpha + \boldsymbol{j}\cos\alpha) - \rho V^2 d_2\boldsymbol{i} + \rho V^2 d_3\boldsymbol{i} - \iint_{DE} p_{struc}\boldsymbol{n}dA + \iint_{DE} p_a\boldsymbol{n}dA \\ &= -\iint_{DE} p_{struc}\boldsymbol{n}dA + \iint_{DE} p_a\boldsymbol{n}dA + (\rho V^2 d\cos\alpha)\boldsymbol{j} - (\rho V^2 d_2 - \rho V^2 d_3 - \rho V^2 d\sin\alpha)\boldsymbol{i} \end{aligned} \tag{11}$$

Considering the water is approximately an idealized fluid, only the normal force exists on the seabed, and the x-axis component of $\boldsymbol{F}$ is zero.

$$\boldsymbol{F} = -\iint_{DE} p_{struc}\boldsymbol{n}dA + \iint_{DE} p_a\boldsymbol{n}dA + (\rho V^2 d\cos\alpha)\boldsymbol{j} \tag{12}$$

$$d_2 - d_3 = d\sin\alpha \tag{13}$$

Since $d_2 + d_3 = d$, we have $d_2 = \dfrac{d(1+\sin\alpha)}{2}$ and $d_3 = \dfrac{d(1-\sin\alpha)}{2}$.

Hereby, the inter-force on the interface between water and sea bed can be written as

$$\boldsymbol{F}_{\text{int}eraction} = (-\rho V^2 d\cos\alpha)\boldsymbol{j} - \iint_{DE} p_a\boldsymbol{n}dA \tag{14}$$

Therefore, $\boldsymbol{F}_{\text{interaction}}$ is a function of the fluid density, relative velocity and incidence angle of jet, the pressure of environment, and the ED length of seabed incitement. If we assume the length of ED is l, $d = \kappa l$, $\kappa \in (0,1)$ is a ratio (we define it as a factor of effective width of jet flow), then

$$\boldsymbol{F}_{\text{int}eraction} \approx (-\rho V^2 \kappa l\cos\alpha)\boldsymbol{j} - l\rho gh\cdot\boldsymbol{n}$$

$$\| F_{\text{int}eraction} \|_1 = \rho V^2 \kappa l\cos\alpha + l\rho gh = \rho l(\kappa V^2\cos\alpha + gh) \tag{15}$$

In fact, the value of κ reflects the homogenization of fluid velocity and pressure on the entrance and exit of jet. Where, g is the gravity acceleration force, h is the depth of water.

We can also consider the effect of $\boldsymbol{F}_{\text{interaction}}$ to the water energy by the formula $\frac{\partial E}{\partial t} = \iint_{\Sigma} \boldsymbol{T}_n \cdot \boldsymbol{V} dA$, where E is the total energy of water.

$$\begin{aligned}\frac{\partial E}{\partial t} &= \iint_{\Sigma} \boldsymbol{T}_n \cdot \boldsymbol{V} dA = \iint_{\Sigma} \boldsymbol{F}_{\text{interaction}} \cdot \boldsymbol{V} dA = \iint_{\Sigma} ((-\rho V^2 \kappa l \cos\alpha)\boldsymbol{j} - l\rho g h \cdot \boldsymbol{n}) \cdot \boldsymbol{V} dA \\ &= \iint_{\Sigma} \rho V l (\kappa V^2 \cos^2\alpha + gh\cos\alpha) dA\end{aligned} \tag{16}$$

The above equation is very simple but with an important implication to separate the pattern of energy. We can define Q to illustrate the result as well:

$$Q = c \cdot V^2 / gh \tag{17}$$

Where, c is the ratio of $\kappa \cos^2\alpha$ and $\cos\alpha$ in the equation (16).

It is believed that, once a tsunami is induced by an earthquake, the uplift velocity of seabed is between 0.1-10m/s, and h is between 500-5000m. According to Equation (17), Q would be in the range of 2.04×10^{-7} to 0.0204 if c is about 1. This range of Q value shows that, compared with the potential energy, the kinetic energy of water is very small in the tsunami incitement process. On the other hand, the initial tsunami height is correlated with the energy of the potential; hence, we can conclude that tsunami propagation simulating initial condition is approximately replaced by the seismic static near-field displacement.

To test this statement, we did an Ansys/Ls-Dyna numerical simulation.

Ls-Dyna is mainly an explicit scheme code first developed by Hallquist (1976), and it became a commercial product inbuilt in the Ansys software around 2003. Anghileri et al. (2005) used it to simulate four descriptive patterns of water model. We utilize the Lagrange method to simulate the water. The model parameters are given in table 1.

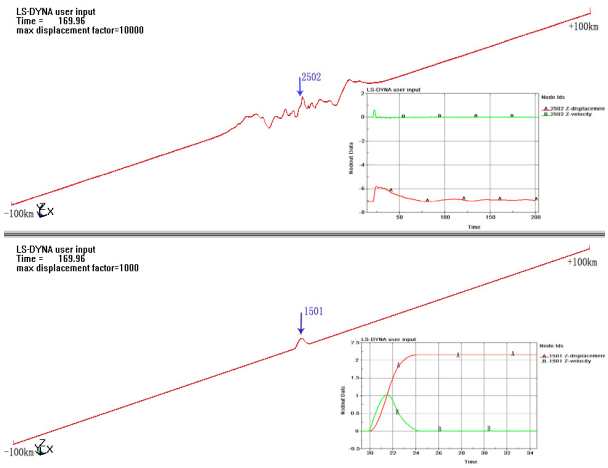

Fig.2 The sea level deformation after about 150s by the incitement and the evolution of velocity and displacement on node 1501(level) and node 2502(seabed)

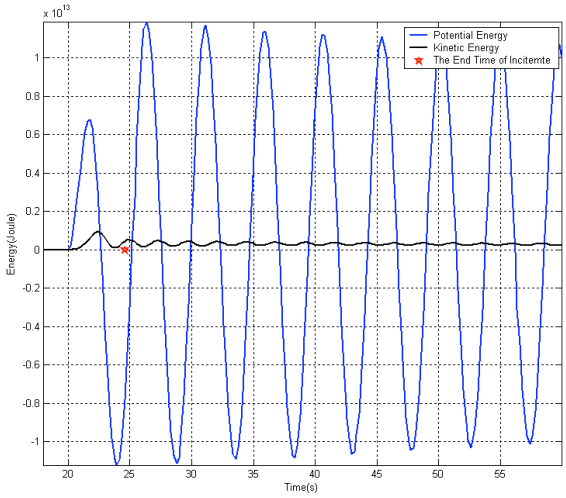

Fig.3 The evolution of potential and kinetic energy in the incitement progress, "★" the end time of incitement

Table 1 the parameters of water model

*MAT_NULL							
1	1000.0	0	0	0	0	0	0
*EOS_GRUNEISEN							
1	1.647E3	1.921	-0.096	0	0.350	0	0
0.0							

In the simulation, the depth of water, which considered to be the compressible GRUNEISEN model (see table 1), is 2000 meters. We establish a three dimensional calculation, but the y-axis is a "unit" length (200 meters, a length of lattice). A 5 km width sea bed with a smooth run-up sites in middle (see fig.2). As the compressibility of water, in the starting 20 seconds, we set the sea bed stationary; and a weight damping algorithm is engaged for creating an initial quasi-static sea environment. The evolution of potential and kinetic energy in the incitement progress is shown in Fig. 3. The difference of amplitude shows that the potential energy plays a dominant role. Fig.2 also shows that the disturbed water spreads with an approximate celerity of gravity water C ($C = \sqrt{gh}$). This result indicates that using the weight-damping algorithm in the calculation is very important; otherwise, like in the work of Ohmachi et al. (2005), the water wave spreads very fast; and we think their velocity is the sound speed in water instead of the tsunami prorogation's. As a result, static displacement is of satisfying approximation to initial tsunami wave, we can utilize the EDGRN/EDCMP program to calculate the effect of the dislocation, fault length, fault width, fault central depth, obliquity, and rake in the seismic near-field static displacement, in order to give the possibility of tsunami from different pattern of seafloor earthquakes (see the appendix).

PART (II) Determining the OPTIMAL ANCHOR-GROUNDED Tsunami OBSERVATIONAL STATION

In this section, we present a method to determine the best location for the anchor-grounded tsunami observation station in the region west of 126E. Three primary factors that control the site-selection include the clustered seismic activity, the population distribution of cities near China coastline and comparative propagation damping coefficient from the Manning formula.

The following factors are also taken into account:

(1) Seismic activity; there are 670 historical earthquake events, which span from 1976 to 2006 and spread across the 115-135 longitude and 20-41 latitude. The cluster method, K-means clustering, compress the 670 events into 40 representations.

(2) Altitude of each observation point; the land points (dry points) are set the weight of 3/8p, and p is an artificial small value for Surfer imaging. The total nodes in the model are 301□316(a node per 2 minute).

(3) National boundaries, namely, simply give a weight of 5/8p to the region east of 126^0 E.

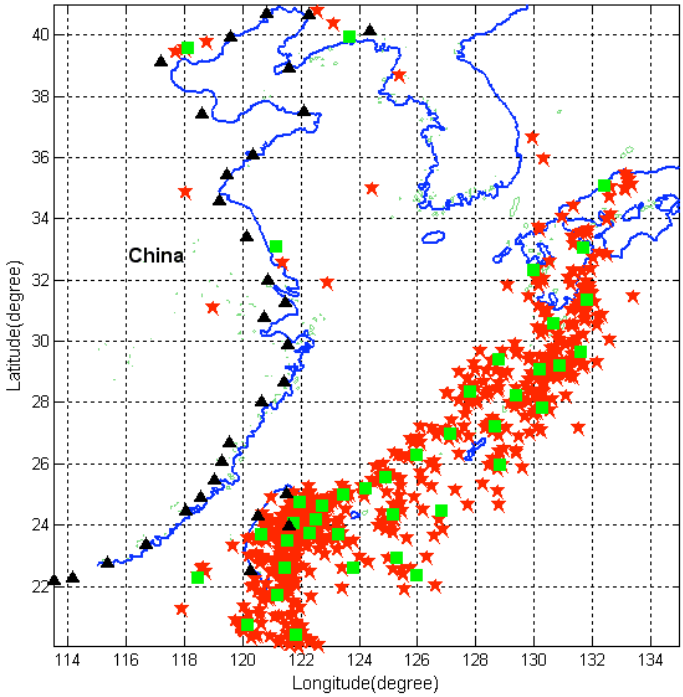

Fig. 4 The distribution of earthquake central (red star) in China eastern sea and neighboring region (1976-2006, Mw>5, data come from http://www.globalcmt.org/CMTsearch.html) and cluster central (green pane).

(4) Distance from the center of the nearest three cities **C**. If it is less than 50km, the weight is as small as p. The article includes 33 coastal cities, for instance, Macao, Hong Kong, Shanghai, Tianjin, Taipei, Taichung, Kaohsiung, Hualien and so on (see Fig. 4 the black triangle symbols).

The above four steps are engaged for reducing the cost of calculation.

(5) Synthesized effect of inshore cities. Here, we consider the systematical interaction among the observational station **R**, the nearest three cities population weighted position **C**, the sum population $Popu_k$ of three cities, and the angle $\boldsymbol{\theta}$ between vector of **SR** and **RC** (see Fig. 6).

(6) Consumed time in the propagation of **SR**. The consumed time $\eta\_t = \dfrac{T\_mean}{T\_mean + T_{RS}}$, where, T_mean is that the span of calculation area divided by the mean of the gravity velocity of the total sea points, is modified by the T_mean in order to avoid the excess exaggeration of length effect of ray.

(7) Damping coefficient. Using the Manning formula $n = \sqrt{\dfrac{fh^{1/3}}{2g}}$, then $f = \dfrac{2n^2 g}{h^{1/3}}$ .And we define the $Q_{rs} = e^{-\varepsilon_1 \times L_{RS} \times \frac{(f_1 + f_2 + \cdots + f_k + \cdots + f_n)}{n}}$ for the whole damping effect for points of each propagation ray **RS**. ε_1 is a modulated factor. And the land points (dry points) are given a specified large friction (see Fig.5).

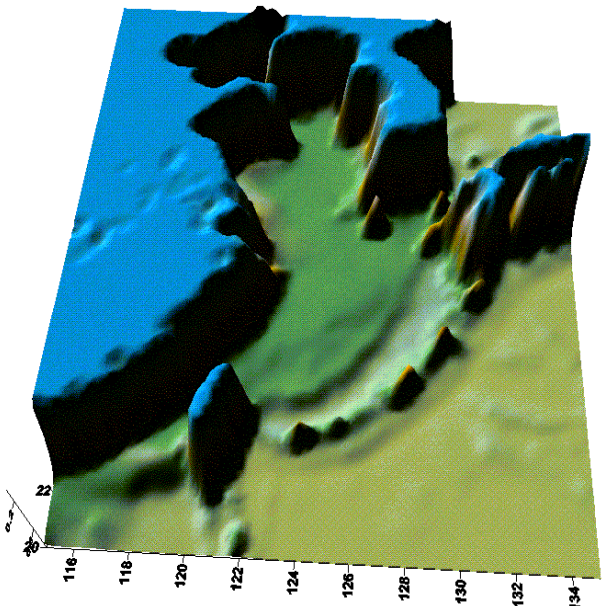

Fig. 5 Distribution of friction in the region

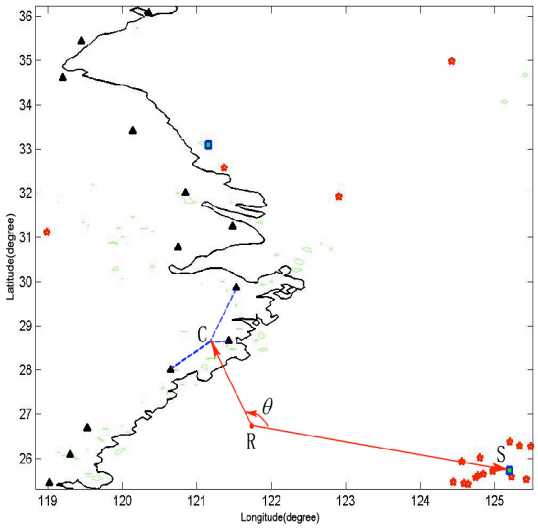

Fig. 6 The cluster central **S**, anchor point **R**, and the weighted central of cities **C**, and the angle $\boldsymbol{\theta}$

(8) Warning time and Cost; making use of $\mu(L) = v_i \times (\frac{1}{2L} + \frac{1}{0.28L + \frac{2000}{L-49}})$, ($L$≥50km) to replace the effect. $\mu(L)$ is approximately like the F-distribution of the Probability in the calculating interval. where, v_i is separated into three classes according to the water depth. In the article, let the ratio are 2:3:5 with respect to the 0-100, 100-600, 600-2000 meters.

(9) The ratio of land points in the ray **RS**; if the ratio is larger than 2/3, the effect of the j^{th} ray is set to be zero. The factor (9) can partly reflect the contributions of obstacle islands or land in collaboration with factor (7).

The mathematical model eventually is established as follow

$$P_i = \sum_k \{\mu(L_{R_i C_k}) \times Popu_k \times [\sum_j (Q_{R_i S_j} \times \eta\_t_{i,j} \times \sin(\frac{1}{2}\theta_{k,i,j})]\} \quad (18)$$

Calculation result is displayed in Fig. 7.

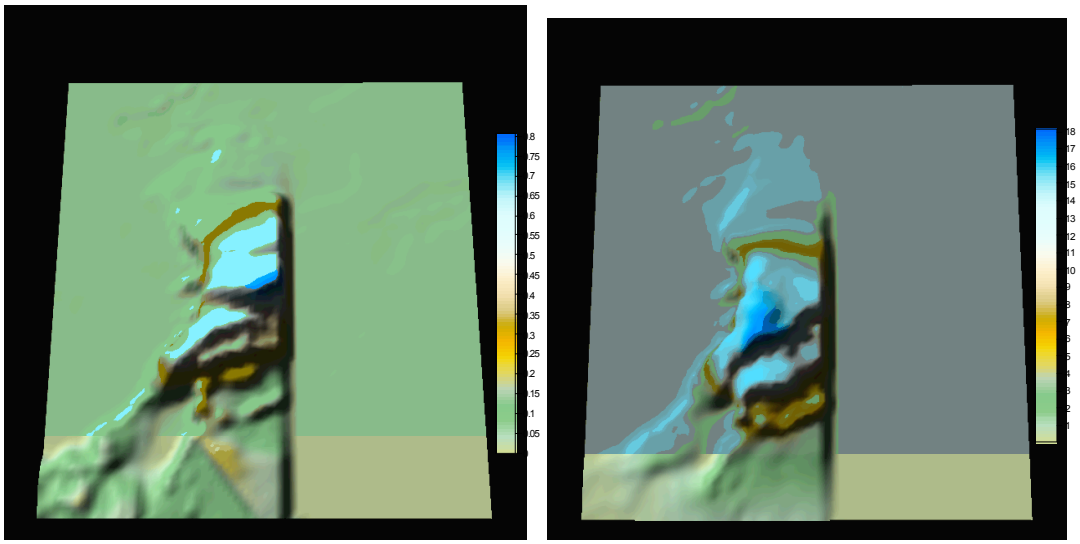

Fig.7 the weight of observational station anchor-grounded in Chinese eastern sea (color value only be compared in each picture respectively)
(a)Consider the 33 cities effect (b) Only concerned with Shanghai

According to the above result, we maybe take some action to decide how to emplace the observation station for tsunami precaution.

CONCLUSION

In this paper, we divide it into two parts. In the first part, we mainly discuss the interaction of fluid-structure in the tsunami incitement process. A valuable result is obtained that the tsunami initial height, which provided for propagation simulating condition, is closely the same as the seismic static near-field displacement. As this result, we can answer the comparative effects between different earthquake parameters by running the EDGRN/EDCMP program.

In the second part, we use the multiplicative principle to organize 9 factors to discuss the problem of observation station anchor-grounded for Chinese eastern sea region. Two cases of our calculations are displayed in Fig.7. They illustrate together an arc area with a high weight to the east of Zhejiang and Fujian provinces. The east-northern edge of Taiwan island get a much higher weight as well, but Bohai sea is a small weight area. It behooves us to make a reference for optimum of tsunami observation.

ACKNOWLEDGEMENTS

In the accomplishment of this paper, we have received the zealous help and support from Professor Steven, N.Ward, Dr. Yinchun Liu at University of Minnesota, USA, Dr. Rongjiang Wang, at Potsdam, Germany, and Dr. Ting Yang at Tongji University, Shanghai. We express our thanks for their generosity. The work is supported by the National Geophysical Observatory at Sheshan (2007FY220100), the Chinese Joint Seismological Science Foundation (106078) and NSFC (40576022).

APPENDIX

(I) *The Effect of Earthquake Parameters*

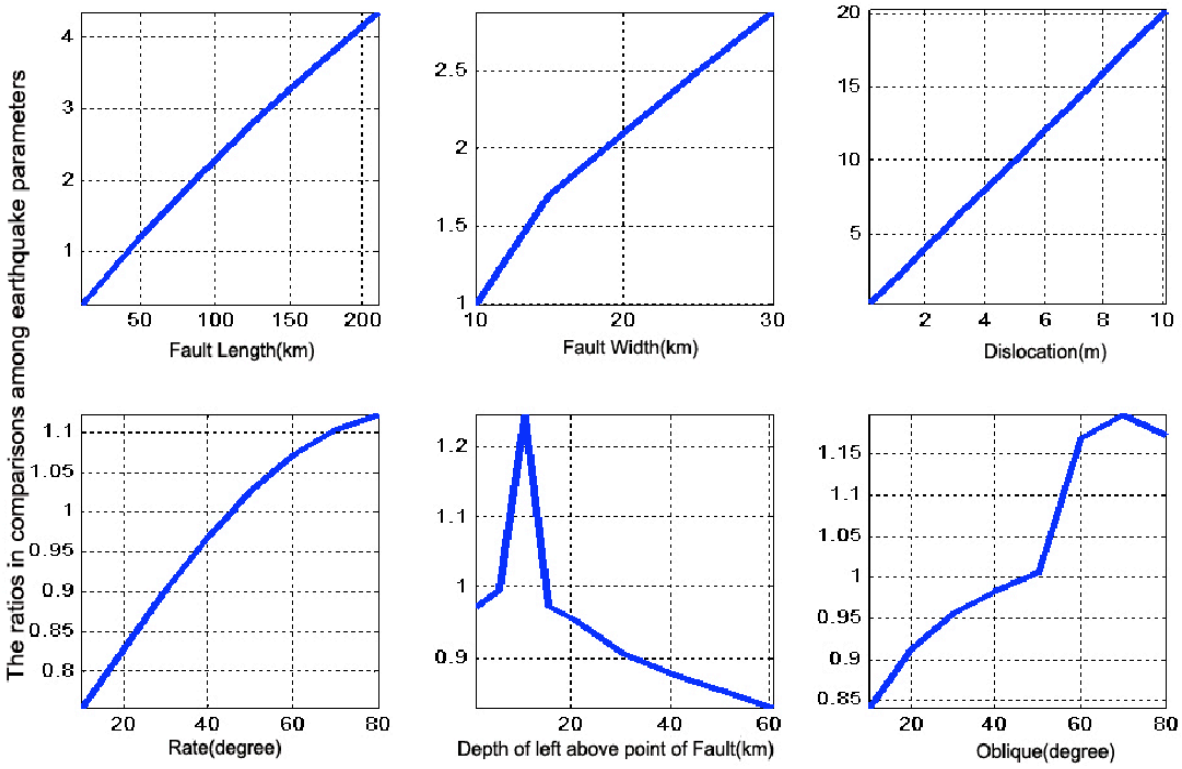

Fig. 8 The effect among different earthquake parameters

Fig.8 is calculated by the EDGRN/EDCMP program (Wang Rongjiang, 2003). As the expatiation in the Part (I), we conclude the tsunami initial propagation condition is closely the same as the seismic static near-field displacement. Usually, the tsunami is mainly disturbed by the vertical component of displacement, thus, we calculate a 400km×400km area deformation by diversified earthquakes, with 201×201nodes，then accumulate the absolute vertical displacement component on every node. Eliminating the disharmony between dimension of the calculating area and true disturbed area by earthquake, for instance, removing the case of the calculating area is less than true disturbed area, we make the each acuminated displacement component to be divided by a "unit" displacement by a referenced earthquake with a 40km fault length, 10km fault width, 5km depth of the left above fault point, 0.5m dislocation, 45^0 rate and 45^0 oblique. It is easy for us to discover that the dislocation plays the most important role in the near-field displacement, and there is an inflexion on the effect as the depth of epicenter becomes deeper gradually because of the effective energy released by earthquake.

(II) ***The Simulation Near the Yaeyama Islands***

Fig. 9 is a hypothetic tsunami nonlinear simulation near the Yaeyama islands, with the Manning constant n=0.012 and the COMCOT program (SCEE, 2006). The topography data of two minutes come from the NGDC. We interpret the data into the one-minute with a third-order B-spline method. The result indicates n=0.012 is credible for the actual calculating. Thus, in the part (II), we also set the n=0.012 for the factor (7).

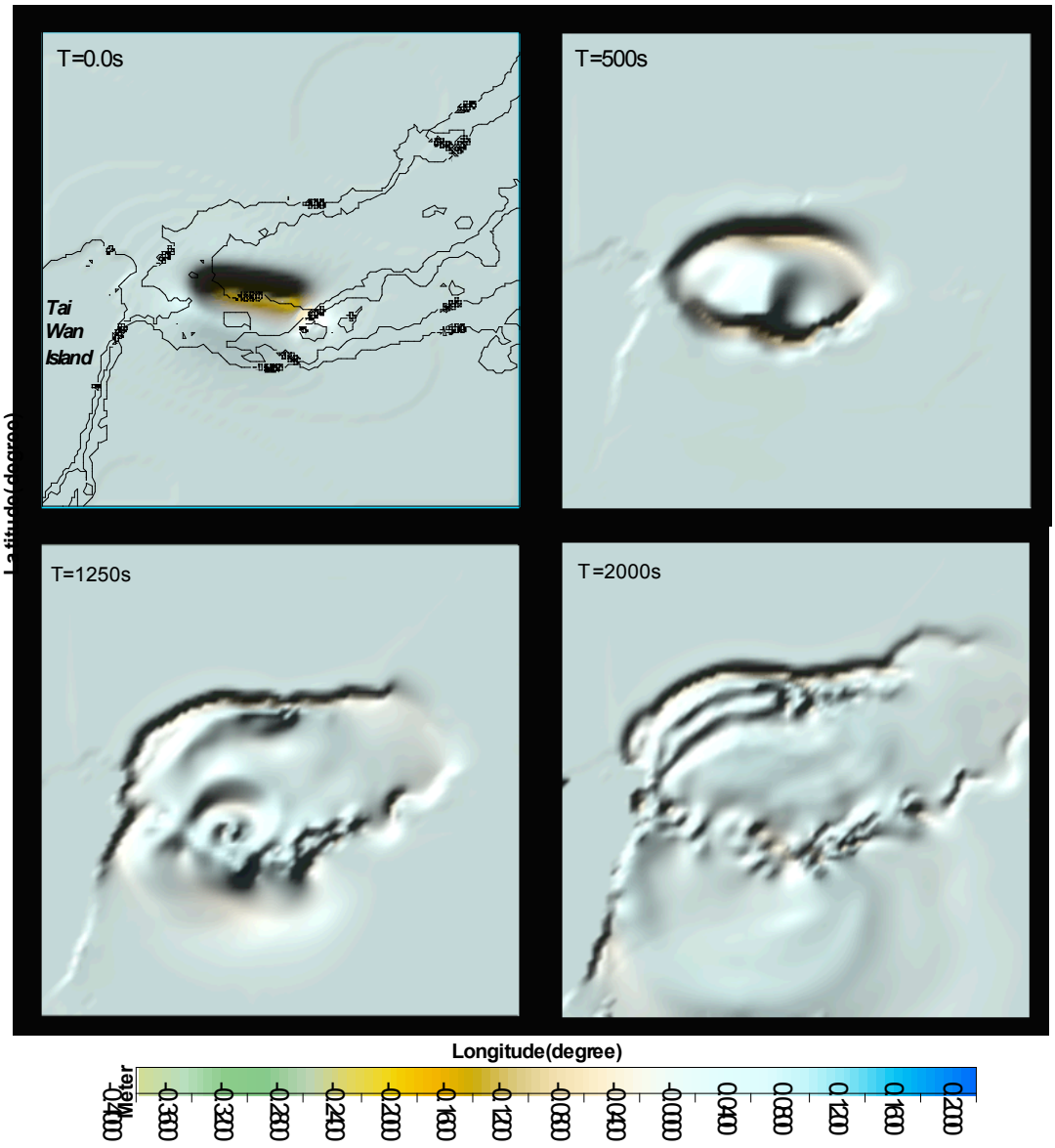

Fig. 9 A hypothesis tsunami simulation near the Yaeyama islands

REFERENCES

[1] Carlo Brandini, Stéphan T. Grilli.(2001). Modeling of freak wave generation in a 3D-NWT, To appear in Proc.ISOPE 2001 Conf. Stavanger, Norway (http://www.oce.uri.edu/~grilli/isope13.pdf)

[2] Gutenberg, B. (1939). Tsunamis and earthquakes, Bull, seism, Soc.America. **29:4**, 517-526

[3] John O.Hallquist (2006). LS-DYN A theory manual

[4] Kajiura, K (1970). Tsunami Source, Energy and the Directivity of Wave Radiation, Bulletin of the Earthquake Research Institute, **Vol.48**, 835-869

[5] M.D. Trifunac, A. Hayir, M.I. Todorovska. (2003). A note on tsunami caused by submarine slides and slumps spreading in one dimension with non-uniform displacement amplitudes, Soil Dynamics and Earthquake Engineering **Vol.23**, 223-234

[6] Maria I. Todorovska, Mihailo D. Trifunac (2001). Generation of tsunamis by a slowly spreading uplift of the sea floor, Soil Dynamics and Earthquake Engineering **Vol.21**, 151-167

[7] M.I.Todorovska, A.Hayir, M.D.Trifunac (2002). A note on tsunami amplitudes above submarine slides and slumps, Soil Dynamics and Earthquake Engineering **Vol.22**, 129-141

[8] Philip Watts, Stephan T. Grilli, M. Asce (2005). David R. Tappin and Gerard J.Fryer, Tsunami Generation by Submarine Mass Failure II: Predictive Equations and Case Studies, Journal of Waterway, Port, Coastal, and Ocean Engineering, **Vol.131, No.6**, November 1

[9] P.L.-F Liu, T. -R. Wu, F. Raichlen et al. (2005). Run-up and rundown generated by three-dimensional sliding masses, J. Fluid. Mech, 107-144

[10] Rongjiang Wang et al. (2003). Computation of deformation induced by earthquakes in a multi-layered elastic crust—FORTRAN programs EDGRN/EDCMP, Computers & Geosciences **Vol.29** (2003), 195-207

[11] SCEE (School of Civil and Environmental Engineering, Cornell University)(2006). COMCOT User Manual, Version 1.6

[12] Stéphan T. Grilli, Richard W. Gilbert (2004). Pierre Lubin et al., Numerical Modeling and Experiments for Solitary Wave Shoaling and Breaking over a Sloping Beach, Proceedings of The Thirteenth (2004) International Offshore and Polar Engineering Conference Toulon, France, May23-28, 2004, 306-312

[13] Steven N. Ward (2003). Classical Tsunami Theory-a la Ward

[14] Steven N.Ward. Tsunamis in The Encyclopedia of Physical Science and Technology, ed. R. A. Meyers, Academic Press, **Vol. 17**, 175-191

[15] Tatsuo Ohmachi et al. (2001). Simulation of Tsunami Induced by Dynamic displacement of Seabed due to Seismic Faulting, Bulletin of Seismological Society of America, **91:6**, 1898-1909

PREDICTION OF TSUNAMI PROPAGATION IN THE PEARL RIVER ESTUARY

Sun J. S.,
Wai, O.W.H.*,
Chau, K.T.
and
Wong, R.H.C.

Department of Civil & Structural Engineering,
The Hong Kong Polytechnic University
Hung Hom, Kowloon,
Hong Kong

**Corresponding author—Tel: (852) 27666025; Fax: (852) 23346389;*
email: ceonyx@polyu.edu.hk

ABSTRACT

Tsunamis entering into shallow water regions may become highly nonlinear and this may be due to the irregularity of sea bottom roughness relative to the water depth and the complex coastline geometry. The elliptic mild-slope equation is commonly used to predict the nonlinear wave propagation in shallow water regions but it requires huge amount of computer resources which may not be practical for tsunami propagation predictions. An efficient finite element approach has been adopted in the present project to resolve the nonlinear problem of wave transformation in near shore zones as well as to better conform the model grids to any complex coastline configurations. The efficient approach is based on the wave action conservation equation that takes into account of wave refraction-diffraction and energy dissipation due to bottom roughness. An operator splitting scheme is employed to solve the wave action conservation equation. Firstly, to increase numerical stability, the Eulerian-Lagrangian method is applied to solve the advection terms in the equation. The horizontal terms are then discretized by an implicit finite element method and, finally, the vertical terms are approximated by an implicit finite difference method. A nominal-time iteration method is used to efficiently solve the non-linear irrotational wave number equation for the wave direction. Over 6000 nine-node elements have been used to mesh the Pearl River estuary region. The boundary conditions are based on the results obtained from a simulation applied for a larger computation domain encompassing the entire South China Sea. The computed result provides a general picture of tsunami propagation in the desired region. Model validation and result verification, however, are necessary for any future prediction exercises.

KEYWORDS: Tsunamis, shallow water regions, finite element approach, operator splitting scheme, PRe

1. INTRODUCTION

Tsunami is a high impact low probability maritime hazard that poses a threat to the coastal communities worldwide. The M9.0 Asia Tsunami took place on Dec. 26, 2004 in the Northern part of Sumatra (Lay et al., 2005), the coast region were hit almost immediately by the largest waves with devastating effects. Most of the damages and death toll was caused by the unexpected attack of the tsunami flood waves.

China has a very long stretch of coastline which is exposed to the open ocean. Tens of millions of citizens reside near the coast. Because of the recent rapid economic growth in China, there is a great momentum to push for the development of coastal areas. The coast of southeastern China may be affected by tsunamis generated by earthquakes in the northern part of the South China Sea and the Taiwan region. The study aims at acquiring a better understanding of any potentially hazard regions that are subject to the threat of tsunamis.

Numerical modeling of tsunami serves a double purpose: it allows us to estimate the effects of events which have yet to happen, and it enables us to evaluate our understanding of past tsunami. There are a number of numerical models that are commonly used to simulate tsunami propagation. These models are MIKE21 model developed by the Danish Hydraulic Institute, the Delft3D model developed by Delft Hydraulics in Netherlands, the MOST (method of splitting tsunami) model developed at the University of Southern California in the United States of America (Titov and Synolakis, 1998); the COMCOT (Cornell multi-grid coupled tsunami model) model developed at Cornell University in the United States of America (Gica et al., 2007); TSUNAMI2 model developed at Tohoku University in Japan (Imamura, 1996) and so forth.

In this study the three-dimensional wave model was introduced to simulate the tsunami propagation and wave run-up in the Pearl River estuary (Chen, 2001), which adopted an efficient finite element approach in the present project to resolve the nonlinear problem of wave transformation in near shore zones as well as to better conform the model grids to any complex coastline configurations.

2. TSUNAMI MODEL

2.1. Governing Equations

The problem of gravity surface wave propagation with wave refraction and diffraction on non-uniform current and bottom friction can be described by the following equations.

Irrotational wave number vector:

$$\frac{\partial(K\cdot\sin\alpha_w)}{\partial x}-\frac{\partial(K\cdot\cos\alpha_w)}{\partial y}=0 \tag{2.1}$$

Where K is the modified wave number; α_w is the wave propagation direction; and x, y are the Cartesian coordinates.

Dispersion relation:

$$[\omega - K\cdot U\cos(\alpha_w-\alpha_c)]^2 = gk\cdot\tanh(k\cdot h)-\frac{1}{4}W^{*2} \tag{2.2}$$

where U is the current velocity; α_c is the current direction; k is the wave number; h is the water depth; ω is the wave angular frequency; g is the acceleration of gravity; and W^* is the bottom friction coefficient, $W^* = \frac{4f_w H}{3\pi g}[\frac{\omega}{\sinh(kh)}]^3$, f_w is the wave friction factor.

For rough turbulent flow, a number of formulas have been proposed for the wave friction factor f_w. Based on 44 measured values of f_w which are taken from seven sources, Soulsby (1997) proposed the following equation for f_w.

$$f_w = 1.39\left(\frac{A^{'}}{z_0}\right)^{-0.52} \tag{2.3}$$

where $A^{'} = U_w T / 2\pi$ is the semi-orbital excursion; the roughness length $z_0 = k_s / 30$, k_s is the Nikurades equivalent sand grain roughness; T is the wave period; and $U_w = \frac{\pi H}{T}\frac{1}{\sinh(kh)}$.

Wave action conservation equation:

$$\frac{\partial A}{\partial t} + \frac{\partial}{\partial x}[A(\overline{u} + \frac{cc_g}{\omega_r} K\cos\alpha_w)] + \frac{\partial}{\partial y}[A(\overline{v} + \frac{cc_g}{\omega_r} K\sin\alpha_w)] = -W^* \cdot A \tag{2.4}$$

where A is the wave action, $A = \frac{\omega R^2}{2}$, $R = \frac{H}{2\omega}$, H is the wave height; $\overline{u}$ and $\overline{v}$ are the depth-averaged current velocity in x and y directions; and t is the time.

Wave eikonal equation:

$$\begin{aligned} K^2 = k^2 - \frac{1}{cc_g R}[\frac{\partial^2 R}{\partial t^2} + \frac{\partial W^* R}{\partial t} + 2\overline{u}\frac{\partial}{\partial t}(\frac{\partial R}{\partial x}) + 2\overline{v}\frac{\partial}{\partial t}(\frac{\partial R}{\partial y}) + \frac{\partial R}{\partial x}\frac{\partial \overline{u}}{\partial t} + \frac{\partial R}{\partial y}\frac{\partial \overline{v}}{\partial t}] \\ + \frac{1}{cc_g R}[\frac{\partial}{\partial x}(cc_g\frac{\partial R}{\partial x}) + \frac{\partial}{\partial y}(cc_g\frac{\partial R}{\partial y})] \\ - \frac{1}{cc_g R}[\frac{\partial}{\partial x}(\overline{u}^2\frac{\partial R}{\partial x} + \overline{uv}\frac{\partial R}{\partial y}) + \frac{\partial}{\partial y}(\overline{uv}\frac{\partial R}{\partial x} + \overline{v}^2\frac{\partial R}{\partial y}) + \frac{W^{*2}}{4}R] \end{aligned} \tag{2.5}$$

in which c is the wave speed; and c_g is the wave group speed.

2.2. Boundary conditions

The conditions at the boundaries enclosing the computational domain must be specified to completely define the problem. Two kinds of boundaries, namely, the incident wave boundaries and absorbing boundaries that absorb all wave energy arriving are considered. Generally, the incident wave boundary is the deepwater wave condition or the measured wave condition at the open boundary and the absorbing boundary is the land boundary.

The wave energy arriving at absorbing boundaries from the fluid domain must be absorbed perfectly. The treatment of this kind of boundary is difficult in numerical modeling. The most commonly used method is the Sommerfeld radiation condition which can be written as:

$$\begin{aligned} H_t + C_x H_x = 0 \\ H_t + C_y H_y = 0 \end{aligned} \tag{2.6}$$

where C_x and C_y are the phase speeds along the x and y directions, respectively. In the actual computation, it is difficult to obtain the exact phase speeds and hence, the boundary can still reflect some wave energy.

To eliminate the boundary reflections, a 'sponge' layer proposed by Larsen and Dancy (1983) is placed in front of an absorbing boundary to absorb the incoming wave energy. On the sponge layer, the wave height is divided by a factor, $\mu(x,y)$, after each step. The factor $\mu(x,y)$ takes the following form after extending the one-dimensional form given by Larsen and Dancy (1983) to two dimensions (Li *et al.*, 1999).

$$\mu(x,y)=\begin{cases}\exp\left[\left(2^{-d/\Delta d}-2^{-d_s/\Delta d}\right)\ln\alpha\right] & 0\le d\le d_s\\ 1 & d_s<d\end{cases} \tag{2.7}$$

in which d is the distance between the 'sponge' layer and the boundary; Δd is the typical dimension of the elements; d_s is the sponge layer thickness, usually equal to one to two wave lengths and α is a constant to be specified.

2.3. Numerical Schemes

The computation procedure starts from the seaward boundaries in which Eq. (2.1) is first solved for α_w by assuming an initial value of the modified wave number, e.g. $K=k$. Using the values of α_w and K, Eq. (2.4) is then solved for the wave height. With the known values of the wave direction and wave height, the values K are updated using Eq. (2.5). The procedure is repeated until convergence is achieved.

2.3.1 Splitting of wave action equation

To increase the numerical stability, an operator splitting method is applied to the wave action equation. The time integration of the wave action equation is performed in two sequential stages. That is, a time step is divided into two sub-steps in which the first step is for the advective terms and the second step is for the other terms.

In the first sub-step, the advective term is solved for wave action. In general, numerical instability in wave propagation computations is mainly caused by the incorrect approximation of the advective term. To increase the numerical stability, an Eulerian-Lagrangian method is applied to discretize the advective term. The equation in this sub-step is given as:

$$\frac{A^{n+\frac{1}{2}}-A^n}{\Delta t}+\left[\left(\bar{u}+\frac{cc_g}{\omega}\cdot K\cdot\cos\alpha_w\right)\frac{\partial A}{\partial x}\right]^n+\left[\left(\bar{v}+\frac{cc_g}{\omega}\cdot K\cdot\sin\alpha_w\right)\frac{\partial A}{\partial y}\right]^n=0 \tag{2.8}$$

in which Δt is time step.

In the second sub-step, the other terms in the wave action equation are calculated using the implicit finite element method. The equation to be solved in this sub-step is:

$$\frac{A^{n+1}-A^{n+\frac{1}{2}}}{\Delta t}+A^{n+1}\cdot\frac{\partial}{\partial x}\left(\bar{u}+\frac{cc_g}{\omega}\cdot K\cdot\cos\alpha_w\right)^{n+\frac{1}{2}}+A^{n+1}\cdot\frac{\partial}{\partial y}\left(\bar{v}+\frac{cc_g}{\omega}\cdot K\cdot\sin\alpha_w\right)^{n+\frac{1}{2}}=\left(-W^*\cdot A\right)^{n+1} \tag{2.9}$$

2.3.2 Spatial discretizations

In the first sub-step, Eq. (2.8) is approximated by an explicit Eulerian-Lagrangian Method (ELM). The Eulerian-Lagrangian method has advantages over other commonly used numerical methods, such as the upwind method and the ADI method. The scheme was subsequently extended to three dimensions by Casulli and Cheng (1992). In the method, a fluid particle is assumed to arrive at a mesh node at the end of a time step, and the known value of a certain variable at the beginning of the time step is assumed to be constant over the time step. The position of the particle at the beginning of the time step may be obtained by backtracking and its value can be obtained through interpolation from the values at the surrounding mesh points. In this study, the Eulerian-Lagrangian method is employed to handle the advective term in the wave action equation.
To obtain an Eulerian-Lagrangian approximation, a wave ray or the transport of the wave action from a point x_i over time is defined as follows.

$$\frac{dx}{dt} = \overline{u} + \frac{cc_g}{\omega} \cdot K \cdot \cos\alpha_w \quad , \qquad \frac{dy}{dt} = \overline{v} + \frac{cc_g}{\omega} \cdot K \cdot \sin\alpha_w \tag{2.10}$$

A particle that ends at a mesh node has a position at the beginning of the time step that can be obtained by assuming a constant wave velocity over the time step. This can be written as:

$$x_p = x_i - \Delta t \cdot (\overline{u} + \frac{cc_g}{\omega} \cdot K \cdot \cos\alpha_w) \, , \qquad y_p = y_i - \Delta t \cdot (\overline{v} + \frac{cc_g}{\omega} \cdot K \cdot \sin\alpha_w) \tag{2.11}$$

in which x_p, y_p are the coordinates of a particle at a beginning position p; x_i, y_i are the coordinates of a particle at node i.

2.3.3 Approximation of the other terms of the wave action equation by an implicit finite element method

In the second step, the other terms in the wave action equation were calculated using the implicit finite element method (FEM).
For accurate computations, the nine-node isoparameteric quadrilateral finite elements are employed in this model. The 2nd-order nine-node isoparametric shape functions are expressed as follows:

$$\phi_j = \begin{cases} \frac{1}{4}(\xi_j\xi)(\eta_j\eta)(1+\xi_j\xi)(1+\eta_j\eta) & for\ j = 1,...,4 \\ \frac{1}{2}(\xi_j\xi + \eta_j\eta)(1+\xi_j\xi+\eta_j\eta)(1-\xi_j^2\eta^2-\eta_j^2\xi^2) & for\ j = 5,...,8 \\ (1-\xi^2)(1-\eta^2) & for\ j = 9 \end{cases} \tag{2.12}$$

in which ϕ is the interpolation function; ξ and η are the local coordinates.
Subdividing the domain of interest Ω into finite elements and denoting a generic element by Ω^e, the dependent variables in wave action conservation equations are approximated within the elements as follows

$$f \approx \sum_{i=1}^{nd} \phi_i f_i \tag{2.13}$$

where f_i is the values of any independent variable at the nodal points, nd is the number of nodes.

The Galerkin's method with the use of integration by parts and Green's theorem are applied to Eq. (3.10). The following element matrix equations can be obtained.

$$[D]\{A_i^{n+1}\} = [M]\left\{A_i^{n+\frac{1}{2}}\right\} \tag{2.14}$$

where $A_i = [A_1, A_2, \ldots A_N]^T$, N is the number of nodes,

$$[D] = \sum_{e=1}^{M}\{\frac{1}{\Delta t}\cdot S1_{jk}^{(e)} + S2_{jkl}^{(e)}\cdot(\bar{u} + \frac{cc_g}{\omega}\cdot K\cdot\cos\alpha_w)_l^{(e)} + S3_{jkl}^{(e)}\cdot(\bar{v} + \frac{cc_g}{\omega}\cdot K\cdot\sin\alpha_w)_l^{(e)} + S4_{jkl}^{(e)}\cdot W_l^{*(e)}\} \tag{2.15}$$

$$[M] = \sum_{e=1}^{M}(\frac{1}{\Delta t}\cdot S1_{jk}^{(e)}) \tag{2.16}$$

$$S1_{jk}^{(e)} = \iint_{\Omega^e}\phi_j\cdot\phi_k\cdot|J|d\xi d\eta \tag{2.17}$$

$$S2_{jkl}^{(e)} = \iint_{\Omega^e}\phi_j\cdot\phi_k\cdot P_l d\xi d\eta \tag{2.18}$$

$$S3_{jkl}^{(e)} = \iint_{\Omega^e}\phi_j\cdot\phi_k\cdot Q_l d\xi d\eta \tag{2.19}$$

$$S4_{jkl}^{(e)} = \iint_{\Omega^e}\phi_j\cdot\phi_k\cdot\phi_l\cdot|J|d\xi d\eta \tag{2.20}$$

$$P_j = \frac{\partial y}{\partial\eta}\frac{\partial\phi_j}{\partial\xi} - \frac{\partial y}{\partial\xi}\frac{\partial\phi_j}{\partial\eta} \tag{2.21}$$

$$Q_j = -\frac{\partial x}{\partial\eta}\frac{\partial\phi_j}{\partial\xi} + \frac{\partial x}{\partial\xi}\frac{\partial\phi_j}{\partial\eta}. \tag{2.22}$$

Here, M is the total number of elements; and $|J|$ is Jacobi matrix as given below

$$|J| = \begin{vmatrix}\frac{\partial x}{\partial\xi} & \frac{\partial y}{\partial\xi}\\ \frac{\partial x}{\partial\eta} & \frac{\partial y}{\partial\eta}\end{vmatrix} \tag{2.23}$$

2.3.4 Approximation of the wave number equation by an iteration method

To solve the wave number equation (Eq. 2.1) for the wave direction, a direct discetization of this equation by either the finite element method or a finite difference method may end up with numerical instability in complex geometrical boundary situations. This problem is mainly due to the solution of a highly non-linear equation for

the entire computational domain in every time step. To increase stability, an iteration method is presented. A nominal (or fictitious) temporal derivative term is added to Eq. (2.1) and the spatial derivatives of the wave number are discretized by a finite node method (FNM) at each node. FNM is a mixture of the finite element method (FEM) and the finite difference method (FDM). The form of expression of the FNM is similar to that of the FEM and the basic solution process is the same as in FDM. Eq. (2.1) with the nominal temporal term is written as:

$$\frac{\partial \alpha_w}{\partial t'} + \frac{\partial (K \cdot \sin \alpha_w)}{\partial x} - \frac{\partial (K \cdot \cos \alpha_w)}{\partial y} = 0 \tag{2.24}$$

where t' is the nominal time.

Using a finite node method, Equation (2.24) becomes:

$$\alpha_{w,i}^{n+1} = \alpha_{w,i}^{n} + f(K_0) \cdot \{ \frac{\Delta t'}{M_i} \sum_{e=1}^{M_i} [\frac{\partial \varphi_j^{(e)}}{\partial y} (K \cos \alpha_w)_j^{(e)}]_i^n - \frac{\Delta t'}{M_i} \sum_{e=1}^{M_i} [\frac{\partial \varphi_j^{(e)}}{\partial x} (K \sin \alpha_w)_j^{(e)}]_i^n \} \tag{2.25}$$

in which M_i is the number of elements around the i-th node; φ_j is the four-node isoparametric shape function; $f(K_0)$ is a coefficient for improving numerical stability and speeding up convergence where $f(K_0) = \frac{0.99^n}{K_0}$; K_0 is the deep water wave number. Note that the grid layouts for wave direction calculation and the wave height calculation are the same.

2.4 Tsunami Simulations

The main goal of the present project is to estimate tsunami propagation and wave run-up numerically in the Pearl River estuary (PRe) to gain better understanding of the tsunami risk in this region. The coast of southeastern China may be affected by tsunamis generated by earthquakes in the northern part of the South China Sea, therefore in this study; we used two bathymetry layouts to carry out more realistic simulations of the tsunami propagation. One layout covers the entire South China Sea (SCS) region obtained from the National Geophysical Data Centre ETOPO2 which consists of digital averaged land and sea floor elevations assembled from several uniformly gridded data bases with a grid spacing of 2 minutes of latitude by 2 minutes of longitude (about 3.6 km by 3.6 km in size). The PRe layout is obtained by combining the coastline data and non-uniform bathymetry grid data using software Surfer and ArcGIS. Figures 1 and 2 show the two-bathymetry layouts.

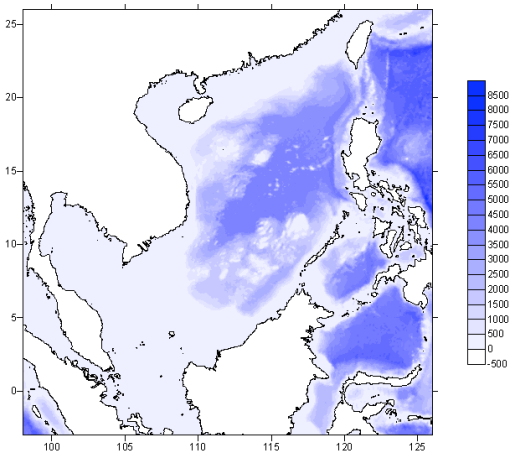

Figure 1 Bathymetry of SCS

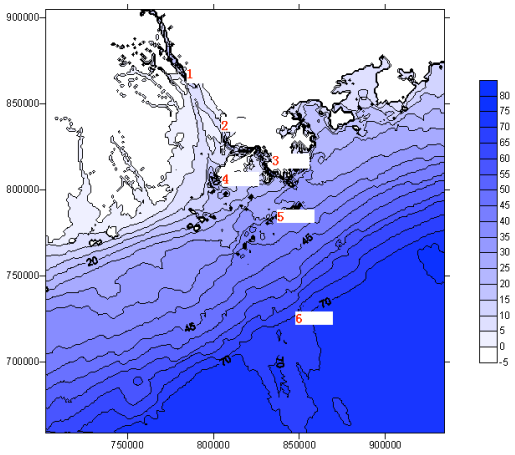

Figure 2 Bathymetry of PRe

The maximum number of grids used in the SCS region is 6385 and the maximum number of grids used in the PRe region is 6036. Figures 3 and 4 show the two grid layouts.

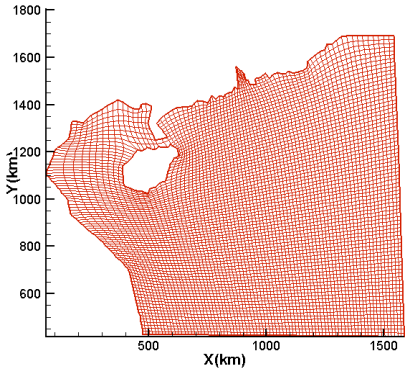

Fig 3 Grids of the SCS

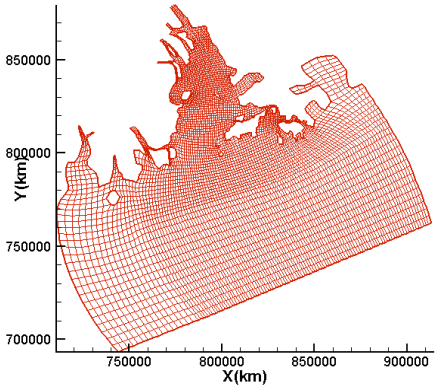

Fig 4 Grids of the PRe

Simulations of tsunami propagation were firstly carried out for the SCS region. The water elevation result of the SCS simulation was then used as the initial and boundary conditions for the PRe region simulations. Simulations of different scenarios have been conducted to test the model stability, capability and reliability. In this paper, we mainly focus on the PRe region results.

3. RESULTS AND DISCUSSION

The tsunami propagation and run-up patterns in the PRe region are simulated using 3D wave model with boundary conditions based on the SCS simulation results. To demonstrate the stability of the wave model and to estimate the approximate computer time required to simulate wave propagation from the boundary in the open sea, a pure wave propagating in quiescent water was modeled.

Fig 5 and Fig show the wave heights and directions in the Hong Kong Waters and the Pearl River Estuary, respectively, at the equilibrium state. In these figures, the contours represent the wave heights and arrows indicate both the wave heights and wave directions. It can be seen from the figures that the wave height in the open sea is relatively uniform. Due to the existence of numerous islands and complex coastlines, refraction and diffractions occur when waves impinge on the obstacles or the irregular land boundaries. The sheltering effects from the two larger islands, Hong Kong Island and Lantau Island, are significant. The wave heights behind them are reduced markedly. The wave heights in the Victoria Harbour are very small, about 0.2 m. This indicates that it is difficult for waves from the open sea to propagate into Victoria Harbour, where waves will be predominantly local wind-induced. The wave heights behind Lantau Island are about 0.2 to 0.4 m because of sheltering. When waves propagate into the Pearl River Estuary, the shoaling and sheltering effects of islands dissipate the wave energy gradually. Consequently, the wave height diminishes gradually from around 1.4 m near the Waglan Island to about 0.1 m at Humen.

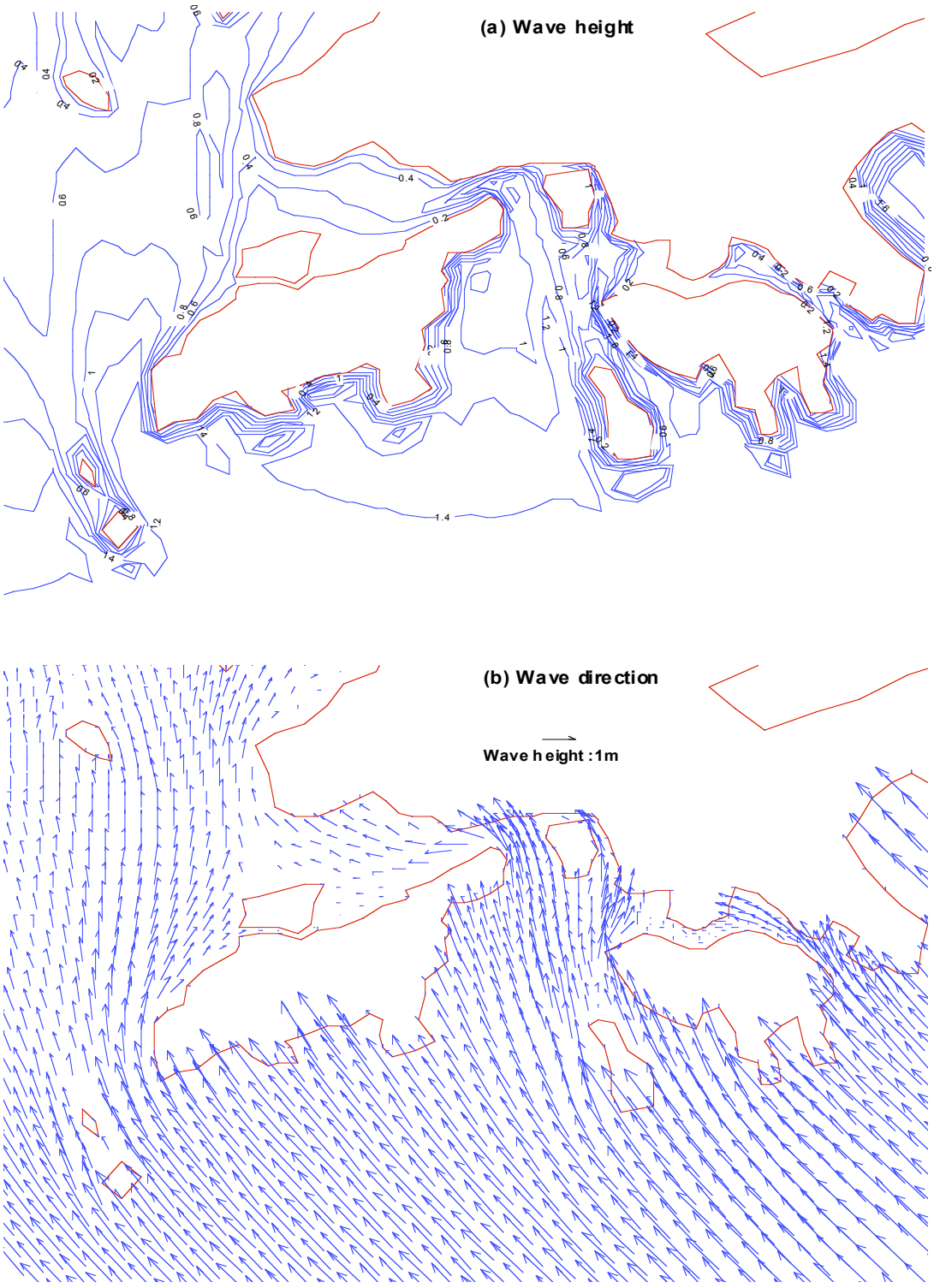

Fig 5 Simulated wave heights and directions in quiescent water in Hong Kong waters

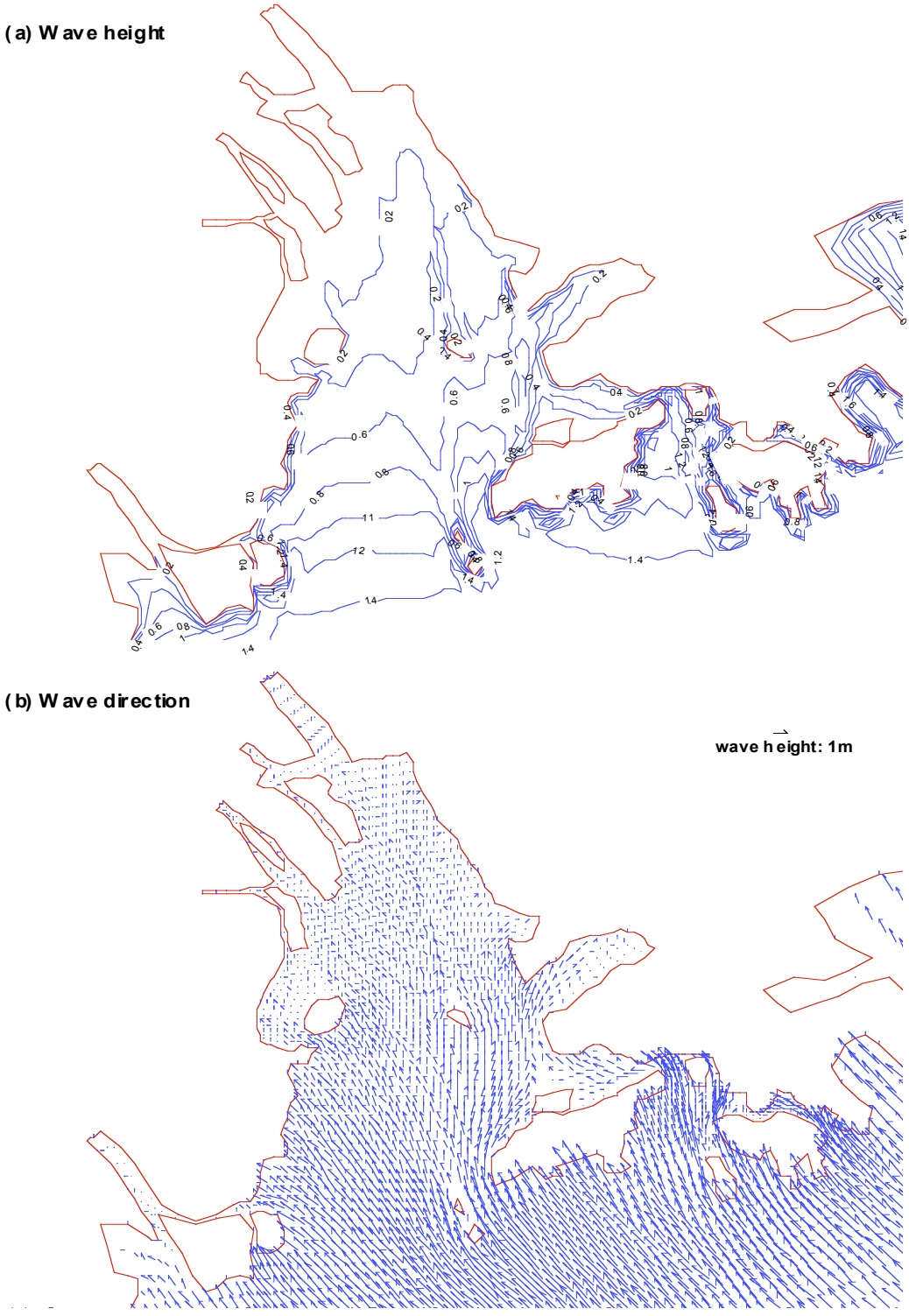

Fig 6 Simulated wave heights and directions in quiescent water in Pre

Simulations with different computation time steps had been conducted. Figs. 7 and 8 show the simulated results with time steps of 1 sec and 60 sec, respectively. The model tends to generate more accurate results when the time step is smaller than 30 sec. From the computed wave distributions shown in Fig 7, it can be seen the wave heights at the up-estuary and the west side of PRE are smaller than those in the east side of the PRe and this may be due to bottom friction and shoaling effects.

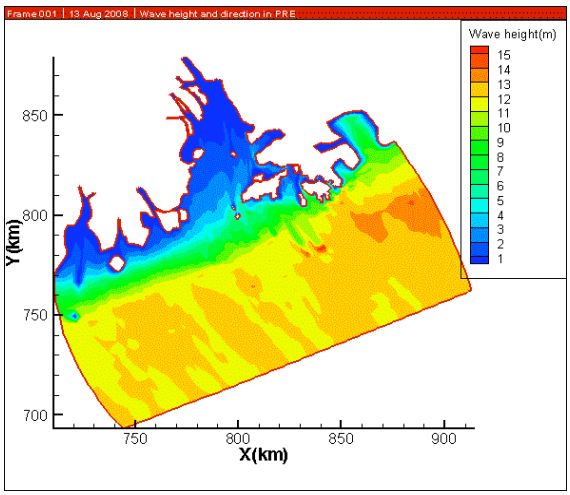

Fig 7 Wave height distribution
(time step = 1 sec)

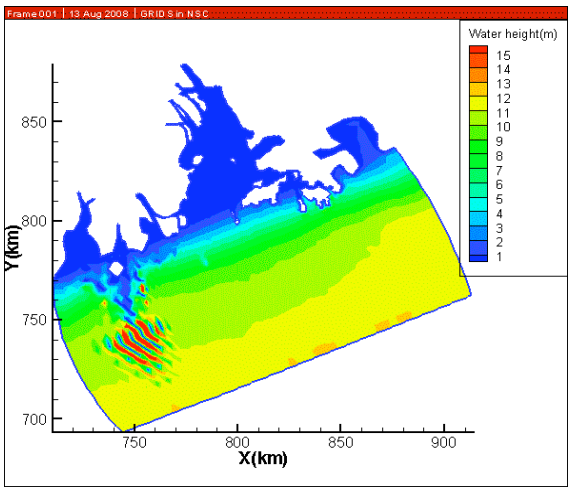

Fig 8 Wave height distribution
(time step = 60 sec)

With a Pentium-4 3.0G CPU personal computer, 1.5 hours of actual clock time are needed to establish the equilibrium wave field for the entire model domain of PRe regions for waves propagating from the open sea boundary (the southern boundary) to the up-estuary river boundary at Hu Men. This demonstrates that the present model can overcome the demanding requirement of computer resource.

4. CONCLUSION

This preliminary numerical study provides a rough estimation of the tsunami propagation in the Pearl River estuary, where the coastline geometry is complex. The model makes use of an operator splitting method in which the Eulerian-Lagrangian method is applied to resolve the advective terms, and the other terms are discretized by the implicit finite-element method in the wave action equation. A nominal time iteration method using a finite-node scheme is applied to solve the nonlinear wave-number equation for the wave directions. This method overcomes the numerical instability caused by other discretization methods used for the solution of the nonlinear wave-number equation. The major improvements of the model include eliminating the convergence and instability problems; increasing computation efficiency; and better representing actual coastline geometries. The model results reveal that, due to the bottom friction and shoaling effects, the wave heights at the up-estuary and the west side of the PRE are smaller than those in the east side of the PRE. Simulations with different computation time steps show that the present model tends to generate more accurate results when the time step is smaller than 30 sec.

It is concluded that the overall performance of the present model is highly satisfactory in gentle bathymetric gradient situations. It is also noticed that the model seems to inherit the smoothing nature of Ebersole's approach. Finer grids should be used in regions where bottom spatial variability is high. Fortunately, finer grids

can be easily established at any desired regions in the model domain with the unstructural finite-element scheme equipped in the model. Model validation and result verification, however, are necessary for any future prediction exercises.

ACKNOWLEDGEMENT

This research was supported separately by two Central Research Grants of The Hong Kong Polytechnic University (Account Nos.: 87K1 and G-U198.)

REFERENCES

Casulli, V. and Cheng, R.T. (1992). SEMIIMPLICIT FINITE-DIFFERENCE METHODS FOR 3-DIMENSIONAL SHALLOW-WATER FLOW. International Journal for Numerical Methods in Fluids 15, 629-648.

Chen, Y. (2001). Sediment transport by waves and currents in the Pearl River Estuary. Ph.D. thesis, Department of Civil and Structural Engineering, The Hong Kong Polytechnic University, Hong Kong.

Gica, E., Teng, M.H., Liu, P.L.F., Titov, V. and Zhou, H.Q. (2007). Sensitivity analysis of source parameters for earthquake-generated distant tsunamis. Journal of Waterway Port Coastal and Ocean Engineering-ASCE **133**, 429-441.

Larsen, J. and Dancy, H. (1983). Open Boundary in short wave simulation – a new approach. *Coastal Eng***7: 3,** 285-297

Lay, T. et al., (2005). The great Sumatra-Andaman earthquake of 26 December 2004. Science **308**, 1127-1133.
Imamura, F. (1996). Review of tsunami simulation with a finite difference method. *Long Wave Runup Models*. World Scientific Publishing

Li, B.G., Xie, Q.C. and Xia, X.M. (1999). Particle size distribution in the turbidity maximum and its responding to the tidal flow in Jiao Jiang Estuary. *Journal of Sediment Research* **1**, 18-26.

Soulsby, R.L. (1997). Dynamics of Marine Sands. *A Manual for Practical Applications*.

Titov, V.V. and Synolakis, C.E. (1998). Numerical modeling of tidal wave run-up. Journal of Waterway Port Coastal and Ocean Engineering-ASCE **124**, 157-171.

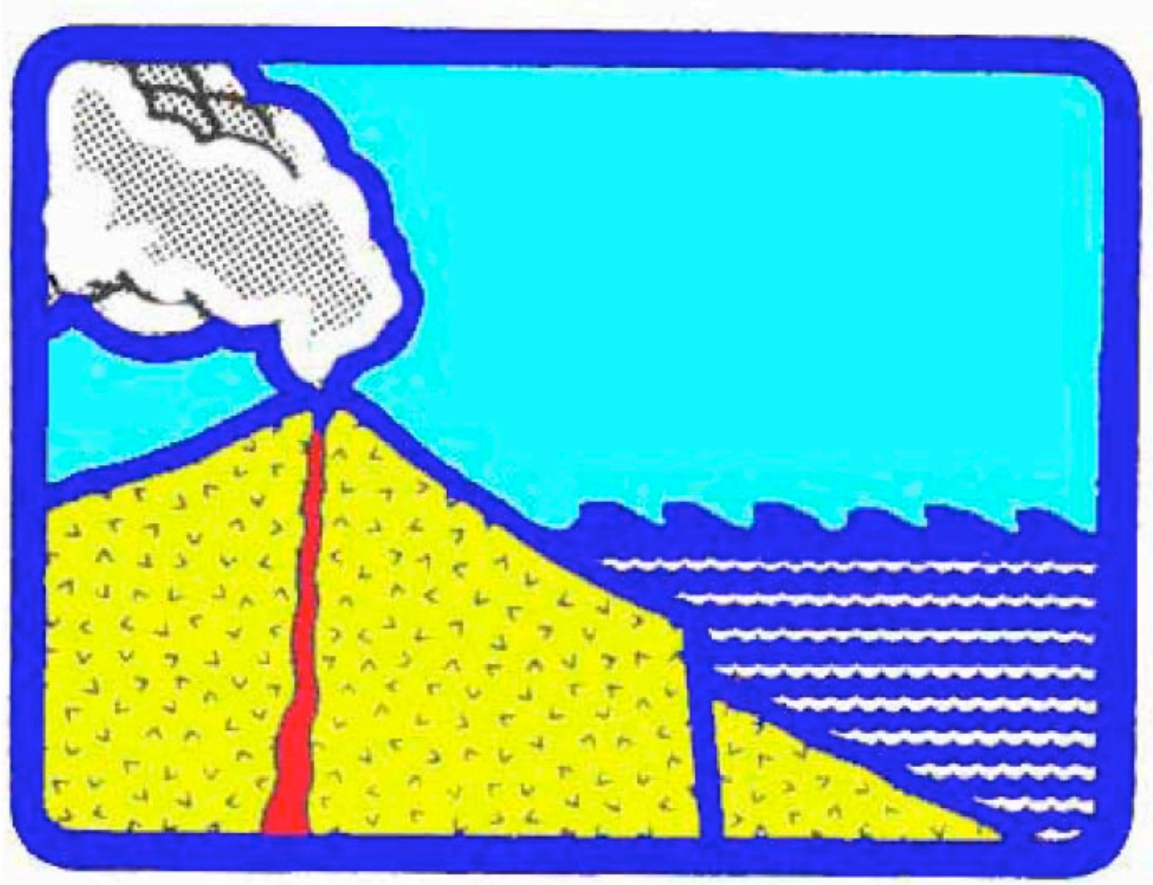

Tsunami Society
1741 Ala Moana Blvd. #70
Honolulu, HI 96815, USA

WWW.TSUNAMISOCIETY.ORG